Биомедицинска техника

Biomedical Engineering

A Rule-Based Control System for Assisting the Gait by Multichannel Functional Electrical Stimulation: Design and Proof of Concept

Eleonora Vendrame, Dejan B. Popović, Emilia Ambrosini, Lana Popović-Maneski

***Abstract*—A rule-based controller to assist stroke survivors' gait through multichannel functional electrical stimulation was developed. The controller was designed for the system comprising a wearable four-channel stimulator and insoles instrumented with pressure sensors and inertial measurement units. The gait segmentation algorithm processes Real-time signals from the sensorized insoles. The heuristically established rules split each gait cycle into five phases. These *If-Then* rules trigger stimulation channels to activate paralyzed thigh and shank muscles in an order that leads to the natural like stance and swing. The stimulator sends electrical pulses via surface electrodes positioned on a hemiplegic patient's paretic leg to activate the quadriceps, the hamstrings, the anterior tibialis, and the gastrocnemius muscles. A graphic user interface was developed to set the stimulation parameters and calibrate the system. The segmentation algorithm was validated on the recordings of 10 stroke patients, and the assistive gait training system was tested on one older adult to prove the concept.**

***Index Terms*—Rule-Based Control; Multichannel Functional Electrical Stimulation; Post-Stroke Gait Restoration.**

I. Introduction

80 percent of stroke survivors develop motor disability and experience problems to walk. Restoring functions after stroke is a complex process mediated by neuroplasticity induced by spontaneous recovery and therapeutic interventions [1]. Early motor training seems essential for successful recovery: motor learning mechanisms may be operative during spontaneous stroke recovery, and by interacting with a rehabilitative exercise, they can be reinforced [2]. Functional Electrical Stimulation (FES) has been used in the rehabilitation of chronic hemiplegia since the 1960s when the first applications for drop-foot correction were patented [3]. During the following years, many improvements were suggested in terms of synchronizing the stimulation with the gait events and the number of stimulated muscles. The first clinically applied FES systems for restoration of locomotion used an open-loop control method, in which stored sequences of muscle activation were associated with the phases of a normal gait cycle [4]. The main drawback of this control was the lack of adaptation of the stimulation to the inevitable walking pattern fluctuations. The microcontroller technology and the enhancement of the gait events detection sensors led to the development of more effective control strategies. The rule-based control (RBC) aims to replace the manual FES-switching function through the automatic detection of the gait phases [5]. This control method is based on *If-Then* expressions: *If* part of the rule corresponds to the real-time recognition of a coded sensor pattern and represents the system*'s state, then* part of the rule triggers the functional movement correspondent to the state identified. The real-time recognition of the gait events is usually performed by Gait Phase Detection (GPD) systems that rely on the signals from artificial sensors. Nowadays, wearable sensors can effectively be used for gait segmentation. Foot pressure insoles or footswitches represent the gold standard in gait segmentation since each gait phase can be associated with a specific sensor output [6]. Alternatively, inertial measurement units (IMU) that comprise accelerometers, gyroscopes, and magnetometers are widely used to feed gait phase discrimination algorithms. The signals from footswitches and pressure/force sensors allow identification of the gait events accurately (e.g., heel contact, push-off). Still, they cannot discriminate against the swing phase's sub-phases. This limitation can be eliminated by adding inertial sensors to provide information about the kinematics of the movement [7]. Kojović et al. [8] presented an automatic control for an FES system based on *If-Then* rules designed by mapping sensors, and muscle activated patterns. The sensor system included accelerometers and force-sensing resistors.

We present here a new rule-based controller for a multichannel electronic stimulator to assist gait in stroke survivors.

II. Materials and Methods

The experimental setup includes the multichannel MOTIMOVE modular functional electrical stimulation system which allows distributed and asynchronous stimulation (compensated biphasic pulses, 1-100 pulses, 50-1000 μs, up to 170 mA) [9], a set of surface electrodes for four muscle groups and the Gait Teacher, a sensorized insole for the acquisition of ground reaction forces and foot kinematics [10] (Fig. 1). The MOTIMOVE controls current pulses on four stimulation channels and receives six analog inputs from the Gait Teacher (sampling rate 100 Hz). Four input signals come from the insole worn on the paretic side: three ground reaction forces estimated from five pressure

Eleonora Vendrame is with the Department of Electronics, Information and Bioengineering, Politecnico di Milano, Piazza Leonardo da Vinci, 32, 20133 Milano MI, Italy (e-mail: eleonora.vendrame@mail.polimi.it).

Emilia Ambrosini is with the NearLab, Department of Electronics, Information and Bioengineering, Politecnico di Milano, Piazza Leonardo da Vinci, 32, 20133 Milano MI, Italy (e-mail: emilia.ambrosini@polimi.it).

Dejan B. Popović is with SASA, Knez Mihailova 35, 11000 Belgrade, Serbia (e-mail: dbp@etf.rs).

Lana Popović-Maneski is with the Institute of Technical Sciences of SASA, Knez Mihailova 35/IV, 11000 Belgrade, Serbia (e-mail: lana.popovic.maneski@itn.sanu.ac.rs).

sensors and the foot's angular rate in the sagittal plane (from the gyroscope) (Fig. 2). Two input signals come from the non-paretic side and are used for the assessment of the gait pattern.

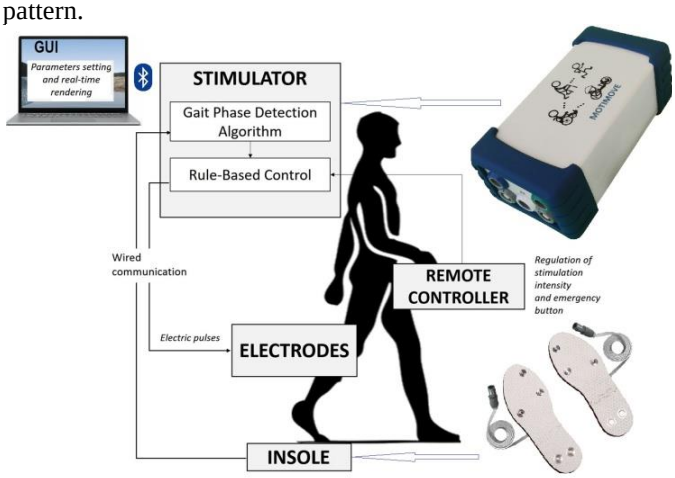

Fig. 1. Setup used for the design and proof of concept of the rule-based controller for FES assisted gait. MOTIMOVE is an up to eight-channel smart electronic stimulator. The Gait Teacher is a set of two instrumented insoles with pressure transducers and inertial measurement units for reproducible, real-time, no hysteresis acquisition of ground force reaction and foot kinematics. The system uses surface electrodes.

A. *Gait Phase Detection Algorithm*

Starting from the signals coming from the Gait Teacher, we implemented a Gait Phase Detection (GPD) algorithm for the real-time detection of gait sub-phases during walking. This algorithm detects five transition events (T1, T2, T3, T4, T5), which define five gait sub-phases corresponding closely to Terminal Swing (TS), Heel Contact (HC), Mid Stance (MS), Push-Off (PO) and Initial Swing (IS), respectively (Fig. 2).

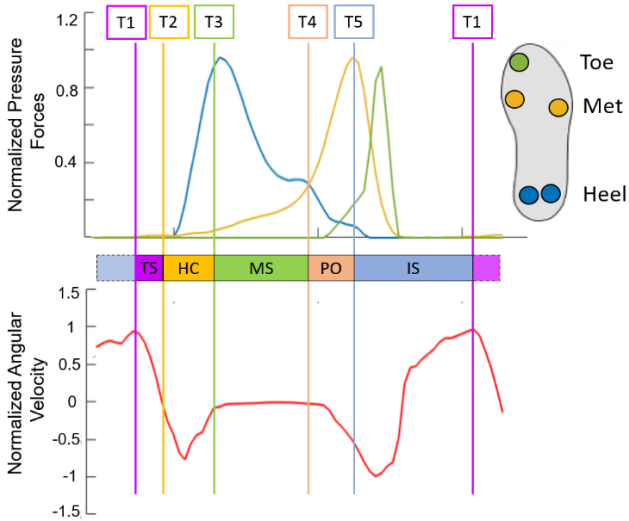

Fig. 2: Gait Teacher recordings from one gait cycle: the upper panel shows the normalized pressure forces on heels, metatarsals, and toe. Outputs from two sensors on the metatarsals (yellow) and two sensors on the heel (blue) are connected in parallel. The bottom panel shows the normalized angular velocity of the foot in the sagittal plane. Transition events T1, T2, T3, T4, and T5 are described in the text (TS-Terminal Swing, HC-Heel Contact, MS-Mid Stance, PO-Push-Off, IS-Initial Swing).

Each transition event is detected by the fulfillment of determined conditions, as reported in Table 1. The algorithm uses the signals coming from the insole (worn on the paretic side) and threshold values that are patient-dependent and are set during the calibration procedure.

TABLE 1. CONDITIONS FOR DETECTING THE TRANSITION EVENTS T1, T2, T3, T4, T5. Ω IS THE ANGULAR RATE IN THE SAGITTAL PLANE, PHEEL, PMET, AND PTOE ARE THE PRESSURES ON HEELS, METATARSALS, AND TOE. PHEEL_THRS, PMET_THRS, AND Ω_THRS ARE THRESHOLD VALUES.

T1	ω = max & *PMet* < PMet_Thrs & *PHeel* < PHeel_Thrs
T2	Zero-crossing of ω from positive to negative values
T3	ω < ω_Thrs & (*PHeel* + *PMet*) > (PHeel_Thrs+ PMet_Thrs)
T4	Intersection of *PHeel* with *PMet*
T5	(*PMet* = max || *PToe* = max || ω = min) & *PHeel* < PHeel_Thrs

B. *Rule-Based Control*

We implemented the GPD algorithm as a state machine, in which each gait phase defines a state, and conditions from Table 1 define transitions between the states. The stimulation starts when the event T4 is detected for the first time. Transitions are allowed only between consecutive states. This constraint leads to the fact that, if the algorithm misses a transition event, the stimulation remains in the current state until the same transition occurs in the following step. To avoid this mechanism, we set a time constraint on each phase duration: if a phase's duration is higher than a set time, the system enters an idle state with no stimulation, waiting for the beginning of the following step (e.g., event T4). This time constraint depends on the subject's walking speed, and the therapist chooses it among pre-selected values during the calibration of the system. The rule-based control of the FES-assistive gait training system is based on *If-Then* expressions, where the *If* statement verifies the current gait sub-phase. In contrast, the *Then* statement activates the corresponding muscular group. Thus, once the *If* the condition of the rule-based control is satisfied (i.e., the GPD algorithm determined the current phase of the system and the phase duration is not higher than the pre-set time constraint), the stimulator can generate and send the electric pulses to the corresponding channels. Each channel is connected to a surface electrode positioned on the bulk of the correspondent muscle. The muscular groups involved in the stimulation are the quadriceps (vastus lateralis and rectus femoris) as knee extensor, the hamstring as knee flexor, the tibialis anterior as dorsal flexor, and the gastrocnemius as a plantar flexor. The stimulation pattern is shown in Fig. 3.

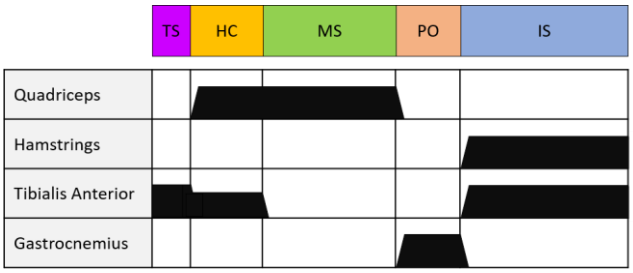

Fig. 3. Basic stimulation pattern for one gait cycle.

C. *Graphic User Interface*

We developed a Graphic User Interface (GUI) to allow the therapist to easily interact with the assistive gait system (Fig. 4). The GUI can directly communicate with the stimulator, sending and receiving data, and allows setting the system without any external assistance. It allows us to calibrate the insole, remove the offsets from the sensors, and set the amplitude of the stimulation for each muscle depending on the patient's motor and pain threshold. The user can enable the desired channels and select the basic stimulation parameters, such as the frequency and the pulse width of the stimulation. Also, from this interface, the pressure and angular velocity signals' thresholds can be manually set for each patient. Finally, the basic stimulation pattern can be modified according to patient needs. At the end of the calibration session, all the parameters can be saved and stored for the following sessions. The first calibration session lasts about 25 minutes, while the subsequent sessions' setting time is about 5 minutes.

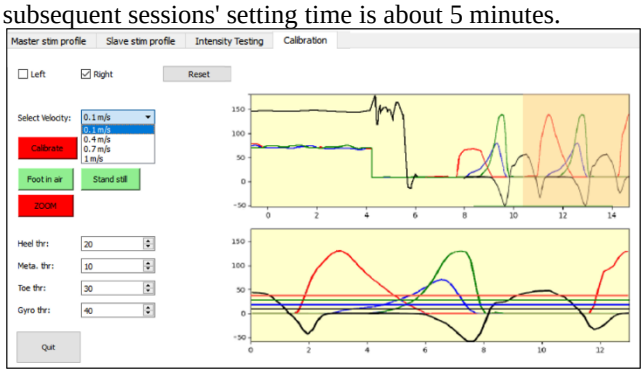

Fig. 4. Insole Calibration Tab of the GUI.

D. *Gait Phase Detection Algorithm Validation*

The Gait Phase Detection algorithm was validated using the recordings in ten chronic stroke patients to assess their efficiency and robustness. We implemented a second algorithm to perform a precise offline gait segmentation. The outputs of the online and offline algorithms were compared, and the time differences of the same events defined the time errors (Fig. 5). The time error in estimating each phase was computed both for the paretic and non-paretic limb for all the subjects. The analysis was carried out in both intra-subject (across 50 steps) and inter-subject (averaged across subjects). Due to the small sample size, we used a non-parametric statistical test to assess differences between online and offline detection; particularly, the Wilcoxon signed-rank test was employed.

E. *Proof of Concept of the FES-Assistive System*

Finally, we tested the FES-assistive gait training system on a 70-year-old man without any known motor disability. The gait pattern of older adults is similar to the gait of stroke patients, except that there is no drop-foot, and the symmetry between the legs is high. This test aimed to prove that the stimulation does not prevent normal gait and does not lead to instability. Three different modalities were tested: no stimulation, one single stimulation channel (tibialis anterior only) replicating the typical foot-drop stimulation, and 4-channel stimulation (quadriceps, hamstrings, tibialis anterior, and gastrocnemius). We compared gait characteristics as cadence and gait phases' duration between the different stimulation modalities. Moreover, we performed the analysis of signals oscillations: they were quantified by applying a moving-average low pass filter (20 samples) on the signals for the three tested modalities and computing the difference between the filtered signal and the original ones. Again, we chose a non-parametric statistical test: in this case, we used the Mann-Whitney U test.

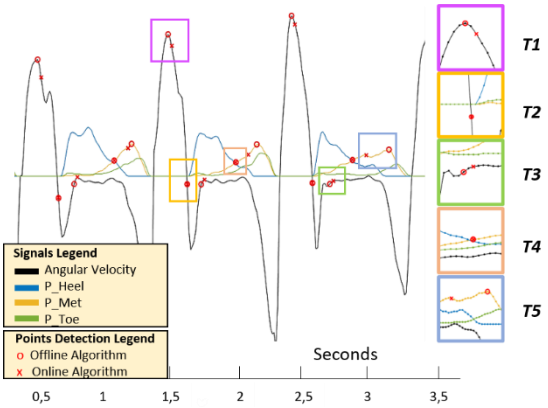

Fig. 5. Example of gait segmentation performed by the offline and the online algorithms on three gait cycles of a stroke patient. On the right, the detected events are zoomed.

III. Results

A. *Gait Phase Detection Algorithm Validation*

Signals coming from the healthy gait pattern are smoother and more regular than signals acquired from stroke patients. The GPD algorithm was tested on data collected in ten chronic stroke patients. The algorithm detected 100% of the transition events on an average of 50 steps per patient. A higher walking disability characterized three out of ten patients in terms of gait speed and asymmetries between the limbs. The time error distribution computed across each patient for both the limbs showed a low variability in detecting all the phases, except for the most impaired subjects.

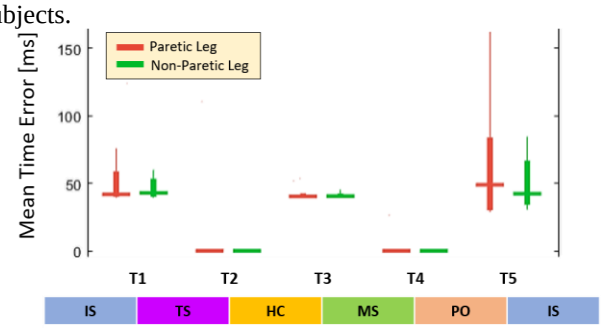

Fig. 6. Meantime error distribution across ten stroke patients in each transition event. The horizontal bar of the box plot represents the median of the population. The bold line extends from the first to the third quartile. The fine line goes from the minimum to the maximum value, excluding the outliers.

For them, the paretic limb was characterized by a large error variability, especially in detecting the beginning of the Terminal Swing (T1) and the beginning of the Initial Swing (T5). The time error was averaged across the steps of each patient to assess the variability among patients. Similarly, this analysis showed a very low variability of the time error for all the phases except for the T5 transition. Moreover, the time error distribution showed the existence of an intrinsic error due to the real-time nature of the algorithm: transitions T1, T3 and T5 had a median delay of 40ms, since the conditions for the detection of these events are based on the

derivative of the signals computed over five consecutive points (Fig. 6).

B. *FES-Assistive System Proof of Concept*

The current amplitude values were set at: 68 mA, 59 mA, 78 mA, and 68 mA for the quadriceps, hamstrings, tibialis anterior and gastrocnemius channels, respectively. The stimulation frequency was set to 40 pulses per second, and the pulse duration was 350µs. First, the cadence did not change significantly between the three stimulation modalities, although a small increase occurred in 4-channel stimulation (No stimulation, 81.1 steps/m; Tibialis Anterior stimulation, 80.1 steps/m; 4-channel stimulation, 84.1 steps/m). We evaluated the angular velocity and heel pressure force signals: in the no stimulation modality, they were characterized by more significant oscillations than in the stimulation modalities. For the angular velocity pattern, we found a statistically significant difference between the modalities with and without stimulation. In contrast, for the heel pressure force, we found a significant difference between all the modalities (Fig. 7). Finally, the phases' duration analysis showed a non-significant difference between the modalities, except for the Terminal Swing and Heel Contact phase duration. The reduction of oscillations probably reduced the Terminal Swing phase duration and increased the duration of the Heel Contact phase.

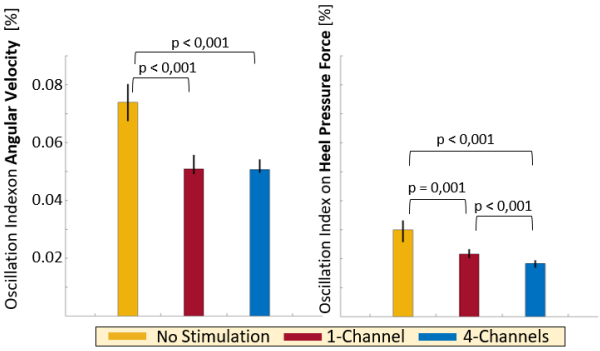

Fig. 7. Oscillation index computed on the angular velocity and the heel pressure force signals across ten gait cycles for the healthy subject. The bar value is the median of the index, and the vertical black line represents the first and third quartile of the distribution. For the statistical analysis, the Mann-Whitney U test was used.

IV. Conclusion

In the framework of FES-assistive systems for stroke patients' rehabilitation, we present a new controller for a multichannel electronic stimulator to assist gait in stroke survivors. The novelty of the proposed control system relies on combining the accurate and reliable gait information provided by the Gait Teacher insole with the modularity of the MOTIMOVE stimulator, which creates an exceptional wearable and easy-to-use solution to assist persons with hemiparesis to recover motor functions after stroke.

The Gait Teacher's signals are online processed by a GPD algorithm to split gait into five phases corresponding closely to: Terminal Swing, Heel Contact, Mid Stance, Push-Off, and Initial Swing. Five transition events, T1-T5, identify these phases. This algorithm was validated on the recordings of ten chronic stroke patients. T2 and T4 are characterized by negligible time delays, while T1, T3, and T5 detections are affected by an intrinsic time delay (40 ms) due to the algorithm's real-time nature. Nevertheless, the GDP algorithm was able to detect all the phases across all the steps of each stroke patient. The validation results were in line with the timing and accuracy requirements that the stimulation demands. The proof of concept performed on a healthy subject showed the stimulation pattern did not counteract the physiological muscle activity and seemed to work in synergy.

Moreover, some oscillations, which characterized the angular velocity signal and the heel pressure force signal, were reduced by the stimulation of the tibialis anterior during the swing phase of the gait cycle and the quadriceps muscle during the Heel Contact phase, respectively. Finally, the system's calibration from the GUI allows partial customization of the system for each subject. The gait parameters sent to the GPD algorithm before the stimulation permitted session to set the proper thresholds of the pressure and angular velocity signals. Moreover, the possibility to store the data of each patient after the first session reduces the setting time to only 5 minutes. The next step is to perform a feasibility study on stroke patients to evaluate the FES-assistive system usability in a clinical environment. Further improvements will involve combining the information coming from both insoles, allowing the implementation of more flexible and efficient rules. Moreover, the automatization of the calibration and the online adaptation of the parameters would reduce the setting time and limit the error due to a manual selection of the signal thresholds.

References

[1] Verma, R., Arya, K. N., Sharma, P., & Garg, R. K., "Understanding gait control in post-stroke: implications for management", *Journal of bodywork and movement therapies*, 16.1, 14-21, 2012, Jan.

[2] Askim, T., Indredavik, B., Vangberg, T., & Håberg, A., "Motor network changes associated with successful motor skill relearning after acute ischemic stroke: a longitudinal functional magnetic resonance imaging study", *Neurorehabilitation and neural repair*, 23.3, 295-304, 2009, Mar.

[3] Liberson, W. T., "Functional electrotherapy: stimulation of the peroneal nerve synchronized with the swing phase of the gait of hemiplegic patients", *Arch Phys Med*, *42*, 1961.

[4] Lynch, C. L., & Popovic, M. R., "Closed-loop control for FES: Past work and future directions.", In *10th Annual Conference of the International FES Society* , 2005, July.

[5] Kostov, A., Stein, R. B., Popović, D., & Armstrong, W. W., "Improved methods for control of FES for locomotion." *IFAC Proceedings Volumes*, *27*(1), 445-450, 1994, Mar.

[6] Taborri, J., Palermo, E., Rossi, S., & Cappa, P., "Gait partitioning methods: A systematic review." *Sensors*, *16*(1), 66, 2016, Jan.

[7] Kavanagh, J. J., & Menz, H. B., "Accelerometry: a technique for quantifying movement patterns during walking.", *Gait & posture*, *28*(1), 1-15, 2008, July.

[8] Kojović, J., Djurić-Jovičić, M., Došen, S., Popović, M. B., & Popović, D. B. "Sensor-driven four-channel stimulation of paretic leg: functional electrical walking therapy", *Journal of neuroscience methods*, *181*(1), 100-105, 2009, June.

[9] Popović, D.B. and Popović Maneski, L., "The instrumented shoe insole for rule-based control of gait in persons with hemiplegia". *EasyChair Preprint*, p.1345, 2019.

[10] 3F-Fit Fabricando Faber, https://www.3-x-f.com/. Accessed 13/07/2020.

V. Acknowledgment

This study was financially supported by the Ministry of Education, Science and Technological Development of the Republic of Serbia, Agreement with the Institute of Technical Sciences SASA, Grant No. 451-03-68/2020-14/200175 and the Grant F-137 from SASA.

Surface EMG for the Assessment of the Gait Performance in Hemiplegic Patients

Ivan Topalović, Suzana Dedijer Dujović, Ljubica Konstantinović and Dejan B. Popović, *Member, IEEE*

***Abstract*— We developed a method for assessment of the gait regularity in hemiplegic patients. We used a fully wearable system comprising ground reaction force sensors and inertial measurement units to record the dynamics and array electrodes and multichannel amplifiers for electromyography (EMG) mapping of activity of *tibialis anterior m*. during the gait. The fuzzy logic was applied to ground reaction force signals for estimating the gait symmetry. This paper introduces a new parameter for estimation of symmetry of muscle activities in the ipsilateral and contralateral legs based on the entropy of EMG maps. The presented method forms a set of gait parameters for quantifying the regularity of the patient's gait. The set of parameters are of interest for the assessment of the efficacy of the therapy.**

***Index Terms*—gait, EMG, EMG maps, IMU, wearable technology, drop foot**

I. Introduction

Cerebrovascular lesion in most cases leads partial paralysis of one side of the body (hemiplegia). Hemiplegia comprises an irregular posture, unevenly distributed support on legs when standing, slow and asymmetrical gait, rapid onset of fatigue, etc. [1].

The motor status of a hemiplegic patient can be assessed by the analysis of the gait regularity. There are a several scales for gait assessment: Rivermead Visual Gait Assessment (RVGA), Salford Gait Tool (SGT), Observational Gait Scale (OGS), Clinical Gait and Balance Scale (GABS), etc. [2]. The listed clinical scales are largely based on the visual observations made by the clinician.

Technological progress led to the reproducible and examiner independent methods for gait quantification. Different types of instrumentation are in use: sensor platforms for measuring the reaction forces of the ground and cameras with reflective markers for recording movement [3], inertial measurement units (IMU), and insoles for shoes with force sensors [4], walking paths with sensors [5], etc. These systems provide various information about gait mechanics: joints angles, angular velocities, ground reaction forces, etc. [6]. Electrophysiological signals (e.g., electromyography – EMG) carry important information about the motor systems responsible for the gait [7]. The combination of physiological signals and gait mechanics gives the possibility of qualitative and quantitative gait analysis, which includes the analysis of the movement actuators and its mechanics.

We presented a method for gait assessment based on temporal parameters [8, 9]. To obtain these parameters (gait cycle, step cycle, swing phase, stance phase, double support phase, and cadence) we used shoe insoles with built-in pressure sensors and IMUs to analyze gait mechanics and determine the characteristic moments that represent the boundary between individual gait phases. We showed in another study [10] the upgraded method where the EMG mapping was included. We have shown that there are significant differences between the intensities of EMG in specific regions on the paretic and nonparetic leg. We showed the presence of symmetrical shapes in EMG maps of ipsilateral and contralateral extremities and lack of intensity in the paretic side relative to nonparetic [11, 12]. As EMG maps represent digital images, in [13] we have shown the implementation of digital image processing techniques for analysis of EMG maps.

In this paper we presented the method for gait assessment based on temporal gait parameters and EMG mapping. The method quantifies the gait symmetry in electrical activities of muscle *tibialis anterior* (TA) in legs during the gait of hemiplegic patients. The TA muscle is responsible for lifting the toes. The lack of activity of the TA results with the drop foot and the gait starts to be abnormal since the toes are catching the ground during the swing phase of the gait cycle. We used the recordings of mechanical and EMG signals from the gait of a group of hemiplegic patients before and after standard medical treatment in the rehabilitation.

II. The Method

A. Instrumentation

To record monopolar EMG signals from the TA on both legs we used two custom designed circular 24-pad electrodes (d = 8 mm). Pads were fixed in 6 rows with different number of pads (5 pads in 1st and 2nd row, 4pads in 3rd and 4th row, and 3 pads in 5th and 6th row). Arrays were made of SA9327 EKG/EMG Ag-AgCl commercially available electrodes (Thought Technology Ltd., Montreal, QC, CA). All pads were

Ivan Topalović is with Institute of Technical Sciences of SASA, Knez Mihailova 35, 11000 Belgrade, Serbia (e-mail: topalovic_ivan@yahoo.com)

Suzana Dedijer Dujović is with the Clinic for rehabilitation "Dr Miroslav Zotović", Sokobanjska 13, 11000 Belgrade (e-mail: suzanadedijer@yahoo.com)

Ljubica Konstanitinović is with the Medical Faculty, University of Belgrade and Clinic for rehabilitation "Dr Miroslav Zotović", Sokobanjska 13, 1100 Belgrade (e-mail: ljubicakonstantinovic@yahoo.com)

Dejan B. Popović is with the School of Electrical Engineering, University of Belgrade, 73 Bulevar kralja Aleksandra, 11020 Belgrade, Serbia and Serbian Academy of Sciences and Arts (e-mail: dbp@etf.rs).

covered with AG936 conductivity gel (Axelgaard Manufacturing Co. Ltd., Lystrup, DK). We used disposable pre-gelled EMG Ag/AgCl electrodes with 10 mm flat pellets, Covidien BRD H124SG (Covidien, Medtronic, Dublin, IR) as ground and reference electrode.

Array electrodes were connected to two wearable 24-channel amplifiers Smarting® (https://mbraintrain.com/). The Smarting was designed for monopolar recordings of the cortical activities (brain-computer interface – BCI). Due to Bluetooth connection with PC Smarting has sampling rate limit at 500 Hz per channel. This limitation does not satisfy Nyquist criterion for EMG signals, but we validated the applicability of the Smarting® for estimation of EMG envelopes by comparing the recordings with the signals acquired by a professional EMG amplifier BioVision (BioVision, Wehrheim, DE) [14]. For recordings, we used the proprietary software of the Smarting®. Each Smarting system was connected to a separate PC.

For the recording of the gait mechanics we used instrumented insoles (Gait Teacher, https://rehabshop.rs/). Each insole comprises five pressure sensors and one IMU to record accelerations and angular velocities in all three directions. Insoles have wireless connection with PC. For the signal acquisition, we used the proprietary software of the Gait Teacher. In this study we used signals from the pressure sensors that are highly correlated with the ground reaction forces.

All three recording systems (two PCs with smarting systems and one PC connected to insoles system) were synchronized by Lab Stream Layer platform, which collects data from available streams from PCs connected in the same Local Area Network.

B. Subject and Procedure

One hemiplegic patient (female, 72-years, 175 cm, 71 kg, right side hemiplegia, uses four-legged cane) participated in our key study. She signed the informed consent approved by the ethics committee of the Clinic for rehabilitation "Dr Miroslav Zotović"). The whole procedure was supervised by a physiatrist.

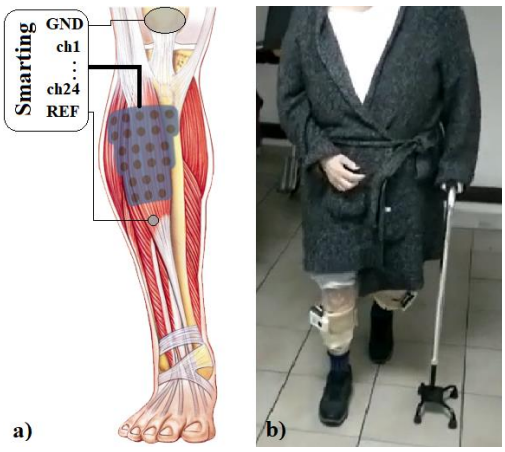

Fig. 1. a) Schematics of the electrode placement: array electrode was covering the region over TA muscle; ground electrode was placed over bony part of knee and the reference electrode was placed under the array along the longitudinal axis; b) Patient with experimental setup.

The array electrodes were placed symmetrically on both legs, covering the TA regions. Longer edge of the electrode was placed along the tibia, top of the electrode at 20 mm from the tibial tuberosity (Fig. 1). Ground electrodes were placed over *patella*, and reference electrodes were placed under the array electrodes, 10 mm along the longitudinal axis.

Subject's task was to walk in a straight line to cover the distance of 10 m. Before the recording subject was asked to stand with evenly distributed weight on both legs (as much as it was possible). Subject was asked to start and stop the gait on an auditory signal. The subject was asked to walk with the gait rate that she felt comfortable. The procedure was repeated three times in one session before and after three weeks of the therapy.

C. Data Processing

An original software in Matlab R2015a (MathWorks, Inc., Natick, MA, US) was used for processing.

We applied fuzzy logic on signals from pressure sensors to estimate the heel contact (HC; beginning of the stance phase) and toes off (TO; beginning of swing phase) moments. Detailed explanation can be found in [8, 9]. We estimated the following parameters: gait cycle (GC) – time between the two consecutive HC of the same leg; step cycle (SC) – time between the HC of the ipsilateral leg and the HC of the contralateral leg; stance phase (STP)– time between the HC and the TO of one leg; swing phase (SWP)– time between TO and HC of one leg; double support phase (DSP) – time when both legs are contacting the ground; gait cadence (GCD)– number of steps per unit time.

We applied high pass Butterworth filter (2nd order, cutoff frequency at 30 Hz) to EMG signals to stabilize the baseline and notch Butterworth filter (3rd order) at 50 Hz to minimize the impact of noise coming from the power lines. To remove the artefacts incurred during a heel strike we used FastICA method [15]. Recorded signals $\boldsymbol{x}$ (surface EMG) with artifacts can be represented as:

$$\boldsymbol{x} = \boldsymbol{A}\boldsymbol{s}; \tag{1}$$

$$\boldsymbol{x} = \begin{bmatrix} x_1 \\ \vdots \\ x_n \end{bmatrix}; \boldsymbol{s} = \begin{bmatrix} s_1 \\ \vdots \\ s_n \end{bmatrix}; \boldsymbol{A} = \begin{bmatrix} a_{11} & \cdots & a_{1n} \\ \vdots & \ddots & \vdots \\ a_{n1} & \cdots & a_{nn} \end{bmatrix};$$

where $\boldsymbol{s}$ are original activities of particular sources and $\boldsymbol{A}$ is the mixing matrix (matrix of constants).

Using the ICA algorithm, the weight factors $\boldsymbol{W}$ are calculated such that the separated components $\boldsymbol{u}$ are maximally statistically independent:

$$\boldsymbol{u}(t) = \boldsymbol{W}\boldsymbol{x}(t) = \boldsymbol{W}\boldsymbol{A}\boldsymbol{s}(t) \tag{2}$$

Fig. 2 shows the decomposition of 24 EMG signals from one array electrode (only one channel is shown on the top panel due to limited space) to 24 independent components (maximum number of components). Among the obtained components $\boldsymbol{u}$ (middle panel) the components with artifacts

stand out (examples are marked with red circles).We detected components that mostly contain artifacts, using visual inspection, and removed them manually, equating them with zero. After the components are deleted, the inversion reconstructs the EMG signals based on the remaining components:

$$\boldsymbol{x}(t) = \boldsymbol{W}^{-1}\boldsymbol{u}(t) \tag{3}$$

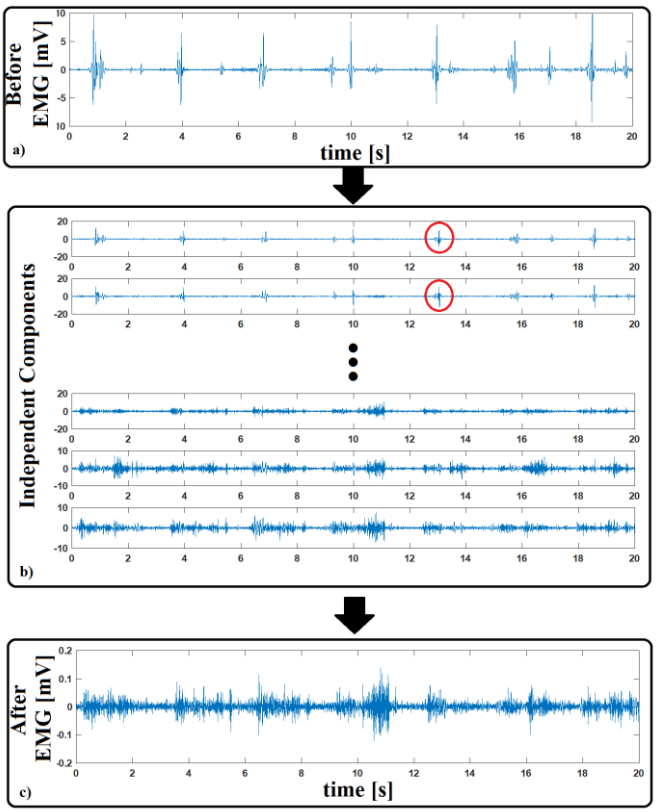

Fig. 2. Removing heel contact artefacts from EMG signals by applying ICA method. a) The example of EMG signal with significant moving electrode artefacts incurred during a heel strike; b) The independent components obtained from 24 EMG channels from the same array electrode; c) The EMG signal with removed artefacts.

We applied low pass Butterworth filter (3rd order, cutoff frequency at 3 Hz) on absolute value of EMG signals to estimate the EMG envelopes. All envelopes were normalized relative to maximal value of all channels in the analyzed sequence.

We used EMG envelopes to obtain the EMG maps. Similar to method we used in our previous researches [13], we applied bicubic ("spline") interpolation to current envelope samples from the same array electrode. The only difference was in initial matrix, due to different shape of array electrode. The EMG maps were formed based on the template matrix (72x101 pixels – one pixel corresponds to 1x1mm of array electrode) that contains three groups of pixels (Fig. 3): 24 original pixels with the envelope samples, placed in appropriate place due to pads order; pixels interpolants; and empty pixels that exceed the array electrode.

Algorithm took the samples of EMG envelopes from same array electrode in the same moment (1 sample per channel – 24 samples in total) and arranged them in appropriate pixels in the template. In next step, algorithm applied interpolation and assigned the scale of colors (deep blue is region without activity and deep red is region with highest activity). Assigning colors is used just for visualization of EMG maps, but it is not a part of further calculations.

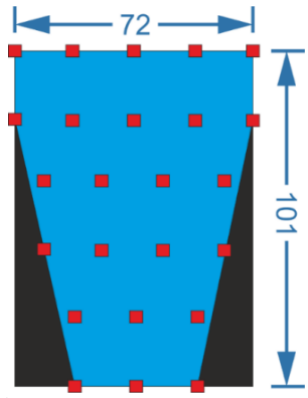

Fig. 3. Template for EMG map interpolation: red squares represent the 24 original data set; blue region represents the pixels interpolants and black region are the empty pixels that exceed dimensions of array electrode.

To ensure better repeatability of EMG maps from step to step, EMG maps were calculated by averaging of 11 samples from each channel, in the vicinity of HC (5 samples before, HC moment and 5 samples after). The number of samples is determined heuristically. Since it is difficult to estimate the appropriate moment from EMG envelopes on the paretic foot, the detection was performed based on signals from the insoles, in which the desired HC is clearly distinguished.

We calculated entropy of digital image as:

$$Ent = -\sum_{i=0}^{n-1} p_i \log p_i \tag{4}$$

where n is number of intensities in the color scale, and p_i is the probability expressed in number of pixels with intensity i. Based on the individual entropies, the mean entropy values for the nonparetic and paretic leg were calculated. A coefficient representing their ratio was calculated, according to the formula:

$$\frac{\overline{Ent_l} - \overline{Ent_r}}{\overline{Ent_l} + \overline{Ent_r}} \tag{5}$$

where $\overline{Ent_l}$ and $\overline{Ent_r}$ are mean entropy values for EMG maps from left and right leg, respectively.

III. Main Results

Figure 4 shows the example of signals from pressure sensors and median of EMG envelopes from nonparetic and paretic leg for seven full gait cycles. Figure also shows sequences of EMG maps on both sides in characteristic moment of gait which are marked with red dots.

In Figure 5 are shown the examples of EMG maps from nonparetic (top left) and paretic (bottom left) leg and their histograms (right).

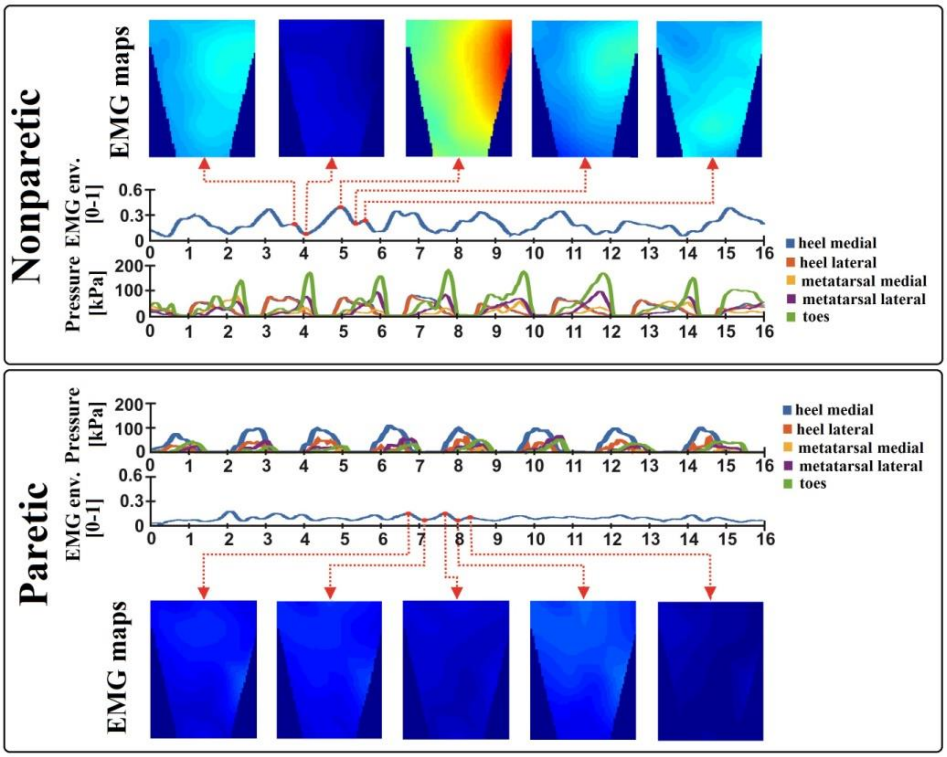

Fig. 4. Signals from pressure sensors and median of EMG envelopes from nonparetic leg (top panel) and paretic leg (bottom panel) for seven full gait cycles; Example shows the sequences of EMG maps on both legs obtained in characteristic moments, marked with red dots. Significant difference can be noticed in signals and EMG maps on paretic and nonparetic side.

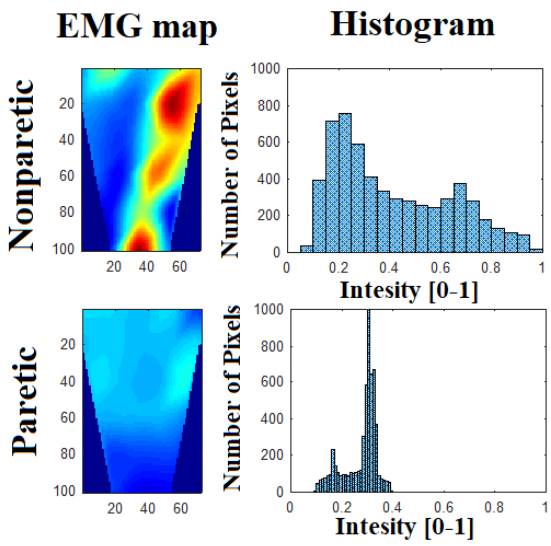

Fig. 5. Examples of EMG maps from nonparetic (top left) and paretic (bottom left) leg and their histograms (right). There is noticeable difference between histograms: histogram on paretic side is more concentrated around one peak, while histogram on nonparetic side wights to uniform distribution.

In Table I are presented the mean values of gait parameters and EMG map entropies obtained from signals recorded before and after therapy. Gait cycle (GC) and Step Cycle (SC) are given in seconds, Swing phase (SWP) and Stance phase (STP) are given as percent of Gait cycle, Gait cadence (GCD) is given in steps per second, Double support phase (DSP) is presented as percent of a Gait cycle and EMG entropy is represented in arbitrary values.

TABLE I
GAIT PARAMETERS AND EMG MAP ENTROPY

		GC [s]	SC [s]	SWP [%]	STP [%]	DSP [%]	GCD [step/s]	Entropy [arb.]
Bef.	L	2.30	0.62	10.3	89.7	50.4	56.27	5.12
	R	2.29	0.61	26.9	73.1	15.7		3.46
Aft.	L	1.86	0.58	17.5	82.5	38.7	70.51	5.43
	R	1.80	0.56	29.8	70.2	17.2		4.07

Figure 6 shows the main ratio between swing and stance phase for paretic and nonparetic leg before and after therapy (left panel) and ratio of EMG entropies on left and right leg before and after therapy (right panel).

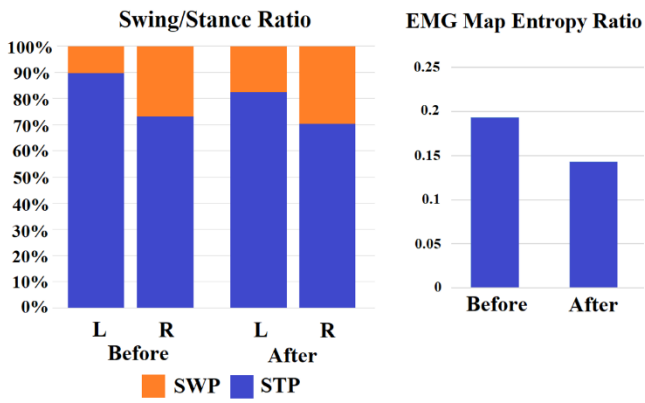

Fig. 6. Main ratio between SWP and STP for paretic and nonparetic leg before and after therapy (left panel) and ratio of EMG map entropies between left and right leg before and after therapy.

IV. Discussion

In Figure 4 it is noticeable that the pressure distribution during the STP arises in an irregular rhythm on the paretic leg (all signals rise simultaneously from the HC moment). Segments in which the pressures are equal to 0 represent the SWP and it can be noticed that their duration differs on the paretic and nonparetic leg: the SWP is shorter on the nonparetic leg, because the subject tends to rely on the nonparetic leg as soon as possible. These differences in signals on both sides indicates to irregular and asymmetrical gait.

In Figure 4 significant difference in EMG activity between nonparetic and paretic leg can be noticed: mean envelope on nonparetic side has relatively repetitive pattern with local maxima at HC moment, while on paretic side EMG envelopes have irregular pattern and noticeably lover amplitude. This difference reflects to EMG maps (Figure 4 top and bottom). Beside lower intensity, EMG maps on paretic side don't have clearly defined high intensity regions, and activity spreads all over the EMG map. This can be explained as patients attempt to make a movement by compensatory mechanism, due to poor innervation of targeted muscle. The EMG maps and histograms in Figure 5 illustrate this scattering of EMG activity. Histogram of nonparetic EMG map wights to uniform distribution because the pixels of the EMG map have various intensities. On the other hand, histogram of the EMG map from paretic side is concentrated around one peak, because the majority of the pixels have same intensity (color).

These differences in intensity distribution are clearly quantified by calculating entropies. The values shown in Table I: 5.12 for nonparetic and 3.46 for paretic leg before the therapy. The greater entropy is the histogram is closer to uniform distribution, which means more different colors in EMG map. After the therapy, difference between entropies are lower, which indicates patient's improvement and greater selectivity in muscle recruitment. The EMG map entropy ratio shown in Figure 6 represents the symmetry of patient's activities on paretic and nonparetic leg and level of selectivity for muscle recruitment. Due to equation (5), in ideal case this ratio would be 0 which would mean that both legs have the same selectivity (entropies are equal on both legs).

Global improvement can be noticed in gait parameters in Table I: patient walks faster (GCD is greater and GC and SC are shorter), but also symmetry is improved (difference between duration of SWP and STP on paretic and nonparetic leg are lower; Figure 6 left panel).

V. Conclusion

The proposed method, which combines the use of pressure sensors with EMG array electrodes and portable amplifiers, provides a good base for gait analysis. The formed set of parameters, based on gait mechanics, and spatio-temporal images of muscle activity during gait (both as a visual assessment and quantified), gives the possibility to assess the patient's condition before and after therapy.

Acknowledgment

This research was supported by the grants III4008 and TR35003 from the Ministry of Education, Science and Technological development of Serbia. The experimental protocol was approved by ethical committee of the Clinic for rehabilitation "Dr Miroslav Zotović" in Belgrade, Serbia.

VI. References

[1] D. B. Popović and T. Sinkjær, Control of movements in humans: systems and mechanisms, Belgrade: Academic Mind, 2015.

[2] C. Ridao-Fernández, E. Pinero-Pinto and G. Chamorro-Moriana, "Observational gait assessment scales in patients with walking disorders: systematic review," *BioMed research international, vol.* 2019, pp. 12, 2019.

[3] K. Aminian, C. Trevisan, B. Najafi, H. Dejnabadi, C. Frigo, E. Pavan, A. Telono, F. Cerati, E. C. Marinoni, P. Robert and P. F. Leyvraz, "Evaluation of an ambulatory system for gait analysis in hip osteoarthritis and after total hip replacement," *Gait & posture,* vol. 20, no. 1, pp. 102-107, 2004.

[4] S. J. M. Bamberg, A. Y. Benbasat, D. M. Scarborough, D. E. Krebs and J. A. Paradiso, "Gait analysis using a shoe-integrated wireless sensor system," *IEEE transactions on information technology in biomedicine,* vol. 12, no. 4, pp. 413-423, 2008.

[5] B. Bilney, M. Morris and K. Webster, "“Concurrent related validity of the GAITRite® walkway system for quantification of the spatial and temporal parameters of gait," *Gait & posture,* vol. 17, no. 1, pp. 68-74, 2003.

[6] I. Milovanović and D. B. Popović, "Principal component analysis of gait kinematics data in acute and chronic stroke patients," *Computational and mathematical methods in medicine,vol. 2012, pp. 8,* 2012.

[7] A. Strazza, A. Mengarelli, S. Fioretti, L. Burattini, V. Agostini, M. Knaflitz and F. Di Nardo, "Surface-EMG analysis for the quantification of thigh muscle dynamic co-contractions during normal gait," *Gait & Posture,* vol. 51, pp. 228-233, 2017.

[8] I. Topalović and D. B. Popović, "Estimation of gait parameters based on data from inertial measurement units," in *Procceedings of 4th IcETRAN,* Kladovo, Serbia, 05-08. June, 2017.

[9] J. Milovanović, M. Gavrilović, I. Topalović and D. B. Popović, "Influence of two weeks balance practice with feedback on the gait in hemiplegic patients," in *IcETRAN & ETRAN*, Palić, Serbia, 11-14. June, 2018.

[10] D. B. Popović, I. Topalović, S. Dedijer Dujović and L. Konstantinović, "Wearable system for the gait assessment in stroke patients," in *International Conference on NeuroRehabilitation. Springer, Cham,* 2018.

[11] L. Popović Maneski, I. Topalović, N. Jovičić, S. Dedijer, L. Konstantinović and D. B. Popović, "Stimulation map for control of functional grasp based on multi-channel EMG recordings," *Medical engineering & physics,* vol. 38, no. 11, pp. 1251-1259, 2016.

[12] L. Popović-Maneski and I. Topalović, "EMG Map for Designing the Electrode Shape for Functional Electrical Therapy of Upper Extremities," in *Masia, L., Micera, S., Akay, M., Pons, J.L. (Eds.),Converging Clinical and Engineering Research on Neurorehabilitation III, Biosystems & Biorobotics,* Pisa, Italy, Springer International Publishing, 2019, pp. 1003-1007.

[13] I. Topalović, S. Graovac and D. B. Popović, "EMG map image processing for recognition of fingers movement," *Journal of Electromyography and Kinesiology,* vol. 49, p. 102364, 2019.

[14] I. Topalović, M. Janković and D. B. Popović, "Validation of the acqusition system Smarting for EMG recordings with electrode arry," in *Proceedings of 2nd Ic ETRAN,* Srebrno Jezero, 08-11. June, 2015.

[15] A. Hyvärinen, "Fast and Robust Fixed-Point Algorithms for Independent Component Analysis," *IEEE Transactions on Neural Networks,* vol. 10, no. 3, pp. 626-634, 1999.

Cyclograms Based on Principal Components for Assessing the Gait

Marija M. Gavrilović, Dejan B. Popović, *Member, IEEE*

***Abstract*—Objective measure of the gait quality is essential for evaluating the therapeutic protocol's effects on stroke patients' rehabilitation. We present a new proposal for assessing the gait, which uses the principal component analysis (PCA) of feet kinematics and ground reaction forces (GRF) data. The data have been acquired by the Gait Master comprising five GRF sensors and 6D inertial measurement units (IMU) per insole. The PCA reduces the 22-time series output from two insoles and generates cyclograms, allowing qualitative analysis of the pathologic and healthy gait differences. We suggest that cyclograms in the space with principal components on the axis provide useful information to the clinician about the gait performance. Five volunteers with no known motor impairment participated in the determination of the regular pattern. We tested the method in a small series of patients after stroke using the pattern of healthy as a standard. The results suggest that the PCA analysis provides a good measure of gait quality.**

***Index Terms*—Gait; Stroke; Cyclograms; Principal component analysis (PCA); Inertial measurement unit (IMU); Ground reaction force (GRF).**

I. Introduction

THE characterization of gait in persons with motor disabilities is instrumental in selecting the most effective therapeutic protocol. The characterization can be performed based on data acquired during the gait. The data of interest are the ground reaction forces (GRF) and leg segments' kinematics since they fully define the biomechanics.

The precise measurement of leg segments' ground reaction forces and kinematics can be done in the specialized laboratories instrumented with camera systems and force plates [1, 2]. The difficulty is that the recording process requires a specialist's participation with the experience in acquiring motion data and setting the markers on the appropriate places at the body. The gait laboratory setup is designed for only straight-line walking, and GRF is acquired for one or two steps. The alternative to the recordings in the gait laboratories is to implement a wearable system [3-7]. Wearable systems combine sensors integrated into shoe insoles and inertial measurement units (IMU) that measure the acceleration and angular rates of body segments. Information from all sensors must be synchronized, which is not the most trivial task because of the time delays and lost packages when wireless technology is used. The difficulty is that sensors integrated into insoles, although being much improved (availability of new materials and miniaturization of electronics and wireless communication) measure only total ground reaction forces and have hysteresis, delay, and insufficient robustness when the temperature and humidity change. The recently introduced Gait Master system [8] with several industrial quality GRF sensors and IMU provides versatility comparable with the force plates in the gait laboratories. The data from the insoles is stored in a time-stamped format for off-line analysis. The set of data comprises the 22-time series. This data is sufficient to determine gait parameters [1, 2]. Table I shows the typical collection of data that can be estimated from a wearable system.

TABLE 1: FEATURES IN GAIT ANALYSIS

Gait Feature	Definition
Walking Speed	The average speed while the subject is walking
Cadence	Average steps per minute while walking
Swing Time	The transition time of the foot from lift to landing
Stance Time	The transition time of the foot from landing to lift
Stride Length	The distance between the heel contacts of the ipsilateral foot and contralateral foot
Step length	The distance between two consecutive heel contacts of the same foot
Ground reaction force	The distribution of the GRF over the sole
Symmetries	Differences between the same events in ipsilateral and contralateral legs

The reason for the quantification of the gait is the objective assessment of the performance. However, there is no golden standard what is the normal performance. Young people have different gait patterns than persons of older age. Females have different gait patterns influenced by the type of shoes used, etc. [9].

Methods used in clinical studies compare the measured features between before and after the therapy, or between different therapeutic protocols. The comparison is statistically analyzed, and significant differences are used as measures.

Another method to use gait data is to form cyclograms. Cyclograms are a spatial presentation where two or more recorded signals (e.g., hip and knee angles; hip, knee, and ankle angles) are the coordinate system axes. The cyclograms can be used to analyze the different gait modalities and compare healthy vs. pathologic gait [10].

Marija M. Gavrilović, Ph.D. student, Faculty of Electrical Engineering, University of Belgrade, Bulevar kralja Aleksandra 73, 11000 Belgrade, Serbia, (e-mail: marijapetrovic48@yahoo.com).

Dejan B. Popović is with the Serbian Academy of Sciences and Arts, Knez Mihailova 35, 11000 Belgrade, Serbia, and Aalborg University, Department of Health Science and Technology, Denmark (e-mail: dbp@etf.rs).

We introduce here the method which uses cyclograms generated in the space of principal components calculated from data recorded during gait. The principal components analysis (PCA) reduces the 22-time series recordings to a set of orthogonal values that can be used for the creation of a two-dimensional cyclogram. In principle, the analysis can look into three or more dimensional cyclograms.

The method that we present, PCA, was applied to sets of data separately for the left and right legs. Data recorded were considered as sequences of stochastic events. The reason for developing this method for representing the gait performance follows the previous research in applying PCA to analyze kinematic data [11].

We illustrate the method by using data recorded in healthy and patients with stroke. Besides, we associate a numerical measure calculated from the cyclograms to be a classifier of difference between the healthy and pathologic gaits.

II. Methods and Instrumentation

A. Instrumentation

We used Gait Master insoles [8] with five GRF sensors and the one 6D IMU per insole. The insoles use the hardware built around MPU-6050 (16-bit conversion). Each insole includes a wireless communication circuit allowing real-time data transfer at 100 Hz (11 signals per insole) to the host computer at distances up to 30 m. The LabView environment's proprietary acquisition software provides online data with the delay of 50ms and stores data in a time-stamped format for off-line analysis. The program has a graphical user interface (GUI), allowing the clinician to intuitively operate the system.

1) Subjects

Six healthy volunteers participated in this study. They were considered healthy since no known sensory-motor impairment was reported or known from their health record. Four patients with stroke were recruited. The measurements were performed in the Clinic for rehabilitation "Dr. Miroslav Zotović“, Belgrade, Serbia. All patients signed an informed consent approved by the board of the Institute. Patients participated in testing the efficiency of the functional electrical stimulation assisted pedaling.

B. Procedure

Subjects were asked to walk at their normal walking pace. They repeated walking over a 5m flat surface two times. If necessary, they would rest between the trials.

C. Signal processing

Steps extraction and the stance and swing detections were done based on the threshold method for detecting heel strike and toe-off events. The threshold was set to be 5% of the maximum value from the GRF signal from the heel and the toes' lateral side. The first and last steps were excluded from further analysis. The singles used in the principal component analysis were the angular velocity in the sagittal plane (GyroY), the acceleration in the direction of sole (AccX), and the direction orthogonal to the sole (AccZ), and the all five ground reaction forces individually (GRF). The signals were selected based on the heuristic analysis of all 11 signals measured by each insole. We normalized the signals to make them have the unit variance.

The PCA allowed the mapping of the original data into orthogonal space, where the principal axis is the direction of the data's maximal deviation [12]. The analysis includes calculating the correlation matrix, extraction of the application of the principal component of the varimax rotation, and calculation of factor scores. The number of principal components we used in this study was chosen based on Kaiser's proposed method [13]. We retained only elements in which the eigenvalues were more significant than one. The Bartlett's test of sphericity showed that data was suitable for PCA.

The proposed method uses 2D cyclograms in the space of the first two principal components. Cyclograms were compared for consecutive steps for different gait categories. These cyclograms are the image representation for the gait performance assessment.

We defined the quantitative parameter d, as shown in Eq. 1:

$$d = {d_{PC1_{stance}}}/{d_{PC2_{stance}}} * {d_{PC2_{swing}}}/{d_{PC1_{swing}}} \quad (1)$$

where $d_{PC1_{stance}}$ is the maximal distance on the PC1 axis between points on cyclograms for the stance phase. Similarly, $d_{PC1_{swing}}$ is the distance for the swing phase, while PC1 and PC2 subscripts represent the distance on the PC1 and PC2 axis, respectively (Fig 1).

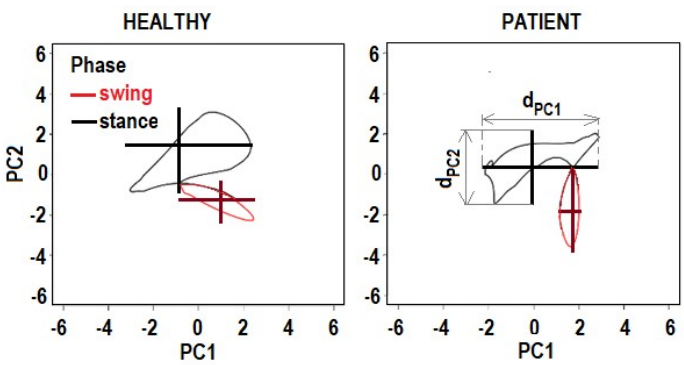

Fig.1. Sketch of the parameters defining the cyclogram that can be automatically calculated. The left panel shows a characteristic pattern for one leg during healthy gait. The right panel shows an example of the non-paretic limb during the gait of a patient.

III. Results

Fig. 2 shows the processed data and a characteristic single step for a person's left leg with no known sensory-motor impairment.

Fig. 2 shows the processed data for about eight seconds (left panel) and extracted data for a single step for a person's left leg with no known sensory-motor impairment (right panel).

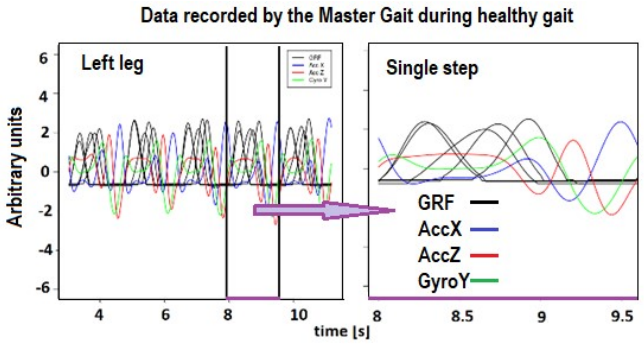

Fig.2. An example of the eight signals extracted from the 22-time series was recorded with the insole in the left shoe during a healthy person (left panel). The right panel shows the processed and standardized data for a single step. Acronyms AccX (blue) and AccZ (red) are used to the accelerations in the direction of the sole, and the direction orthogonal to the sole, GyroY (green) is denoting the angular rate of the foot in the sagittal plane, and GRF (five black lines) are five signals from the GRF sensors.

Left panels in Fig. 3 show the first two principal components (PC 1 and PC 2) vs. time. The right panels in Fig. 3 are cyclograms in the two-dimensional PCA space (PC1 and PC2, the horizontal and vertical axis). The black color shows the stance phase, while the red color indicates the swing phase.

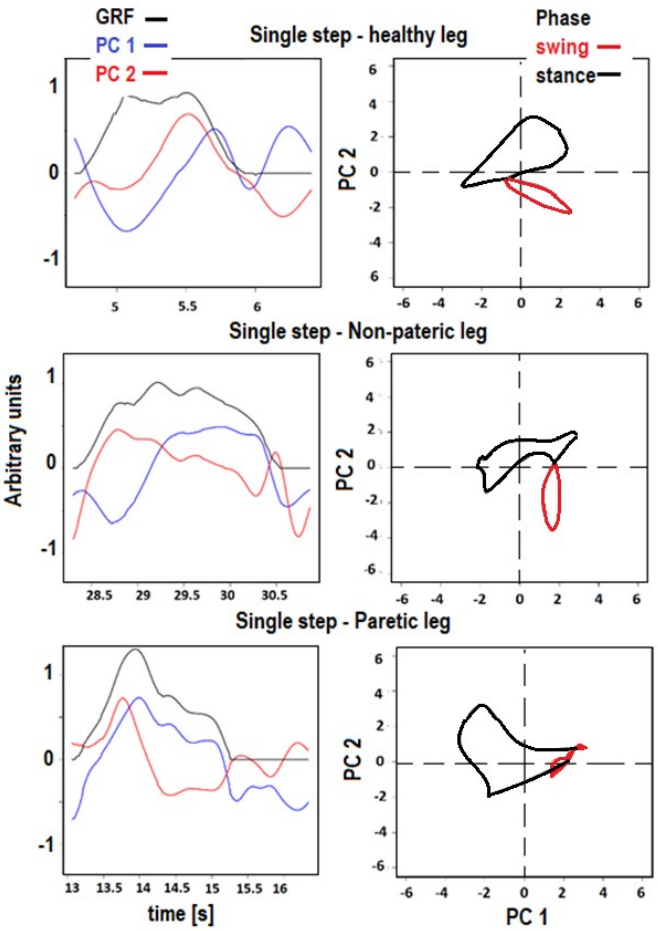

Fig.3. Left panels show the first two principal components (PC 1, PC 2) and the sum of all five sensors (GRF). The right panels show PCA cyclograms for a single gait cycle

and use two colors for distinguishing between the swing and stance phases. The upper row uses data from the left leg of a healthy subject. There is a distinct difference in the cyclograms for both paretic and non-paretic legs compared with the cyclogram for healthy gait patterns.

Fig. 4 shows the variability of cyclograms for four consecutive steps.

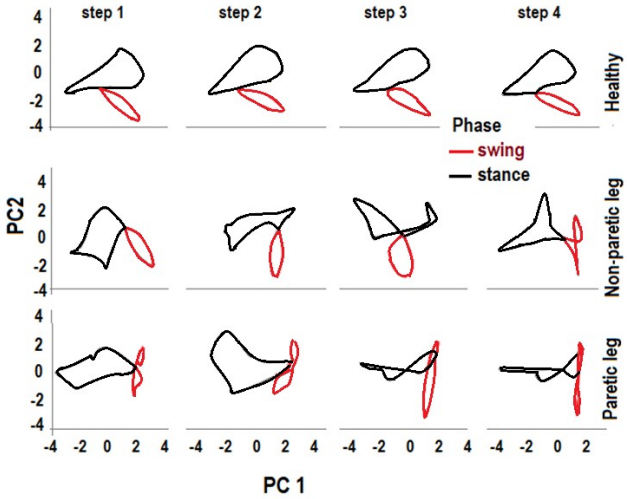

Fig.4. Cyclograms for four consecutive steps. The first row shows cyclograms for the left leg of a person with no known sensory-motor impairment. The second and third rows are cyclograms for a patient's non-paretic and paretic leg after stroke. Red lines are used to the swing phases and the black lines for the stance phases.

The top panels show a healthy pattern, the second row shows the non-paretic leg, and the bottom panels represent the paretic limb. The red color indicates the swing phases, while the black lines show each step's stance phases.

Fig. 4 indicates that there is a small variability from step to step in a healthy gait. There are significant differences between cyclogram in patients for the paretic and non-paretic legs. There is a high variability from step to step, especially noticeable in the cyclograms for the paretic limb.

In conclusion, the pathological gait patterns have different cyclogram shapes than healthy gait patterns, and they have more substantial shape variability from step to step.

TABLE II. THE VALUES OF THE RATIO OF LENGTHS d_{PC1} AND d_{PC2} FOR FOUR CONSECUTIVE STEPS OF A HEALTHY AND PATIENT N°1 FOR THE STANCE AND THE SWING PHASES

	Healthy – left leg		non-paretic		Paretic	
	stance	swing	stance	swing	stance	Swing
Step 1	1.4	1.1	1.2	0.6	1.8	0.2
Step 2	1.2	1.7	0.9	0.3	1.2	0.7
Step3	1.3	2	1.3	0.8	2.3	0.2
Step 4	1.3	1.9	1.1	0.5	2.2	0.3
Mean±SD	1.3±0.1	1.7±0.4	1.1±0.2	0.5±0.2	1.9±0.4	0.3±0.3
d ± SD	0.8±0.2		2.3±0.6*		7.8±5.6*	

Data for four steps for the healthy gait and one patient are in Table I. The columns are the values of the d_{PC1} and d_{PC2}. The data for one leg of a healthy gait and non-paretic and paretic sided of one patient with stroke. The asterisks annotate the significant difference.

TABLE III. THE MEAN AND STANDARD DEVIATIONS OF d (RATIO OF d_{PC1} AND d_{PC2}) FOR ALL CONSECUTIVE STEPS FOR A HEALTHY AND FOUR PATIENTS.

	d ± SD	
Healthy (left leg)	0.9±0.2	
	Non paretic leg	Paretic leg
Patient Nº 1	2.3±0.6	7.8±5.6
Patient Nº 2	3.2±.1.2	6.9±4.5
Patient Nº 3	1±0.9	7.9±6.3
Patient Nº 4	0.7±0.6	1.5±1.2

Table III shows the values of the parameter d for the healthy gait and the gait of four patients.

IV. DISCUSSION AND CONCLUSION

The cyclograms reflect the gait performance reduced to two principal components. The parameter d is a quantitative measure of the cyclograms, which we suggest to be used as the gait measure. The new standard is a simple means for evaluating a therapy [14, 15].

The shapes of cyclograms in patients show a discrepancy in patients' gait compared with healthy persons (Fig. 6). The cyclograms are a catching eye measure to the gait performance. The software we developed allows the clinician to superimpose the cyclogram of a patient over the cyclogram of a healthy gait.

The cyclograms can be used as a simple gait event visualization method. The characteristic points of transition between swing and stance phase of the first two principal components are shown as one point on cyclograms.

Data presented for patients show a significant difference compared with the healthy (Fig. 4, Tables I and II). The high variability between steps is noticeable in patients after stroke compared with the repeatability in persons with no known sensory or motor impairment.

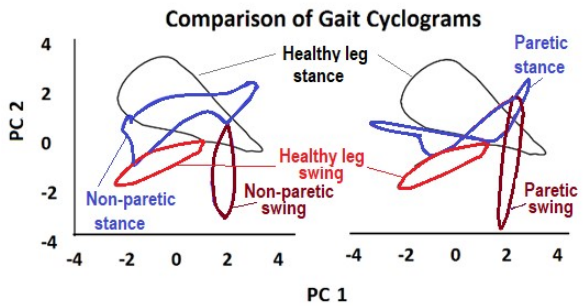

Fig.5. The superimposed cyclogram of a healthy leg over the cyclogram of the non-paretic leg (left panel) and the same cyclogram of a healthy superimposed over the cyclogram of the paretic limb for one gait cycle (right panel).

The orientation of the axis is not essential, since if the sign of a component is changed, the variance contained in that component is not changed. More precisely, these components are given by PCA component scores. Each original variable is a linear combination of the weighted components. The cyclograms are not fully closed curves; some overlap since we observe consecutive steps, but this does not limit the estimation of the parameter d.

The cyclograms shape for the non-paretic leg is more similar to the one presenting healthy gait (Fig. 5). This can be explained by the fact that the neural system still has not developed compensation strategies for this leg. Thus, we can conclude that this image representation is an effective and simple way to follow the therapy's progress.

We suggest that the PCA distinguishes between healthy gait and gait of a person after a stroke.

The Gait Master system also provides data that can be used to study the gait in more detail. More extensive clinical studies for the method's validation started, but the current Covid-19 pandemic slowed down the data collection.

ACKNOWLEDGMENT

The work on this project was partly supported by the Serbian Academy of Sciences and Arts, Belgrade, Project F-137. We thank Prof. Dr. Ljubica Konstantinović and Suzana Dedijer-Dujović, M.D. from the Clinic for rehabilitation. "Dr. Miroslav Zotović," Belgrade for providing gait data.

REFERENCES

[1] http://www.qualisys.com/, accessed on September 4, 2020
[2] https://www.ndigital.com/msci/products/optotrak-certus/, accessed on September 4, 2020
[3] Tao, W., Liu, T., Zheng, R. and Feng, H., 2012. Gait analysis using wearable sensors. Sensors, 12(2), pp.2255-2283.
[4] Chen, S., Lach, J., Lo, B. and Yang, G.Z., 2016. Toward pervasive gait analysis with wearable sensors: A systematic review. IEEE journal of biomedical and health informatics, 20(6), pp.1521-1537.
[5] Muro-De-La-Herran, A., Garcia-Zapirain, B. and Mendez-Zorrilla, A., 2014. Gait analysis methods: An overview of wearable and non-wearable systems, highlighting clinical applications. Sensors, 14(2), pp.3362-3394.
[6] Crea, S., Donati, M., De Rossi, S.M.M., Oddo, C.M. and Vitiello, N., 2014. A wireless flexible sensorized insole for gait analysis. Sensors, 14(1), pp.1073-1093.
[7] Park, S.W., Das, P.S. and Park, J.Y., 2018. Development of wearable and flexible insole type capacitive pressure sensor for continuous gait signal analysis. Organic Electronics, 53, pp.213-220.
[8] www.rehabshop.rs, accessed on July 17, 2020
[9] Cho, S.H., Park, J.M. and Kwon, O.Y., 2004. Gender differences in three dimensional gait analysis data from 98 healthy Korean adults. Clinical biomechanics, 19(2), pp.145-152.
[10] Sandhitsu R. Das, Robert C. Wilson, Maciej T. Lazarewicz, Leif H. Finkel, 2006. Gait Recognition by Two-Stage Principal Component Analysis. Journal of multimedia, vol. 1, no. 5, August 2006.
[11] Milovanović I, Popović DB. Principal component analysis of gait kinematics data in acute and chronic stroke patients. Computational and mathematical methods in medicine. 2012;2012.
[12] Milovanović, I.P., Synergy patterns of stroke subjects while walking: Implications for control of FES assistive devices, Ph.D. thesis, 2013. http://bmit.etf.bg.ac.rs/wp-content/uploads/radovi/doktorati/Doktorat-Ivana-Milovanovic.pdf (in Serbian)
[13] Kaiser, H. F. "An index of factorial simplicity," Psychometrika, vol. 39, no. 1, pp. 31–36, 1974.
[14] Deepak J. and Sneh A., "Cyclogram and cross correlation: A comparative study to quantify gait coordination in mental state", J Biomedical Science and Engineering, pp. 322-326. 2010.
[15] Shanahan, C.J., Boonstra, F., Cofré Lizama, L.E., Strik, M., Moffat, B.A., Khan, F., Kilpatrick, T.J., Van Der Walt, A., Galea, M.P. and Kolbe, S.C., 2018. Technologies for advanced gait and balance assessments in people with multiple sclerosis. Frontiers in neurology, 8

Parameter estimation of a human controller transfer function in man-machine system using the PSO algorithm

Jelena Bulatović, Filip Gašparić, OliveraTomašević, Boris Knežević, Nikola Jorgovanović

***Abstract*—Quantification of human behavior has always been quite interesting and very challenging task for control engineers at the same time. What might seem as an automated action performed by a humanrepresentsin fact an expression of complex underlying body and brain processes. Considering man's ability to memorize, adapt and learn,this task sounds even more difficult. Regardless of the non-linearity in human behavior which results from reasons listed above, some classical procedures have proved to be useful in practical application, and engineers have derived quasi-linear mathematical models which describe a human controller in closed-loop man-machine systems. In this work, a general form of these models was used and parameter estimation was performed. In the observed closed-loop system, a human controller was replaced with a corresponding system which contained estimated parameters. The performance of parameter estimation was measured using mean absolute error, when comparing the output of an actual system, controlled by a human, and a simulated one.**

***Index Terms*—man-machine interface, human-controller, parameter estimation, particle swarm optimization**

I. Introduction

Man-machine interface (MMI) also known as Human-machine interface (HMI) is an integral part of certain devices or systems that allows user inputs to be translated as signals for machines that provide the required output. It has been widely used in electronic, medical, entertainment, military, aerospace and automotive industries etc. Understanding human physical, behavioral and mental features are essential when designing these systems in order to provide realistic and natural interaction with other systems and subsystems. Building describing functions and modeling the performance of human using linear differential equations allows prediction and evaluation of stability of the man-machine system. In research done so far, this has proven to be a very sophisticated problem. Beside the reason mentioned above, describing human behavior is also done in order to completely replace a human operator with an automated system.

The first complete model of a human as an operator in man-machine systems was described in a two-part paper [1][2]. The authors gave a detailed mathematical interpretation of human behavior in the role of a controller in MMI. All experimental techniques used to obtain such a model are discussed in [1]. Similarly, spectral analysis methods were used to obtain frequency domain mathematical models of the operator's behavior while performing manual tracking with tactile displays in [3]. The input-output and input-error cross-power spectral densities were obtained by a method of averaging modified periodograms. Their ratio represents a describing function of the human operator which analytic form was closely approximated using visual fitting. In [4] application of modern control concepts and estimation theory has been made to develop a model of humanoperator in manual tracking. It was applied to the prediction of human response in some simple, single-axis control tasks. The basic assumption was that the human operator behaves as an optimal controller, in accordance with his/her inherent limitations and task definition. The cascade combination of a Kalman filter, a least mean-squared predictor and a set of gains acting on the estimated state formed the resultant model and its unique features were the mathematical representation of the human's limitations and the resulting compensating elements. Later, in [5] the model proposed in [4] was used to analyze a more complex control situation, namely the manual control of the longitudinal position of a hovering aircraft.

In work described in this paper, it is assumed that the form of the subject's transfer function is known and we are not focusing on finding it. The idea is to place a human controller into a closed-loop control system and observe his/her behavior while performing different compensatory tracking tasks, which require different control strategies. Hence, our main goal is to estimate the parameters of the transfer function of a described human regulator in MMI using the PSO algorithm as a key step, which includes simple principle and offers fast convergence and computation.

Motivation for this work is better understanding of human behavior in man-machine systems in order to integrate human into complex technological systems or even completely replace with a certain automated system. As mentioned in [1],

Jelena Bulatović is with the Faculty of Technical Sciences, University of Novi Sad, 6 TrgDositejaObradovića, 21000 Novi Sad, Serbia (e-mail: jelena996@uns.ac.rs).

Filip Gašparić is with the Faculty of Technical Sciences, University of Novi Sad, 6 TrgDositejaObradovića, 21000 Novi Sad, Serbia (e-mail: filip.gasparic@uns.ac.rs).

OliveraTomašević is with the Faculty of Technical Sciences, University ofNovi Sad, 6 TrgDositejaObradovića, 21000 Novi Sad, Serbia (e-mail: olivera.tomasevic@uns.ac.rs).

Boris Knežević is with the Faculty of Technical Sciences, University of Novi Sad, 6 TrgDositejaObradovića, 21000 Novi Sad, Serbia (e-mail: borisknezevic@uns.ac.rs).

Nikola Jorgovanović is with the Faculty of Technical Sciences, University ofNovi Sad, 6 TrgDositejaObradovića, 21000 Novi Sad, Serbia (e-mail: nikolaj@uns.ac.rs).

one of the limiting factors in making a human operator model is that, beside a quasi-linear transfer function, correlated linearly with the forcing function, it also consists of a residual output which represents all output content which cannot be ascribed to a linear operation on the input. In this work, the remnant will be neglected, and we will focus on finding parameters of a quasi-linear model.

II. The Method

An input signal subject is tracking is shown on a computer monitor as well as the output of the controlled system. In each trial during the experiment, the subject moves the joystick up and down in order to minimize the difference between input and output signal which he observes through the visual feedback. Finally, recorded input and output signals are stored and used for parameter estimation of a human controller transfer function. Functional block diagram of a closed-loop control system with respect to visual stimuli describing the experiment setup is given in Fig. 1.

A. Subjects and Experimental Design

The experiment was performed by 5 healthy subjects (3 males and 2 females, 24.8 ± 1.5 years) after signing the consent form which was approved by the local ethical committee. The experiment involved recording the subject's response for 120 seconds when operating a given system.The reference signal, i.e. the forcing function *r(t)*, was multi sine whose frequency components ranged between 0.1 and 0.4 Hz and their amplitudes were randomly chosen in range 0 to 2.5.

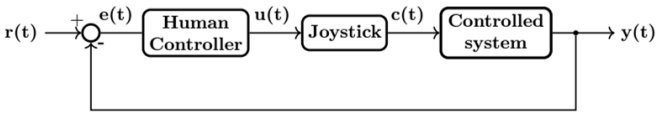

Fig. 1. A block diagram describing closed-loop system where human has the role of a controller; *r(t)* represents the forcing function, i.e. reference signal, *e(t)* is the system error, *u(t)* is the human controller output, *c(t)* is input of a controlled system and *y(t)* represents the output of the controlled system.

B. Experimental protocol

The forcing function was shown to the subject on a computer monitor and his/her task was to follow its motion using the joystick. It can be considered that the transfer function of the joystick used in this experiment is equal to one, i.e. $u(t) = c(t)$, since this joystick does not contain elastic and inertial elements that can affect its behavior in the observed frequency range. The signal at the joystick's output *c(t)* represents an input signal for the controlled system which was modeled by one of four transfer functions of considered systems. The *y(t)* is the output of the controlled system which was also shown to the subject on the computer monitor.All the time during the experiment, the subject wasmonitoring the forcing function and the output signal on the same graph. The subject himself estimated the error as a difference between two observed signals and simultaneously corrected his/her control in order to minimize the error. This type of control is called compensatory tracking, because the reference signal *r(t)* appears randomly and the only information displayed to the operator is an output of a controlled system *y(t)* and it represents a visual feedback to the operator. An example of a subject performing the tracking task is shown in Fig. 2.

Transfer functions of systems controlled by the subject in this experiment and general form of a transfer function of a

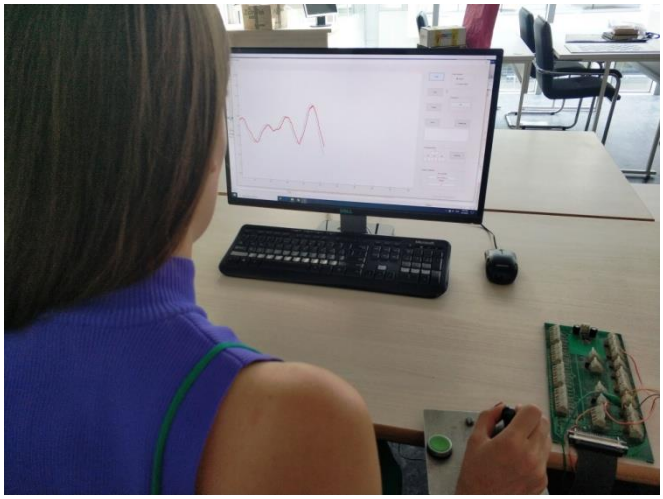

Fig. 2. A subject performing the tracking task using the joystick.

human controller when controlling the corresponding system are given in Table I. The experimental data considered for these systems were taken directly from the efforts of investigators in [1] [2] and [7].

In order to perform the experiment, a personal computer (PC), a Hall-effect joystick and an acquisition card – National Instruments PCI-6024 were used. Data acquisition, as well as a simple graphical user interface that allows the user to run the experiment, were implemented within the MATLAB software package (ver. R2018a, Math Works, USA). The application gives the user the ability to enter data about the subject, set the duration of the experiment and parameters of a system operator controls as well as monitor tracking performance, data acquisition and calibration.

Reference signal *r(t)*, control signal *c(t)* and output signal *y(t)* are stored in the *.mat* file with data about the subject and parameters of a transfer function of acontrolled system. All recorded signals were sampled with a period of $T = 0.01s$.

III. Parameter Estimation

After the signals were recorded, parameters of a transfer function of the human controller were estimated. As mentioned above, the PSO algorithm was used for parameter estimation.

Swarm-based methods such as the PSO algorithm are well-known as powerful tools for dealing with the global optimization problems encountered in engineering [6]. PSO algorithm starts by creating initial population in a form of set of particles often called "swarm", and searches the space which contains potential solutions. Each particle is characterized with its position in previous and current iteration. In addition, each particle is able to remember its best achieved position through iterations, as well as swarm is able

to remember best position achieved by any particle in that particular swarm. Because of the rules that define the process of their motion, particles will eventually swarm around the best possible solution. The generalized PSO algorithm used for the purposes of this work is presented in [6].

As an optimization criterion, mean absolute error was defined and the goal was to find parameters so that the value of this function is minimal. This means that the output of a simulated system needs to be as similar as possible to an actual output of a system obtained during the experiment. In a simulated system, the human controller is replaced with a system whose parameters are estimated. The number of particlesand the maximal number of iterations used in this work varied depending on the number of estimated parameters and it was set to be 10 and 100 times greater, respectively. For example, when the subject controlled system 1, the number of parameters that needed to be estimated was 3. Thus, the number of used particles was 30 and the maximal number of iterations was 300. It has been determined experimentally that this number of iterations is quite sufficient for the algorithm to converge towards the best possible solution for this particular optimization problem. Therefore, the stop criterion was the maximum number of optimization iterations. Out of 10 runs of parameter estimation algorithm, for each subject in every experiment, the run with the best available values of parameters for the given criterion was chosen.

TABLE I
TRANSFER FUNCTIONS OF SYSTEMS USED IN EXPERIMENT AND GENERAL FORM OF A HUMAN CONTROLLER TRANSFER FUNCTION WHEN CONTROLLING THE CORRESPONDING SYSTEM

System	Transfer function of a controlled system	Transfer function of a human operator
1	1	$K\frac{1}{\left(\frac{s}{a}+1\right)}e^{-s\tau}$
2	$\frac{1}{s+1}$	$K\frac{\left(\frac{s}{b}+1\right)}{\left(\frac{s}{a}+1\right)}e^{-s\tau}$
3	$\frac{4}{s}$	$K\frac{\left(\frac{s}{b}+1\right)}{\left(\frac{s}{a}+1\right)}e^{-s\tau}$
4	$\frac{2}{s(0.25s+1)}$	$K\left(\frac{s}{b}+1\right)e^{-s\tau}$

IV. RESULTS

The optimal parametersof a human controllertransfer function, when controlling systems 1 to 4that were obtained using the PSO algorithm are given in Tables II to V, together with the values of the corresponding criterion function (CFV) and mean absolute error (MAE). Mean absolute error is used to represent quality of human performance while performingcompensatory tracking task, that is, the average difference between the reference signal and the control signal during the experiment.Fig. 3 and Fig. 4 show performance of subject 3 during tracking an input signal while controlling system 1 and system 4, respectively.

TABLE II
PARAMETERS OF A TRANSFER FUNCTION OF A HUMAN CONTROLLER WHEN CONTROLLING SYSTEM I

Subject	MAE	K	a	τ	CFV
1	0.256	4.798	1.016	0.193	0.133
2	0.228	5.711	1.098	0.240	0.168
3	0.286	2.861	1.686	0.268	0.141
4	0.247	6.416	0.439	0.495	0.268
5	0.178	7.800	0.957	0.208	0.127

TABLE III
PARAMETERS OF A TRANSFER FUNCTION OF A HUMAN CONTROLLER WHEN CONTROLLING SYSTEM II

Subject	MAE	K	a	b	τ	CFV
1	0.307	4.806	1.966	2.418	0.333	0.148
2	0.355	1.117	1.162	0.354	0.377	0.199
3	0.395	1.230	2.454	0.849	0.409	0.148
4	0.368	3.852	7.985	26.757	0.252	0.236
5	0.280	5.945	1.593	2.615	0.316	0.165

TABLE IV
PARAMETERS OF A TRANSFER FUNCTION OF A HUMAN CONTROLLER WHEN CONTROLLING SYSTEM III

Subject	MAE	K	a	b	τ	CFV
1	0.382	0.830	3.312	2.340	0.331	0.248
2	0.468	1.006	7.513	22.169	0.248	0.317
3	0.418	1.091	2.495	12.415	0.008	0.270
4	0.417	1.290	3.620	4.779	0.301	0.332
5	0.566	0.901	2.955	2.594	0.366	0.457

TABLE V
PARAMETERS OF A TRANSFER FUNCTION OF A HUMAN CONTROLLER WHEN CONTROLLING SYSTEM IV

Subject	MAE	K	b	τ	CFV
1	0.540	1.837	0.324	0.186	0.382
2	0.695	1.241	0.341	0.078	0.481
3	0.409	1.730	0.173	0.205	0.274
4	0.401	1.637	0.158	0.206	0.272
5	0.621	1.216	0.082	0.002	0.403

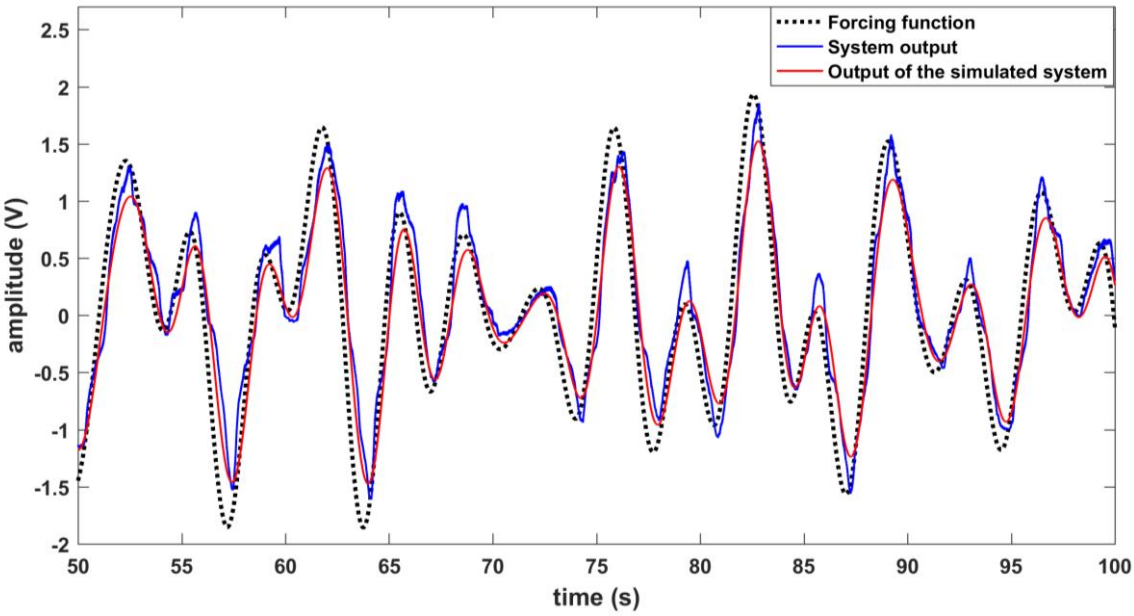

Fig. 3. 50 seconds of the experiment is shown: the input signal (black dotted line) subject 3 is tracking using the joystick and the output signal (solid blue line) which represents the output of the controlled system 1. After these signals were stored and parameter estimation was done, the human controller was replaced with the system with estimated parameters. The output of the system obtained in described way is shown with solid red line.

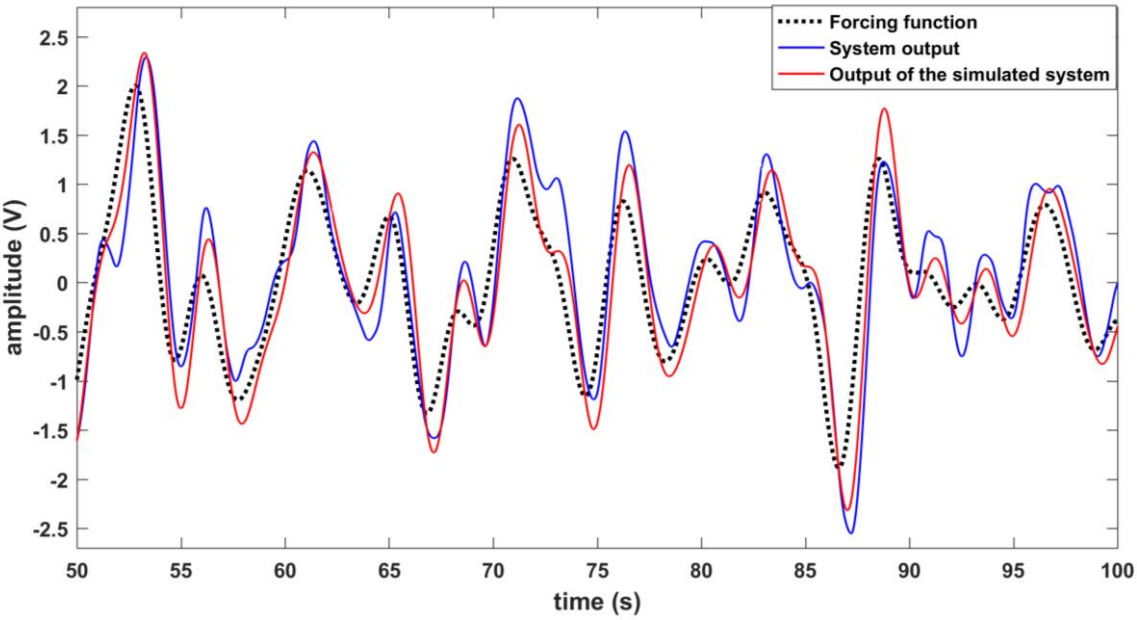

Fig. 4. 50 seconds of the experiment is shown: the input signal (black dotted line) subject 3 is tracking using the joystick and the output signal (solid blue line) which represents the output of the controlled system 4.After these signals were stored and parameter estimation was done, the human controller was replaced with the system with estimated parameters. The output of the system obtained in described way is shown with solid red line.

These graphs show the reference signal that the subject is tracking using the joystick, the output signal which represents the output of the controlled system and the output from the simulated system. As mentioned above, in the simulated system the human controller is replaced with a system with estimated parameters. Mean absolute error that subject 3 makes while tracking is 0.286 for the system 1 and 0.409 for the system 4. Clearly, system 4 is more challenging for subject to control due to its more complex transfer function (see Table I). Values of criterion function when estimating parameters are 0.141 and 0.274, for systems 1 and 4, respectively. Observing the results obtained from other

subjects, it can be noticed that quality of parameter estimation depends on quality of subject's control.

V. Discussion

Although a human behaves as a non-linear system, a human operator shows some regular behavior from the controlled system viewpoint [8]. Also, a human has the ability to adapt to certain situations and remember patterns, but its behavior could be considered linear when no detectable pattern is present [9]. Although the forcing function consists of components at the same frequencies throughout the whole experiment, their amplitudes are numbers that range from 0 to 2.5, which are randomly generated at the start of each trial. This way, the subject cannot memorize the exact shape of the reference signal. The only thing a subject can learn is how to control the particular system.

It is natural to assume that it is not possible to obtain the same parameters for different subjects. Thus, it is expected that the subject's response will vary depending on several factors, such as the dynamics between the manipulated variable and the display, general condition and previous experience of the subject at the time of the experiment (which affects the subject's precision in control, reaction delays, etc.)[1]. Observing the human controller transfer function, it can be concluded how a subject behaves when operating a particular system.

The simplest way of control is modeled with gain K which gives an output signal proportional to the input signal. The next most obvious is reaction time of a human, modeled with$e^{-s\tau}$. When controlling the first threesystems, in transfer function of a human there is a lag, expressed by parameter$a$, showing that the human controller is able to follow slower changes of reference signal, and filters out faster ones, i.e. human behaves as a low pass filter. Lastly, the human's ability to predict a change in input and undertake corresponding control action is represented by derivative time, b.

Transfer functions of a human controller when controllingsystem 1 and system 2 obtained in this work can be considered appropriate for certain applications that do not require high precision, as the value of the criterion function varies from 5% to 10% of the maximum amplitude of the input signal. For systems 3 and 4, the calculated error was as twice as large and varied between 10% and 20% of the maximumamplitude of the input signal. This could be explained by the fact that these systems were more challenging for subjects to control, and thus evoked unexpected human behavior that could not be precisely described using only quasi-linear models. As stated in [9], experiments done by highly trained subjects will give the best results when estimating parameters of a human controller transfer function. Although the subjects who did the experiment for the purposes of this paper had certain time to get familiar with the way of controlling the given systems, they could not be classified as highly trained. This fact could be useful for further work in order to improve the performance of parameter estimation. The more reasonable solution would be to divide an experiment over several days, provide subjects with more training time and make longer pauses between trials in order to prevent mental and physical fatigue occurring in subjects.

VI. Conclusion

The work described in this paper gives an insight into a pilot study conducted with five subjects in order to test a new method for quantification of a human who has the role of the operator in a closed-loop control system. General forms of human controller transfer functions when controlling corresponding system were taken directly from existing literature and their parameters were estimated using the PSO algorithm. The results show that using this method it is possible to find parameters of a quasi-linear transfer function which is able to successfully describe a human behavior when controlling the given system. In further work, in addition to improvements mentioned above, dozens of subject should be considered for this experiment inorder to find a transfer function of an average human controller.

Because the experiment responded to the representation of an operator with a linear mathematical model in a closed-loop control system and examined the quality of visual feedback control, further steps in this research may include the use of another type of feedback, such as electro-stimulation or vibrotactile stimulation and to compare the quality of control when using different feedback, as well as to monitor whether the control can be improved by training. A functional description of human control could be crucial in various applications in biomedical engineering such as closed-loop upper limp prosthesis control, or for example, wheelchair control.

VII. Acknowledgment

This research was supported by the grants III41007 from the Ministry of Education, Science and Technological development of Serbia.

References

[1] McRuer, D.T. and Krendel, E.S., "The human operator as a servo system element part I". *Journal of the Franklin Institute, 267,* no.5, pp.381-403, May, 1959.

[2] McRuer, Duane T., and Ezra S. Krendel. "The human operator as a servo system element part II." *Journal of the Franklin Institute, 267,* no 6, pp.511-536, June, 1959.

[3] Schmid, H.P. and Bekey, G.A., 1978. "Tactile information processing by human operators in control systems0." *IEEE Transactions on Systems, Man, and Cybernetics, 8,* no.12, pp.860-866, Dec, 1978.

[4] Kleinman, D. L., Baron, S. and Levison, W.H., "An optimal control model of human response part I: Theory and validation." *Automatica, 6,* no. 3, pp.357-369, May, 1970.

[5] Kleinman, D. L., Baron, S. and Levison, W.H., "An optimal control model of human response part II: prediction of human performance in a complex task." *Automatica, 6,* no. 3, pp.371-383, May, 1970.

[6] Kanović, Ž.,Rapaić, M.R. and Jeličić, Z.D., "Generalized particle swarm optimization algorithm-Theoretical and empirical analysis with application in fault detection." *Applied Mathematics and Computation, 217, no.* 24, pp.10175-10186, Aug., 2011.

[7] McRuer, D. "Human dynamics in man-machine systems."*Automatica* 16, no.3, pp.237-253, May, 1980.

[8] Abe, M., *Vehicle handling dynamics: theory and application*., 2nd ed. Butterworth-Heinemann, 2015.

[9] Jagacinski, R. J., and Flach, J.M., *Control theory for humans: Quantitative approaches to modeling performance*., 1st ed. Boca Raton, Florida, CRC Press, 2003.

Validation of the new wearable instrument for the pendulum test based on inertial sensors

Marjan Miletić, Vladimir Atanasoski, Jelena Kršić, Aleksandar Lazović, and Lana Popović-Maneski

***Abstract*— The important indicator of the impairment and the course of the recovery in humans with the central nervous system is the assessment of spasticity. The pendulum test was accepted as the quantification method of knee muscles' spasticity. We present a new, inexpensive, easy to use wireless pendulum test device for estimation of spasticity of knee muscles (quadriceps and hamstrings). The new system uses inertial, and electromyography (EMG) sensors positioned at the upper and lower leg segments. The measurement device was applied for the pendulum test on a population of thirteen healthy volunteers. We estimated seven parameters from the pendulum test, which form a single measure of spasticity in patients, termed the pendulum test (PT) score. Results show a small deviation for all parameters between subjects, and mean values of PT score are below 1, which is in the range for healthy persons from the literature. Hence, the mean values of these seven parameters can be used as a reference for the PT score estimation in patients.**

Index Terms—spasticity assessment, wireless pendulum test device, PT score.

I. Introduction

The quantification of the level of impairment is essential for clinicians to select the most appropriate treatment for patients after spinal cord injury (SCI), stroke, multiple sclerosis (MS) or cerebral palsy (CP). Spasticity is one of the main impairments resulting in an automatic increase of the tonus of affected muscles and increased sensitivity to the stretch in SCI patients [1]. More precisely, spasticity is defined as "motor disorder characterized by a velocity-dependent increase in tonic stretch reflexes ("muscle tone") with exaggerated tendon jerk, resulting from hyperexcitability of the stretch reflex, as one of the components of the upper motor neuron syndrome [2]. The conventional method for assessing spasticity by a clinician is using the modified Ashworth scale [3]. The pendulum test was introduced to meet the need for a more accurate quantification method for assessing spasticity and reducing the subjective component of the evaluation of spasticity[4] [5]. The type and intensity of knee muscles spasticity are determined from a set of parameters calculated from the knee joint angle vs. time data curve acquired from the pendulum test [1, 4].

Marjan Miletić is with the Department of Atomics Physics, "VINČA" Institute of Nuclear Sciences - National Institute of the Republic of Serbia, University of Belgrade, Belgrade, Serbia (e-mail: marjanmil@vin.bg.ac.rs).

Vladimir Atanasoski is with the University of Belgrade, Studentski trg 1, 11000 Belgrade (e-mail: vladimir.soski@gmail.com).

Jelena Kršić is with the Department of Atomics Physics, "VINČA" Institute of Nuclear Sciences - National Institute of the Republic of Serbia, University of Belgrade, Belgrade, Serbia (e-mail: jkrsic@vin.bg.ac.rs).

Aleksandar Lazović is a Ph.D. student at University of Belgrade, Studentski trg 1, 11000 Belgrade, Serbia (email: aca.lazovic@gmail.com).

Lana Popović-Maneski is with the Institute of Technical Sciences of SASA,, Knez Mihailova 35/IV, 11000 Belgrade, Serbia (e-mail: lanapm13@gmail.com).

During the pendulum test, while the subject is sitting on the side of bed or similar, the examiner releases the subject's lower leg from a position where the knee joint is fully extended and observes deviations of the knee angle from the dumped oscillation pattern. Standard methods to measure knee joint angle include Hall-effect joint angle encoder of the knee joint [1], potentiometer measuring the knee joint [4], smartphone camera-based system with passive markers at the lateral side of the knee joint [6] or angle camera-based systems in motion laboratories with passive/active markers [7, 8].

We presented a new pendulum test device for the estimation of knee joint muscles spasticity. The instrumentation comprises inertial sensors (gyroscope and accelerometer) mounted on the anterior side of thigh and shank (one 3D gyroscope and one 3D accelerometer per segment) and EMG amplifier that measures muscle activities of two muscles *via* surface electrodes. All signals are wirelessly sent to the host computer with the user-friendly acquisition program. The acquisition program allows the examiner to follow EMG signals from quadriceps and hamstring muscles and angular velocities and acceleration of the thigh and shank vs. time during the pendulum test on the computer screen. The data recorded are used to estimate the Pendulum test (PT) score, as defined by Popović-Maneski et al. [1].

In this paper, we show the data recorded in a group of 13 healthy volunteers, and we show the estimated mean values necessary for the calculation of the PT score in patients.

II. The Method

A. Subjects

The study includes 13 healthy volunteers with demographic data given in Table 1.

TABLE I
BASIC DATA FOR HEALTHY SUBJECTS PARTICIPATING IN THE STUDY

N^o	Sex	Age	Height [cm]	Mass [kg]
1H	F	33	178	65
2H	F	61	166	80
3H	F	35	178	90
4H	F	36	162	55
5H	F	52	162	50
6H	M	30	175	87
7H	M	34	170	82
8H	M	68	178	92
9H	M	35	182	76
10H	M	68	179	115
11H	F	35	162	55
12H	M	24	177	81
13H	F	25	168	60

The inclusion criteria for healthy volunteers were the following: no known sensory-motor impairment, controlled blood pressure and pulse, and able to follow the protocol of the pendulum test.

B. Instrumentation

The pendulum test device (Fig. 1) consists of two separate housings interconnected with a spiral wire. The housings are fixed with stretchable velcro straps on the anterior side of the thigh and shank. The distances of the thigh and the shank housing from the knee joint are about 15cm and 20cm. The distance between housings does not influence the measurements, but it is essential to position them perpendicularly to the sagittal plane. Thigh housing has leads connected with the electrodes for the recordings of two EMG signals with reusable surface electrodes (four leads for the measurements and one lead for the grounding). We used, for the test purposes, one EMG channel for e recording the muscle activity of the quadriceps. EMG signal recording was accomplished with pre-gelled Ag/AgCl electrodes (NM 3351 OFI, Top Trace, CERACARTA S.p.A., Forli, Italy) placed over the bulk of the quadriceps muscle with the inter-electrode distance of 2cm. The ground electrode was placed over the bony part of the knee joint. We do not show in this paper the EMG recordings.

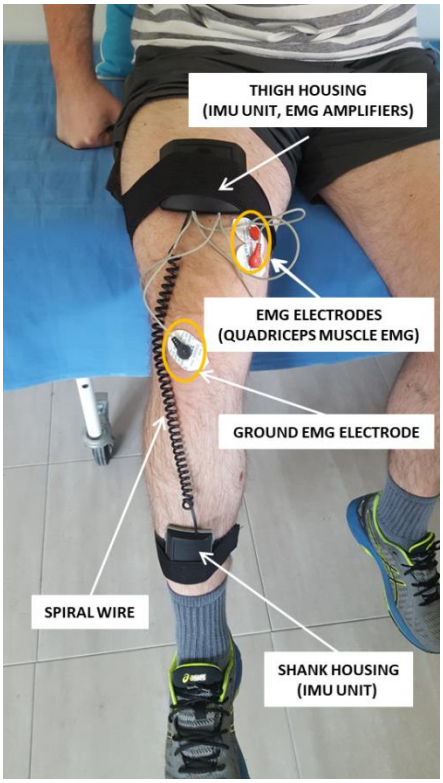

Fig. 1. The wireless instrument for the pendulum test. The thigh and shank housings have inertial measurement units: 3D accelerometers and 3D gyroscopes. Thigh housing also has the EMG amplifiers for bipolar measuring of the muscle activity.

Both thigh and shank housings have an inertial measurement unit (IMU), consisting of one gyroscope and one accelerometer sensor. IMU unit is based on the MPU6050 unit (InvenSense, San Jose, California, USA). This particular IMU unit has a 16bit AD converter, 100Hz sample rate, +/- 500deg/s gyroscope sensor range, and +/-4g accelerometer sensor range. EMG amplifiers in thigh housing are based on one ADS1294 ECG chip (Texas Instruments, Dallas, USA). ECG unit has a 24bit AD converter, 500Hz sampling rate, DC coupling, and inputs for 2 EMG leads.

The pendulum test device has a battery power supply in thigh housing. There is also an “on/off” button for Bluetooth wireless connection with laptop computer and pendulum test acquisition program. All measurement signals from inertial sensors and EMG amplifiers are time-synchronized and subsequently digitized. Signals from inertial sensors are resampled to 500 samples per second.

A subject was sitting on a stable wheel-fixed clinical bed with the back support with a firm pillow (hip joints flexed at approximately 135°). The knee joint was positioned about 5 cm in front of the edge of the bad to ensure that the lower leg swings freely.

C. Measurements

The test was performed on thirteen healthy subjects. Subjects were asked to relax the leg muscles and try not to activate them during the trial. The examiner released the subject’s lower leg from a position where the knee joint was fully extended and allowed shank to oscillate like the physical pendulum about the knee joint until the foot stopped the swinging (Fig. 2). The angular velocity and the angular acceleration of shank and thigh and EMG signal from the quadriceps m. were simultaneously recorded during the pendulum movements. The pendulum test was repeated with a pause of 15 seconds between the trials until three successful pendulum test measurements were obtained. The successful trial is described as a pendulum test movement with no EMG or minimal EMG activity. EMG recordings from the quadriceps were used for online inspection of the leg muscle activity.

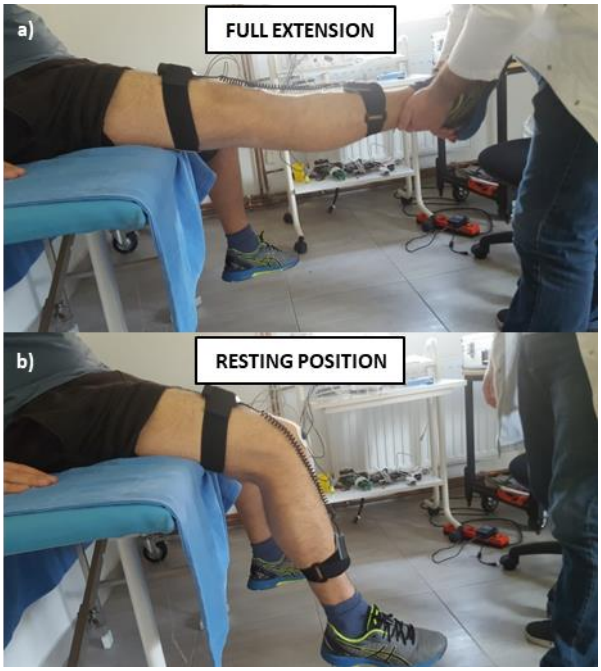

Fig. 2. The fully extended leg reached by the examiner (a) and resting position of the leg (b)

D. Data processing

The EMG signals from quadriceps were high-pass filtered

above 30 Hz, normalized to the maximal value for each swing, and filtered with a notch filter at 50 Hz with a 3rd order Butterworth filter. The sagittal angular velocity signals from the gyroscopes and sagittal angular acceleration signals from accelerometers were filtered with the moving average filter that included 50 samples. The mean value of the last second of the signal (resting position) was subtracted from all angular velocity and angular acceleration signals due to different resting angles for each subject. Corrected sagittal angular velocity of the shank was calculated as the difference of angular velocity of the shank, measured by shank gyroscope, and angular velocity of the thigh, measured by thigh gyroscope, to compensate the thigh movement during pendulum test. The sagittal angle signal was calculated as the first integral of the corrected angular velocity signal. We developed a program for data acquisition in a C# environment and automatic data processing in Matlab.

The parameters from the test for the estimation of spasticity, as defined in [1], are: R_{2n} – the normalized relaxation index, N – the number of swings, ϕ_{max} – the first maximum of the angle signal after releasing the leg, and ω_{max} and ω_{min} - the maximum and minimum angular velocity of the shank, f- the frequency of dump oscillations of pendulum test and $|P_+ - P_-|/P_{total}$ [%] - the absolute difference between the positive and negative areas between the angle signal and neutral line starting from the first minimum and divided with the total area. The normalized relaxation index was calculated from the knee joint angle signal (angle between shank and thigh). The index was calculated as $R_{2n} = A_1/1.6A_0$ where A_0 is the knee joint angle between the full extension (starting position) and the neutral knee joint angle (resting position), and A_1 is the difference between the starting angle and the maximum flexion (the first minimum in the angle signal) as defined by Bajd et al. [4]. N was estimated by counting the number of maxima of the knee joint angle more significant than 1° during the recording session.

The above-listed parameters are used to calculate the PT score with the following equation:

$$PT_i = \left(\left|\frac{(R_{2n_i}-\hat{R}_{2n_H})}{7*\hat{R}_{2n_H}}\right| + \left|\frac{(N_i-\hat{N}_H)}{7*\hat{N}_H}\right| + \left|\frac{(\varphi_i-\hat{\varphi}_H)}{7*\hat{\varphi}_H}\right| + \left|\frac{(\omega_{max_i}-\hat{\omega}_{max_H})}{7*\hat{\omega}_{max_H}}\right| + \left|\frac{(\omega_{min_i}-\hat{\omega}_{min_H})}{7*\hat{\omega}_{min_H}}\right| + \left|\frac{(f_i-\hat{f}_H)}{7*\hat{f}_H}\right| + \left|\frac{\left(\left|\frac{P^+-P^-}{P_{total}}\right|_i - \left|\frac{\widehat{P^+-P^-}}{P_{total}}\right|_H\right)}{7*100}\right|\right) * 10 \qquad (1)$$

Where i denotes a subject, H is used for the values of healthy subjects and ^ represents the mean value for all subjects. Each member of the equation is divided with 7 (total number of parameters) for normalizing the PT score.

In this study, we estimated the values in Equ. 1 denoted with the nominator H (acronym for healthy).

III. Results

A typical example of the signals recorded in one out of thirteen volunteers is in Fig. 3 and represents subject 6H. The normalized EMG recordings from the quadriceps muscle, and estimated knee joint angle and the angular velocity are plotted together for six consecutive repetitions of the test in Fig. 3a. Three trials were selected where the EMG was minimal for the calculation of the pendulum test parameters. The time beginnings of the selected three trials are marked with vertical green lines in Fig. 3a. The knee joint angle, angular velocities, and EMG signal for the selected three trials are in Fig. 3b. Fig. 3c. presents the knee joint angles for the selected 3 trials. There are also marked angles A_0 and A1 (red lines), used for calculation of normalized relaxation index R_{2n}, maximal angle of swings (green dots), which total number represent a number of swings N.

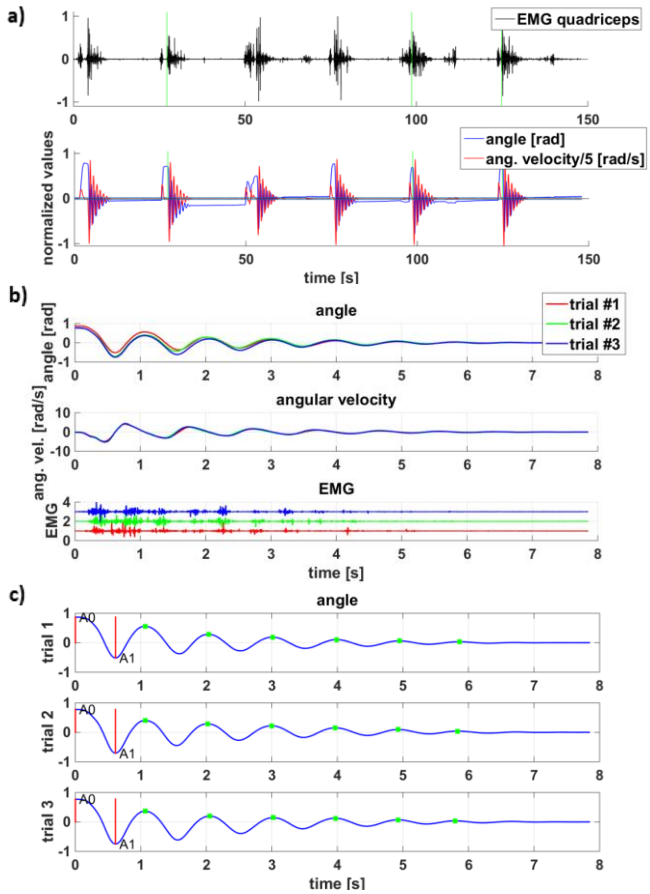

Fig. 3. The recordings of processed signals for subject 6H: EMG signal of quadriceps (normalized), the knee joint angle, and angular velocity of the lower leg for one healthy subject (a). The processed knee joint angle, angular velocity, and normalized EMG activities of quadriceps for the selected 3 trials (minimal EMG activity), started at the vertical green line (b). The knee joint angles for the selected 3 trials with marked positions of the local maxima (green dots), A0 and A1 angles (red lines)(c).

PT values for the selected 3 trails for all subjects are shown in Fig.4. To calculate the PT score, we used the mean values of the parameters with the H index in Eq.1 from all subjects (three trials each). High variability of the scores comes directly from the subjects' inability to relax the muscles completely. The example of the signal in Fig.3. supports this claim because it is visible that the stronger EMG activity in trial 3 changed the regular oscillatory pattern of the angle signal. In further analysis, we used only the minimal PT score value for each subject. In Fig.5, we show the mean values and standard deviations of the seven parameters for the whole set using the trial with minimum PT score in each of 13 subjects. The value for the normalized relaxation index R_{2n} (1.06±0.06), number of swings N (7.08±1.04), the first maximum of the angle signal

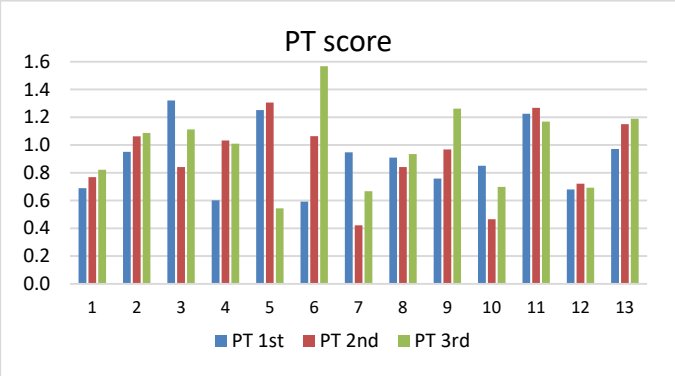

Fig. 4. PT scores for the three selected trials in 13 healthy subjects.

ϕ_{max} (0.62±0.09 rad), the frequency of oscillations f (1±0.05 Hz), the absolute difference between the positive and negative areas between the angle signal and neutral line $|P^{+} - P^{-}|/P_{total}$ (7±5 %), have values in range for healthy individuals according to the literature [1][4].

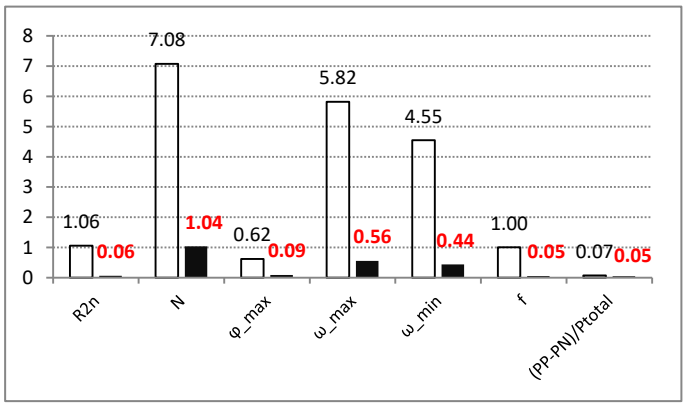

Fig. 5. Mean absolute values of seven parameters (empty bars) and standard deviations (black bars) from 13 healthy subjects.

The standard deviation for parameters R_{2n}, N, and f is low, for parameter ϕ_{max} relative small and for parameter $|P^{+} - P^{-}|/P_{total}$ relatively high; however, the absolute values of this parameter are close to zero. The value for maximum and minimum angular velocity, ω_{max} (5.82±0.56 rad/s) and ω_{min} (-4.55±0.44 rad/s) are much lower than values for healthy range given by [4], but they are in the healthy range given by [1], which could be explained by the fact that we used calculation method for these parameters that are exact and more strict than in [4]. Standard deviations for ω_{max} and ω_{min} are relatively low. Values for pendulum test score PT (0.73±0.22) are below 1, and they are in healthy individual range according to [1].

Fig. 6. shows the values of calculated PT score with the contribution of every parameter included in its calculation according to (1), for each of thirteen healthy subjects. Contribution of parameter $|P^{+} - P^{-}|/P_{total}$, which is relatively unreliable because of high standard deviation, in the calculation of PT score, is low for all subjects.

IV. Conclusion

Previous studies with PT score included a small number of

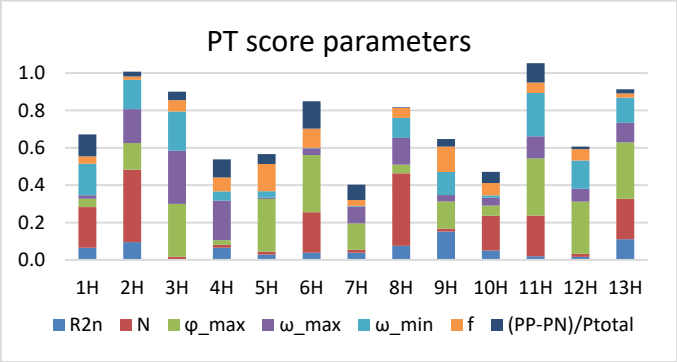

Fig. 6. The value of the PT score (equal to the total height of the stacked bar) with the contribution of seven parameters from equation (1) used in the calculation for each subject.

healthy subjects; hence, the reference "healthy" values previously used for calculation of PT score in patients were unreliable. We calculated PT score components from 13 healthy subjects of different age and sex to determine a set reference values that can be used in future clinical studies in persons with disabilities. Six out of seven parameters of the PT score determined for the tested group had the standard deviation below 15%. The standard deviation for the seventh parameter $(|P^{+} - P^{-}|)/P_{total)}$ is in range of 75%. However, the magnitude of this parameter in healthy is close to zero, so the contribution to the PT score is negligible. The magnitude of this parameter is large for the patients and it shows if the extension or flexion components of spasticity is dominant [1]. The mean values determined in this study will be used in future clinical studies with SCI, stroke, MS, and CP patients to assess their knee spasticity.

Acknowledgment

This study was financially supported by the Ministry of Education, Science and Technological Development of the Republic of Serbia, Agreement with the Institute of Technical Sciences SASA, Grant No. 451-03-68/2020-14/200175 and the Grant F-137 from SASA.

References

[1] L. Popović-Maneski, A. Aleksić, A. Metani, V. Bergeron, R. Čobeljić and D. B. Popović, "Assessment of Spasticity by a Pendulum Test in SCI Patients Who Exercise FES Cycling or Receive Only Conventional Therapy." IEEE Trans Neural Syst Rehabil Eng,, vol. 26, no. 1, pp. 181-187, Jan., 2018.

[2] L. Popović-Maneski, A. Aleksić, R. Čobeljić, T. Bajd, D. B. Popović. "A new method and instrumentation for analyzing spasticity." IETI Trans on Ergonomics and Safety, vol. 1, no. 1, pp. 12-27, Jan., 2017.

[3] R. W. Bohannon, M. B. Smith, "Interrater reliability of a modified Ashworth scale of muscle spasticity "Phys ther, vol. 67, no. 2, pp. 206-207, Feb, 1987.

[4] T. Bajd, L.Vodovnik. "Pendulum testing of spasticity." Journal of Biomedical Engineering., vol. 6, no 1. , pp. 9-16, Jan. ,1984

[5] R. Wartenberg, "Pendulousness of the legs as a diagnostic test." Neurology, vol. 1, pp, 18-24, 1951.

[6] A. Aleksić, S. Graovac and D. B. Popović, "The pendulum test for assessing spasticity based on smart phone movie and passive markers" IcETPAH 2017, 4rd International Conference on Electrical, Electronic and Computing Engineering, Kladovo, Serbia, June, 2017.

[7] Qualisys motion capture systems. URL: http://www.qualisys.se/, accessed on June 25, 2020.

[8] Optotrak.URL:https://www.ndigital.com/msci/products/optotrakcertus/, accessed on June 25, 2020.

Lacunarity Analysis of Microvascular Morphology in Human Retina

Ivana Konatar, Nataša Popović, Tomo Popović, *Senior Member*, *IEEE*,
Miroslav Radunović, Batrić Vukčević

***Abstract*—Fractal analysis provides means for the quantitative assessment of geometric patterns in one, two, and three dimensions. It is aimed at analysis of graphical shapes that belong to a class of fractal objects that are characterized by the self-similarity over different scales. Various structures in nature are fractals and fractal analysis techniques are widely used for analysis of biomedical images. One such example of application is analyzing blood vessel structure in the human retina that can be extracted from digital images captured by fundus camera. The most commonly used fractal analysis is estimation of fractal dimension using various box-counting methods for mono- and multi-fractals. Although two fractal images can have the same fractal dimension they can have very different appearance and structure. One can appear as a structure that fills most of the available space, while the other can have a lot of empty areas. These differences can be quantified by lacunarity parameter, which has greater value in images with less space-filling properties. This paper focuses on the estimation of the lacunarity parameter implemented in the Python programming language, which is aimed at lacunarity analysis of microvaculae morphology in human retina. The implementation is validated by comparison with the results obtained by ImageJ, a commonly used software for analysis of biomedical images. The value of the lacunarity analysis is demonstrated on a set of actual images of human retina associated with different medical conditions.**

***Index Terms*—Box-counting method; fractal analysis; lacunarity; image analysis; Python; retinal microvasculature.**

I. Introduction

The fractal and lacunarity analysis have been around for some time and their usage is recognized in different areas of science [1,2]. Fractal analysis techniques are becoming widely used in medicine for analysis of biomedical signals and images [3-5]. One such example of application is analyzing blood vessel structure in human retina that can be extracted from digital images captured by fundus camera [6,7].

The microvascular system of the retina is an integral part of the microcirculation of the human body that can be studied directly, *in vivo,* in a simple and non-invasive way by using digital photography. This approach gives us information not only about the health of the eye, but also represents one of the standard diagnostic methods used to detect complications of systemic diseases such as diabetes mellitus and hypertension [8]. Vascular networks have fractal structure, so this fact is often used to differentiate healthy retinal microvasculature from the one with pathological changes [9]. Healthy vascular network is characterized by higher complexity and higher fractal dimension, while various systemic and eye-specific pathological processes in most cases cause vascular pruning and lower vascular complexity. Decreased fractal dimension of the microvascular network is a nonspecific marker of pathological process in the organism, because by itself, it cannot show what pathological process caused it. We previously showed that specificity of fractal analysis results can be increased by adding to the analysis of microvascular geometry the lacunarity dimension that measures gappiness of the image [10]. This approach uses the fact that two fractal images can have the same fractal dimension although they have very different appearance resulting from different space filling properties of each image [11,12]. Therefore, when analyzing geometric patterns in biomedical images, in addition to fractal dimension, it may be useful to estimate the lacunarity of the structure and include it in the analysis [13,14].

This paper shows a scripting tool for quantitative analysis of microvascular network in human retina based on estimation of the lacunarity analysis, that was developed by using Python programming language. The implementation is validated by comparison with the results obtained by ImageJ, a commonly used software for analysis of biomedical images [15]. The value of the lacunarity analysis is demonstrated on a set of actual publicly available images of human retina associated with different medical conditions.

II. Materials and Methods

A. Images of Retina

For this research, we used a publicly accessible High - Resolution Fundus (HRF) image database containing 45 raw color images of retina. Images were captured with a Canon CR-digital fundus camera with a 45° field of view and resolution of 3504 × 2336 pixels [16,17]. The database contains 3 groups of images: 15 images of healthy retina, 15 images of retina showing signs of diabetic retinopathy, and 15 images with signs of glaucoma. Each image comes with a

Ivana Konatar is with Faculty of Applied Sciences, University of Donja Gorica, Oktoih 1, 81000 Podgorica, Montenegro (e-mail: ivana.konatar@ udg.edu.me).

Nataša Popović is with Faculty of Medicine, University of Montenegro, Kruševac bb, 81000 Podgorica, Montenegro (e-mail: npopovic@ucg.ac.me).

Tomo Popović is with Faculty for Information Systems and Technologies, University of Donja Gorica, Oktoih 1, 81000 Podgorica, Montenegro (e-mail: tomo.popovic@ udg.edu.me).

Miroslav Radunović is with Faculty of Medicine, University of Montenegro, Kruševac bb, 81000 Podgorica, Montenegro (e-mail: miro@t-com.me).

Batrić Vukčević is with Faculty of Medicine, University of Montenegro, Kruševac bb, 81000 Podgorica, Montenegro (e-mail: batricvukcevic@gmail.com).

corresponding gold standard manual vessel segmentation binary image. In the present study, our focus was on these binary images representing retinal microvasculature.

B. Lacunarity Estimation

Similarly to the estimation of box counting fractal dimension, we determine E that represents a set of all scales, i.e. all square sizes by which we will cover the given image [14,18]. The maximum value for $\varepsilon \in E$ may be min (n, m), where n and m are the length and width of the image, and the smallest value for ε is limited by the image resolution. Namely, the smallest value for ε must be greater than or equal to 1px. We can start from the smallest scale, squares with side length of ε, and increase it according to the algorithm in order to form the set E. For images of retina this is illustrated in Fig. 1. As opposed to fractal dimension, where each square is checked whether the square covers fractal objects or not, when determining the lacunarity we count how many pixels in the square actually belong to the object.

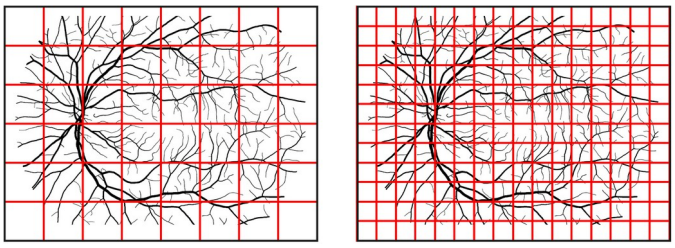

Fig. 1. Covering the fractal objects with different box scales

The lacunarty at each scale ε is estimated using the following formula:

$$\Lambda(\varepsilon)=\left(\frac{\sigma}{\mu}\right)^2 \tag{1}$$

where σ is the standard deviation, and μ is the mean of the number of pixels counted for each square with sides of length ε. The following statistical formulas are used:

$$\mu=\frac{1}{n}\sum_{i=1}^{n} x_i \tag{2}$$

$$\sigma=\sqrt{\frac{1}{n}\sum_{i=1}^{n}(x_i-\mu)^2} \tag{3}$$

where x_i is the total number of pixels in each square and n is the total number of squares at the given scale ε.

As a final step, for a given geometric structure, the lacunarity Λ for a given image is estimated as an average value of all $\Lambda(\varepsilon)$ previously calculated for all scales ε [13].

C. Three Variants of the Estimation Algorithm

We implemented three variants of the method for lacunarity estimation algorithm based on the approach how the squares at different scales ε were placed over the geometric object we are analyzing, as illustrated in Fig. 2. The first variant of the algorithm uses standard non-overlapping placement of squares over the object until the whole image is not covered. This process is repeated at each scale ε and the total number of squares needed to cover the image depends on the size of the image and selected scale ε.

The second approach uses gliding overlapping boxes to cover the image at each scale ε [19]. Here we have a much larger number of total squares needed to cover the image and the number depends on how much do we move/glide each square between the iterations.

Finally, we implemented an approach to lacunarity estimation with random placement of squares over the image at each scale as it can be done for calculations of fractal dimension [20]. The total number of squares at each scale is arbitrary for each step, but it should be at least equal to the total number of squares with sides ε needed to cover the whole image.

As for the settings, the following values were used for for the scales ε: {3, 5, 7, …,19}, both in our script and in the ImageJ program. As for the gliding box approach, when "gliding" the box, each next box was moved 50% to the right, and 50% down when moving to the next row. Finally, for the random placement method, we used the number of boxes for each scale ε to be the same as the the total number of squares of size ε needed to cover the whole image.

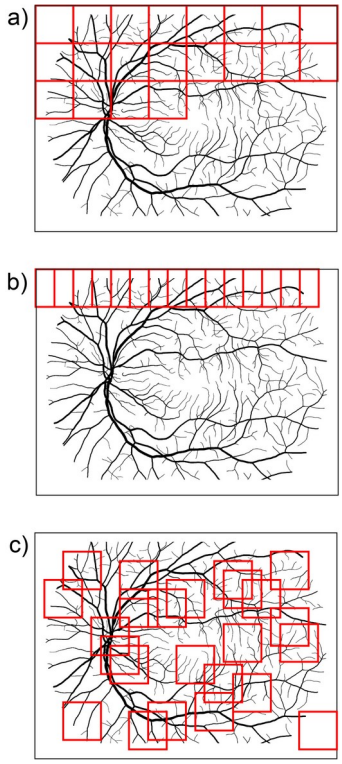

Fig. 2. Three variants of the algorithm: a) Standard non-overlapping boxes, b) Gliding box approach, c) Random box placement

D. Programming and Statistical Analysis Tools

The algorithm for lacunarity analysis is developed using the Python programming language and the Jupyter Notebook scientific computing software [21]. The Jupyter Notebook provides a web-based collaborative environment for experimenting with the code and the intermediate results can

be accessed using a standard web browser. Statistical analysis of the results was performed and visualized using R programming language.

E. Validation Using ImageJ Software

Validation of the lacunarity analysis results obtained using our Python script is done by the comparison with the results obtained by ImageJ software and FracLac plugin [15,22]. ImageJ is a public domain Java program that is commonly used for image analysis in biomedicine. All 45 binary images from the HRF image database that represent blood vessels microvascular network were processed in order to compare lacunarity parameter estimates calculated by ImageJ and all three variants of the presented new software tool were implemented in Python.

III. Results and Discussion

First, we performed the sanity check using arbitrary images of known fractals. We compared the numbers obtained with new Python script and ImageJ and observed matching results in up to two decimal places (data not shown). Next, we used the 45 images coming from the open access HRF image database containing retina images from three groups of subjects: 15 images from patients with diabetic retinopathy (DR), 15 images from patients with glaucoma (G), and 15 images of healthy retina (H). We observed a very good alignment of the results coming from ImageJ and all three approaches implemented in our script as depicted in Fig. 3. The best alignment with the ImageJ is achieved with the gliding box approach, but the computing time was slightly longer than the time that was needed for the standard non-overlapping box approach. As for the method with random placement of boxes, it yielded very good results, even with the number of boxes in each step that is equal to the total number of squares of size ε needed to cover the whole image, let us call it M. This method becomes even more accurate when we use a number of boxes that is much larger than the number M, i.e. 5x, 10x, 50xM, but in those cases the calculation would take much more time. Therefore, the approach with random placement of boxes can be very accurate, but the computing time for this method would be the longest out of the three.

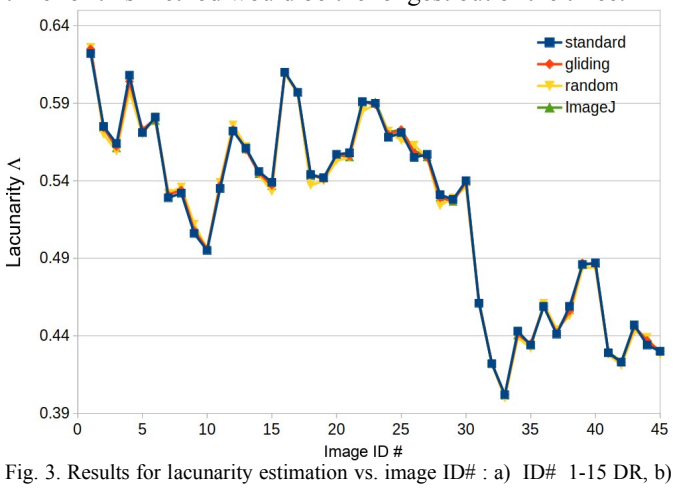

Fig. 3. Results for lacunarity estimation vs. image ID# : a) ID# 1-15 DR, b) ID# 16-30 G; c) ID# 31-45 H

The main evaluation criteria for our research was to perform a comparison of our implementation in Python to ImageJ for the type of experiments we plan to do in the near future. For that purpose we performed statistical analysis in order to compare the three groups of images coming from the HRF image database. As shown in Table 1, there is a very good match of the mean values and standard deviations for the results coming from all three variants of the Python method and ImageJ program. The mean lacunarity distributions for each group of images are also depicted by using box plots in the Fig. 4. It can be seen that the data coming from all four methods, all three variants and ImageJ, display almost identical distributions.

TABLE I
Comparison with ImageJ Software: HRF Image Database

Method vs. Diagnosis	Healthy (H)	Glaucoma (G)	Diabetic Retinopathy (DR)
Standard	0.4438±0.0234	0.5626±0.0249	0.5557±0.0348
Gliding	0.4438±0.0232	0.5624±0.0254	0.5559±0.0343
Random	0.4424±0.0231	0.5606±0.0256	0.5556±0.0334
Image J	0.4439±0.0232	0.5627±0.0255	0.5559±0.0339

Note: showing values mean ± SD

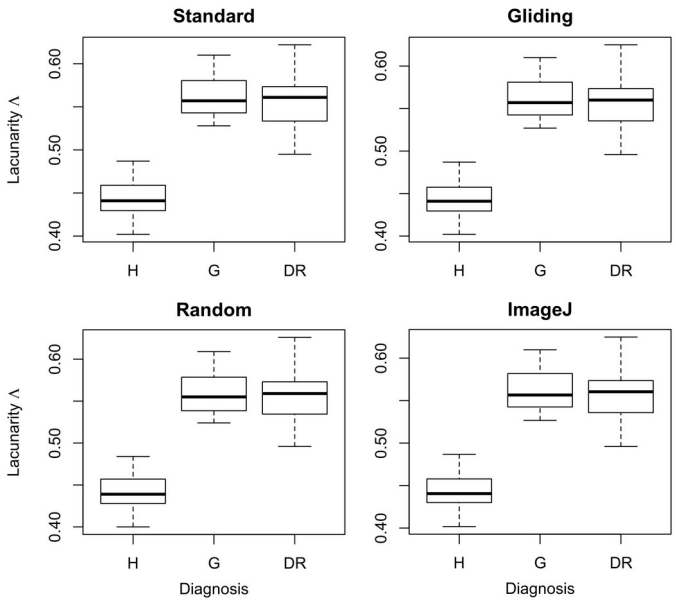

Fig. 4 Statistical visualization of the mean lacunarity distribution for each group of retinal images (H- healthy, G-glaucoma, DR- diabetic retinopathy) Distributions of data points were obtained with our script for three variants for lacunarity calculation in Python vs. results obtained with ImageJ program

In addition, a one-way ANOVA with Tukey post-hoc test was used to analyze if the mean lacunarity dimension is different among the different diagnoses. More importantly, in each case, the p value obtained with the statistical analysis led to the same conclusion regardless which method for the estimation of lacunarity parameter was used (Fig. 5). These results validated the data obtained with three variants of lacunarity estimation from our script versus the results obtained by ImageJ program and FracLac plugin.

This Python script is developed as a part of the project with a main goal to study the use of new methods for stratification of patients with Alzheimer's dementia according to the risk for progression of this disease [23]. One of such methods is use of portable digital fundus camera to evaluate microvascular geometry of the retina in elderly people. Despite the fact that the resolution of images captured with a portable non-mydriatic digital fundus camera is relatively small, its use has many advantages. This type of camera is affordable, and also quick and easy to use because does not require prior dilatation of the pupil. It could be used for screening in primary care clinics in a large number of patients. It could be also used in the field outside the outpatient clinic for patients for whom specialized health care is difficult to access. Digital photographs can be subsequently easily transmitted to a diagnostic center by an ophthalmologist for expert analysis [24,25].

The main advantage of the use of this new script is possibility to perform fully automated scripting and control over our *in-silico* experiments that will be performed on segmented digital retinal fundus images of patients with Alzheimers dementia and the subjects with normal cognitive function. An additional control group of subjects will be made of the patients with colon cancer because it has been shown that in people with some cancers, the incidence of Alzheimers dementia is very low, and vice versa – people with Alzheimers dementia rarely have decreased incidence of cancer [26].

The next steps in development of this analysis tool will include integration with automated fractal dimension and multifractal parameters estimation in order to create a single Python library.

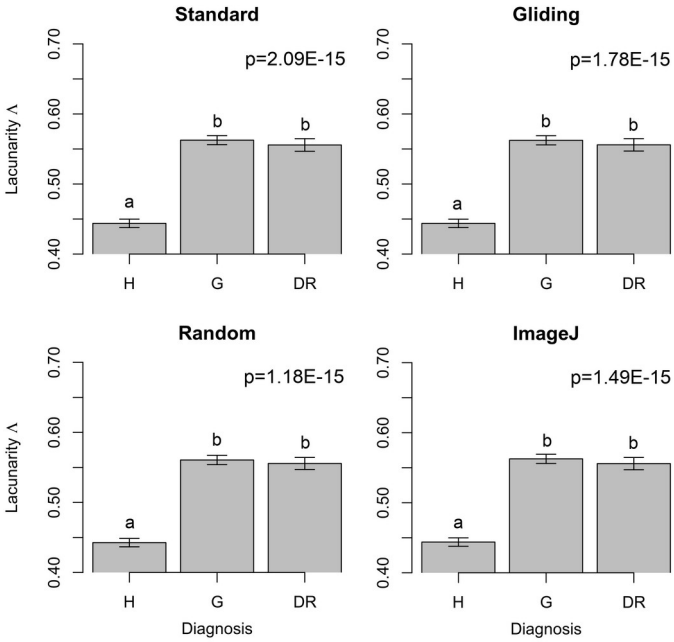

Fig. 5. One-way ANOVA test using lacunarity from different methods

IV. Conclusion

This research focuses on the implementation of a Python library to enable performing automated lacunarity analysis of biomedical images. The paper describes three variants of the implementation aimed for the use when analyzing fractal objects commonly found in biomedical images. The implementation was validated using an open access set of images of human retina. The results obtained by three variants of the method implemented in Python were compared with the results of ImageJ program. It should be pointed out that the method using non-overlapping box placement was the fastest, but not as accurate as the method using gliding box approach. The method with random placement of boxes needs a larger number of boxes than the non-overlapping method in order to achieve desired accuracy and it was the slowest one out of the three. However, the method with random placement of boxes could be very useful if we wanted to estimate the lacunarity of a part of an image that is cut out using an irregular shape. Furthermore, the results for all three methods were statistically analyzed and in each case the statistical analysis led to the same conclusion, regardless which method for the estimation of lacunarity parameter was used. This new tool allows for easy automation of experiments with biomedical images.

Further steps in the research will include improvements of various argument options and additional settings in order to enable advanced and fully automated fractal analysis of fundus images of human retina. Additional image sets will be used including fundus images obtained by a hand-held fundus camera that can be operated by family physicians. Usage of such cameras, combined with the use of fractal analysis and quantification, could potentially allow for development of non-invasive disease detection in early stage.

Acknowledgment

Research supported in part by the Ministry of Science of Montenegro, scientific-research project DEMONSTRATE, Grant Agreement No. 01-781/2.

References

[1] K. Falconer, "Fractal Geometry: Mathematical Foundations and Applications", John Wiley & Sons, New York, 1990.

[2] M. F. Barnsley, "Fractals Everywhere", Dover Publications, Inc., Mineola, New York, 2012.

[3] R. W. Glenny, H. T. Robertson, S. Yamashiro, J. B. Bassingthwaighte, "Applications of fractal analysis to physiology", Journal of applied physiology (1985), 70(6), pp 2351-2361, 1991.

[4] I. Reljin, B. Reljin, "Fractal geometry and multifractals in analyzing and processing medical data and images", Archive of oncology, 10(4), pp 283-293, 2002.

[5] A. L. Karperien, H. F. Jelinek, "Fractal, multifractal, and lacunarity analysis of microglia in tissue engineering", Frontiers in Bioengineering and Biotechnology, Vol. 3, Article 51, pp 1-4, 2015.

[6] C. C. Chen, J. S. Daponte, M. D. Fox, "Fractal feature analysis and classification in medical imaging," IEEE Transactions on Medical Imaging, IEEE, 8(2), pp 133-142, 1989.

[7] C. Cheung et al., "Quantitative and qualitative retinal microvascular characteristics and blood pressure," Journal of Hypertension, 29(7), pp 1380–1391, 2011.

[8] N. Popovic, S. Vujosevic, and T. Popovic, "Regional Patterns in Retinal Microvascular Network Geometry in Health and Disease," Scientific Reports, 9(2019):16340, Nature Research, 2019.
[9] T. Stosic, B. Stosic, "Multifractal analysis of human retinal vessels", IEEE Transactions on Medical Imaging", 25(8), pp 1101-11-07, 2006.
[10] N. Popovic, M. Radunovic, J. Badnjar, T. Popovic, "Fractal dimension and lacunarity analysis of retinal microvascular morphology in hypertension and diabetes," Microvasc. Res. 118 (2018), Elsevier, pp 36–43, 2018.
[11] B. B. Mandelbrot, "A Fractal's Lacunarity, and how it can be Tuned and Measured", in "Fractals in Biology and Medicine", Mathematics and Biosciences in Interaction. Birkhäuser, Basel, Springer, pp 8-21, 1994.
[12] R. E. Plotnick, R. H. Gardner, W. W. Hargrove, K. Prestegaard, M. Perimutter, "Lacunarity analysis: A general technique for the analysis of spatial patterns", Physical Review E, 53(5), pp 5461-6468, 1996.
[13] T. G. Smith, Jr., G. D. Lange, W. B. Marks, "Fractal methods and results in cellular morphology / dimensions, lacunarity and multufractals", Journal of Neuroscience Methods, 69(1996), pp 123-136, 1996.
[14] S. Gilmore, R. Hofmann-Wellenhof, J. Muir, H. P. Soyer, "Lacunarity Analysis: A Promising Method for the Automated Assessment of Melanocytic Naevi and Melanoma", PLOS ONE, 4(10), e7449, 2009.
[15] C. Schneider, W. Rasband, K. Eliceiri, "NIH image to ImageJ: 25 years of image analysis," Nat. Methods 9 (2012), pp 671–675, 2012.
[16] Budai, A., Bock, R., Maier, A., Hornegger, J. & Michelson, G., "Robust vessel segmentation in fundus images". International Journal of Biomedical Imaging 2013, 1–11 (2013)
[17] High-Resolution Fundus (HRF) Image Database. Www5.cs.fau.de at, https://www5.cs.fau.de/research/data/fundus-images (2019)
[18] C. R. Tolle, T. R. McJunkin, and D. J. Gorsich, "An efficient implementation of the gliding box lacunarity algorithm," Physica D237, pp. 306-315, 2008.
[19] A. Roy, E. Perfect, "Lacunarity analyses of multifractal and natural grayscale pattern", Fractals, 22(3):1440003, 2014.
[20] I. Konatar, T. Popovic, N. Popovic, "Box-Counting Method in Python for Fractal Analysis of Biomedical Images", 2020 24th International Conference on Information Technology (IT), Zabljak, Montenegro, pp 1-4, 2020.
[21] Project Jupyter. Accessed July 2020. [Online]. Available: http://jupyter.org
[22] A. Karperien, "FracLac for ImageJ-FracLac Advanced User's Manual," National Institutes of Health. Accessed July 2020. [Online]. Available: http://rsb.info.nih.gov/ij/plugins/fraclac/fraclac-manual.pdf
[23] The DEMONSTRATE project: Risk stratification for progression of cancer and Alzheimer's disease. Accessed July 2020. [Online]. Available: https://demonstrate.ucg.ac.me
[24] S. Vujosevic, E. Midena, "Diabetic Retinopathy in Italy: Epidemiology Data and Telemedicine Screening Programs", Journal of Diabetes Research, 2016(3627465), pp 1-6, 2016.
[25] J. Lopez-Bastida, F. Cabrera-Lopez, P. Serrano-Aguilar, "Sensitivity and specificity of digital retinal imaging for screening diabetic retinopathy". *Diabetic Medicine*, 24(4), pp 403-407, 2007.
[26] J. Driver, "Inverse association between cancer and neurodegenerative disease: review of the epidemiologic and biological evidence," Biogerontology, 15(6), pp 547-557, 2014.

Segmentation and Classification of Leucocyte Images for Detection of Acute Lymphoblastic Leukemia

Ivana Pešić

***Abstract*—Acute lymphoblastic leukemia (ALL) is the most common type of leukemia among children. It is characterized by excessive occurrence of immature lymphocytes – lymphoblasts, especially in bone marrow and lymphoid organs. Diagnosing ALL based on blood samples is routinely done by hematologists, often using cytogenetic analysis or immunophenotyping. However, these visual examinations are often slow and limited by subjective interpretation; therefore standardized inexpensive automated systems for detecting lymphoblasts in blood images are needed. Systems for ALL detection are still in the development stage; improving techniques of lymphocyte segmentation from blood images and classification techniques is a challenge. The aim of this paper is to perform a segmentation of lymphocytes on images from the publicly available ALL_IDB2 database and to compare different classification algorithms for ALL detection. Morphological, color and texture feature extraction from segmented lymphocyte images was performed as well as Principal Component Analysis (PCA) for dimensionality reduction. Classification into two groups (healthy lymphocytes and lymphoblasts) was performed using three different algorithms: k-Nearest Neighbours (kNN), Support Vector Machine (SVM) and feedforward neural network (NN).**

***Index Terms*—acute lymphoblastic leukemia; lymphocyte segmentation; feature extraction; lymphoblast classification**

I. Introduction

Leukemia is a blood cancer which is characterized by uncontrolled proliferation of white blood cells in bone marrow. Leukemias can be divided into acute and chronic; according to the type of white blood cells that are affected by malignant transformation, they are divided into myeloblastic, lymphoblastic and monoblastic. Acute lymphoblastic leukemia (ALL) [1] is a disease caused by the proliferation of immature lymphoid cells (lymphoblasts), mostly in bone marrow and lymphoid organs. According to the French-American-British (FAB) classification of ALL [2], ALL is divided into three groups: L1, L2 and L3. L1 is the most common form of ALL among children, L2 is much more common among adults, while L3 is very rare. This disease mostly occurs in children (about 80%), and in adults it occurs usually around the age of 50. It can be fatal if not treated adequately, hence, early diagnosis is of the utmost importance.

Ivana Pešić is with the School of Electrical Engineering, University of Belgrade, 73 Bulevar kralja Aleksandra, 11020 Belgrade, Serbia (e-mail: ivanapesic207@ gmail.com).

Routinely, diagnosing of ALL is done manually by a medical expert - hematologist. Disadvantages of such an analysis are slowness, as well as the fact that the results are under subjective influence of the doctor. For these reasons, there was a need to create a fully automated computer-aided system that would perform the detection of lymphoblastic cells from blood images. The advantages of such systems would be speed, affordability and procedure standardization.

The most important step in automated ALL systems is the high accuracy recognition of lymphoblasts in microscopic images of blood. Lymphocytes are cells with regular circular shape and with a compact cytoplasm. In contrast, lymphoblasts have more irregular shape and may contain small cavities in the cytoplasm. Each system for detecting lymphoblasts using blood images should contain 3 main parts: segmentation of lymphocytes from blood images, feature extraction from segmented lymphocytes (from whole lymphocytes or their nuclei) and classification into two groups: lymphoblastic and healthy cells.

Various segmentation and classification methods can be found in literature. There are several attempts to design semi-automated system for detecting ALL. The image database ALL_IDB [3], which consists of two sets of images: ALL_IDB1 (blood images with more than one blood cell) and ALL_IDB2 (cropped areas of individual normal and blast cells that belong to ALL_IDB1) , was created to develop and test such systems by Department of Information Technology - *Università degli Studi di Milano*. F. Scotti et al. [4] proposed a method for lymphocyte segmentation and classification based on the feedforward neural network (NN) with the accuracy of 98.67% on the ALL_IDB1 image database. M. Madhukar et al. [5] used c-mean clustering for leukocyte segmentation from the ALL_IDB1 image database, morphological and texture features were extracted and the Support Vector Machine (SVM) classificatory reached the accuracy of 93.5%. S. Mishra et al. [6] performed image segmentation using watersheds and classification using Random Forest algorithm with the classification accuracy of 99% on the ALL_IDB1. Putz et al. [7] performed a transformation to CMYK color space, determined a threshold value for segmentation using Zack's algorithm, morphological, texture and color features were extracted, and classification was performed using Support Vector Machine with the accuracy of 93% on the ALL_IDB1. V. Singhal and P. Singh [8] used the transformation of images into HSV space, threshold segmentation and classification by Support Vector Machine and the classification accuracy was 89.72% on the ALL_IDB2. Abdeldaim, Ahmed and Talaat et al. [9]

performed a transformation into CMYK color space, segmentation was done using Zack's algorithm, texture, color, and shape features were extracted, and the highest accuracy of 96.01% on the ALL_IDB2 was obtained using k-Nearest Neighbours (kNN). Siew Chin Neoh et al. [10] performed segmentation using clustering, and classification accuracy of 96.67% was obtained using 10-fold cross-validation and Support Vector Machine method on the ALL_IDB2.

In this paper, following steps were performed: segmentation of leukocyte images from the ALL_IDB2 database (because it contains only one blood cell per image) using Otsu's threshold, extraction of 3 types of features (morphological, color and texture), dimensionality reduction using Principal Component Analysis (PCA) and classification using 3 different algorithms: k-Nearest Neighbours, Support Vector Machine and feedforward neural network. The aim of this paper was to segment both whole leukocytes and their nuclei from a publicly available blood image database, to extract different features from segmented cells/nuclei, and finally, to test different classification methods, in order to conclude which method has the greatest potential for further development, as well as which features are the most distinctive.

II. The Method

A. Dataset

Segmentation and classification methods were tested on ALL_IDB2. All images in this database were taken with an optical laboratory microscope coupled with a Canon Power Shot G5 camera. ALL lymphoblast classification was provided by expert oncologists. ALL_IDB2 dataset consists of 260 cropped regions of one healthy leucocyte or lymhoblast; resolution of each image is 257 x 257 pixels. There are 130 lymphoblast images (class 1) and 130 images of normal cells (class 0). Fig. 1 shows some example images from this database.

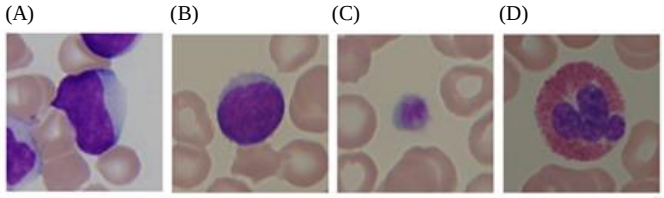

Fig. 1. Images from ALL_IDB2 database: (A) lymphoblast, (B) healthy lymphocyte, (C) platelet, (D) eosinophil

B. Segmentation

Segmentation method consisted of three steps: preprocessing, threshold-based segmentaton and postprocessing. It is necessary to segment the whole cell (both nucleus and cytoplasm), as well as nucleus only, because parameters of both elements are important in order to properly distinguish lymphoblast cell from healthy one. At the end, only leucocyte images should be selected for further classification.

1. Preprocessing

In the preprocessing step, two images based on the original one were prepared for further processing [13]. For the first one, the original image was converted to a grayscale image and global contrast correction method was applied using following formula:

$$I_p(x,y) = 255 \cdot \frac{(I_o(x,y) - min)}{(max - min)}, \qquad (1)$$

where (x, y) are pixel coordinates, I_p is in output grayscale image, I_o is input grayscale image, min and max are the minimum and maximum gray values of an input image. This image will be used to segment only nucleus from lymphocyte. The second image for further processing is an image of H channel from HSV color space: this image will be used to segment the whole cell, because clear difference can be seen between leucocytes, red blood cells and background.

2. Treshold-based segmentation

In histograms of grayscale image with contrast stretching and H channel image (Fig. 2), three sections can be observed. The part with low levels of gray belongs to the background, the middle part belongs to the remains of cytoplasm in the grayscale image and to the remains of red blood cells in the H channel image and the part with the highest brightness levels belongs to the nucleus in grayscale image and the whole cell in the H channel image. Therefore, segmenting the part of the image with the highest brightness levels should be done. Both in grayscale and H channel image, Otsu's threshold method was used twice in a row in order to achieve this [11]. In the first use of Otsu's threshold method background is eliminated; the second one was performed to remove the remains of the cytoplasm/red blood cells.

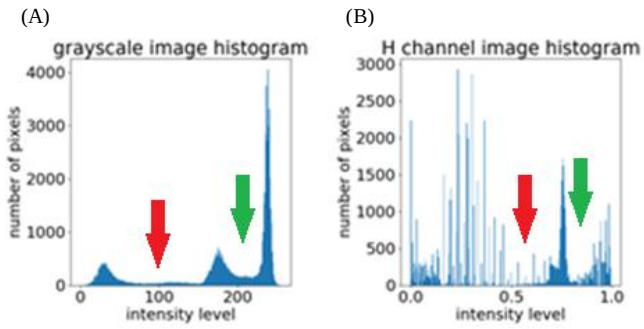

Fig. 2. (A) Grayscale image histogram, (B) H channel image histogram; red arrow - first Otsu's threshold, green arrow – second Otsu's threshold

3. Postprocessing

After the segmentation step, there will still be remains of the noise in the segmented images. The binarization of these two segmented images was done to perform morphological opening [11], using a 5 x 5 kernel of circular shape (due to the circular shape of the lymphocytes). Extraction of the largest connected region was performed and then median filtering with a 15 x 15 kernel and, lastly, morphological closing to fill the holes and remove dots.

4. Leucocyte selection

Since the ALL_IDB2 dataset contains images of all types of blood cells, only leucocyte images should be selected to be used in further classification. The following three parameters

[7] were used to determine whether a cell would participate in the classification:

1) Roundness

$$roundness = \frac{4\pi \cdot P}{O^2}, \quad (2)$$

where P is the area and O is the perimeter of the object. If roundness is 1, then the shape is circle. This parameter is relatively insensitive to irregular edges of the object, and experimentally the threshold was set to 0.58.

2) Solidity

$$solidity = \frac{P}{P_c}, \quad (3)$$

where P is the area and P_c is the area of the convex shell of the object. The closer solidity is to 1, the more regular the edge of the object is and it does not have many holes. The threshold is set to 0.899.

3) Area

The area of the segmented object should be at least one-twelfth of the whole image area, in order to avoid selection of platelets which are circular, but very small.

If the value of at least one of these parameters was less than the specified threshold, the image would not participate in further classification. Out of all 260 leucocyte images, 130 lymphoblasts and 76 healthy cells were selected.

C. Feature extraction

After segmenting whole lymphocyte cells and their nucleuses, the next step was extracting features from these segmented areas. Three types of features were extracted: 26 morphological, 10 color and 24 texture features [7].

1. Morphological features: area, perimeter, major axis, minor axis, convex area, convex perimeter, orientation, roundness, solidity, elongation, eccentricity, rectangularity and convexity are calculated for both nucleus and whole segmented cell.
2. Color features: mean value, standard deviation, skewness, kurtosis and entropy are calculated for both nucles and whole cell.
3. Texture features: contrast, dissimilarity, homogeneity, ASM (Angular Second Moment - Energy), root value of ASM and correlation are calculated from GLCM - *Gray Level Co-occurence Matrix* [11]. These features were calculated only for the segmented whole cell for 4 different angles: – 0°, 45°, 90° and 135°.

D. Principal Component Analysis

Dimensionality reduction is performed to eliminate redundant features. One of the most widely used method for this is the Principal Component Analysis method [12] and it was perfomed in this paper. The process for reducing the feature vector X from n to m dimensions is:

1. Estimate the covariance matrix from vector X.
2. Determine the eigenvectors and eigenvalues of the covariance matrix and sort eigenvalues in descending order.
3. Form a transformation matrix A that contains m eigenvectors that correspond to the largest eigenvalues.
4. Calculate transformation

$$Y = A^T X, \quad (4)$$

where Y is the new feature vector with m dimensions.

E. Classification

Class 0 represents the class of healthy cells, while class 1 represents lymphoblast cells and data is imbalanced (there are 63.1% lymphoblast images and 36.9% healthy cell images); 80% of the images from both classes were used for the traning set and 20% for the test set. The following three algorithms were used and compared:

1. K-Nearest Neighbours (kNN), where 5 neighbours were taken.
2. Support Vector Machine (SVM) with Gaussian kernel
3. Feedforward neural network with hyperarameter optimization – the goal was to find hyperparameters that maximize a certain criterion, in this case F1 score. Hyperparameters for optimization were: number of nodes in hidden layers, activation functions and class weights, where 20% of the training set was used as a set for validation.

III. Results and Discussion

A. Segmentation results

Fig. 3 shows a characteristic example of the original image of a single lymphoblast from ALL_IDB2. Fig. 4 shows the H-channel of the original image used for segmenting the whole cell, the results after segmentation based on the first Otsu threshold, the binary image after segmentation based on the second Otsu threshold and finally, the segmented whole cell after morphological processing. Fig. 5 shows the grayscale image of the original image, grayscale image with corrected contrast, the results of its two segmentations and the final segmented nucleus. Two additional examples of segmentation results from this dataset can be seen in Fig. 6.

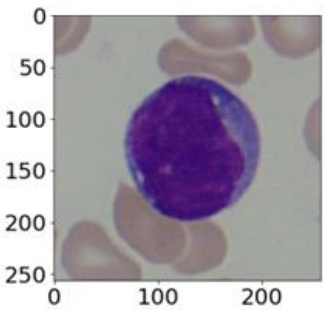

Fig. 3. Original image of one cell from ALL_IDB2

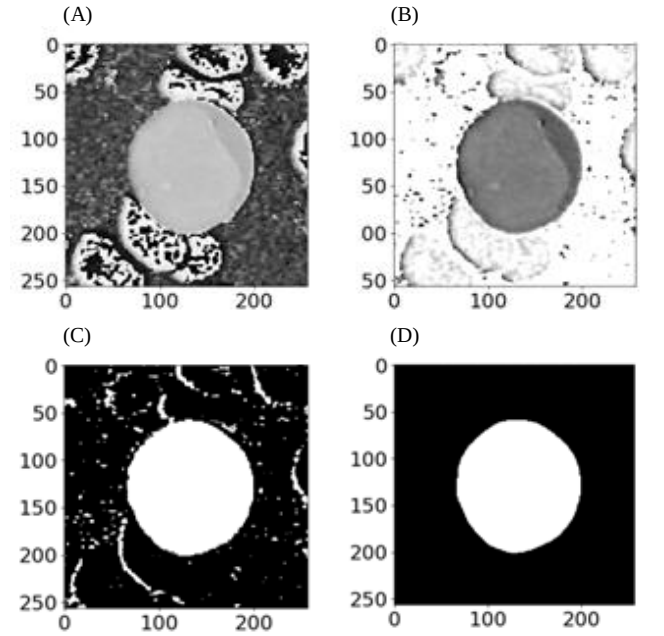

Fig. 4. Steps for segmenting the whole cell: (A) H-channel of the original image, (B) result after first Otsu thresholding, (C) result after second Otsu thresholding (D) segmented whole cell

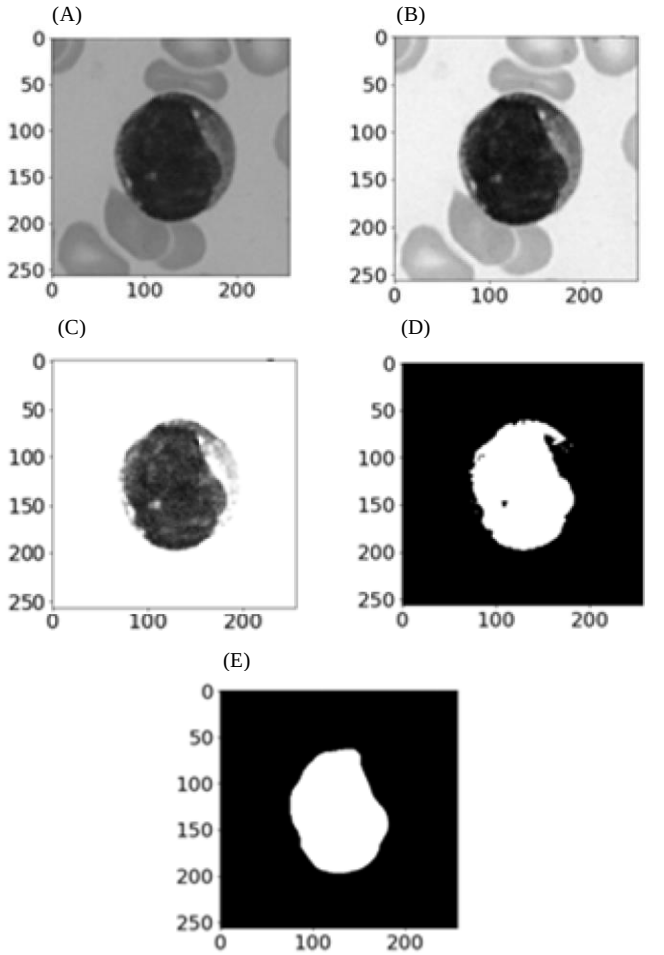

Fig. 5. Steps for segmenting the nucleus: (A) grayscale image of the original image, (B) grayscale image with contrast stretching, (C) result after first Otsu thresholding, (D) result after second Otsu thresholding (E) segmented nucleus

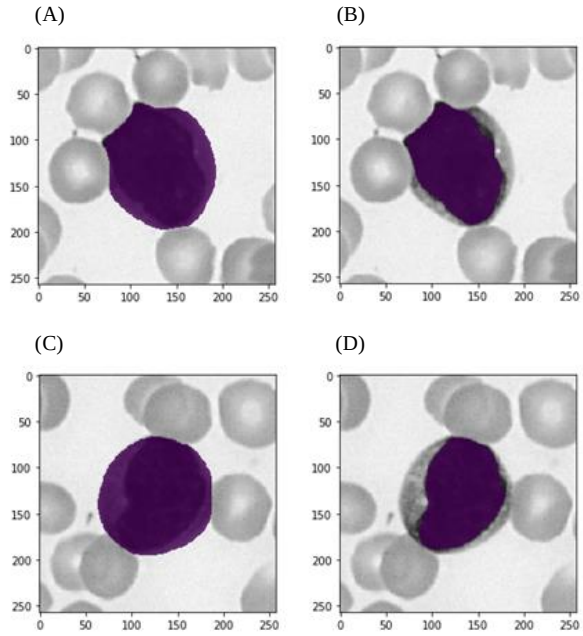

Fig. 6. Two examples of (A), (C) segmented cells and (B), (D) segmented nuclei

From each of the selected 206 images 60 features were extracted, and then dimensionality reduction was performed using the PCA method. It was decided to reduce the dimensions from 60 to 15; the contribution of each eigenvalue can be seen in Fig. 7. Also, dimensionality reduction was performed again for all features except morphological, because morphological features are the most sensitive to segmentation. In this case the dimensions were reduced from 34 to 12 (Fig. 8).

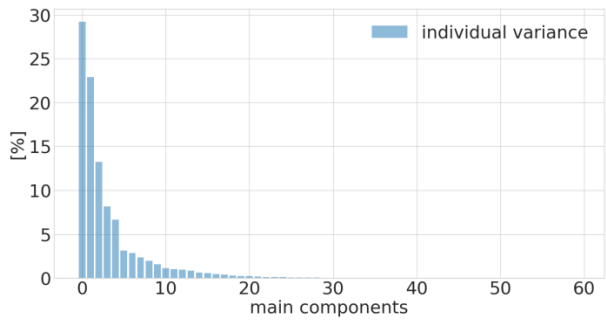

Fig. 7. Eigenvalues for all features

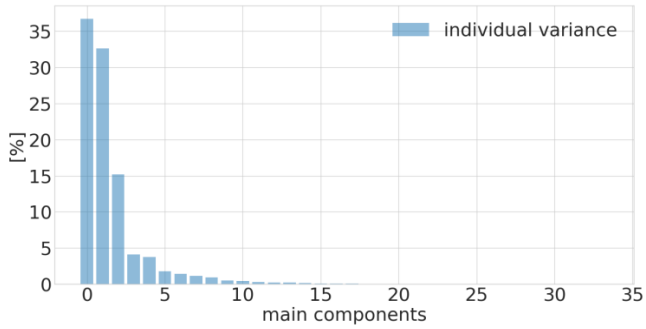

Fig. 8. Eigenvalues for texture and color features

B. Classification results

Based on 20 consecutive classification results, mean values and standard deviations for precision, sensitivity and classification accuracy were calculated for random train and test splits. Four combinations of features were used: 1) all 60 features, 2) 15 features when PCA was applied to all 60 features, 3) 34 color and texture features and 4) 12 features when these features were reduced. The following table shows the results for 3 different classification algorithms – k-Nearest Neighbours, Support Vector Machine, and feedforward neural network.

TABLE I
CLASSIFICATION RESULTS

		Precision [%]		Sensitivity [%]		**Accu-racy [%]**
		Class 0	Class 1	Class 0	Class 1	
kNN	all feat.	60.45± 10.72	95.52± 3.90	84.28± 10.85	74.45± 3.86	**75.85± 4.78**
	all feat. + PCA	75.53± 10.44	92.37± 4.92	85.24± 8.50	87.41± 4.79	**86.35± 4.82**
	color and texture feat.	67.76± 10.76	93.56± 4.57	85.89± 9.03	83.79± 4.89	**83.99± 4.94**
	color, texture + PCA	84.40± 8.73	95.36± 3.86	91.42± 6.74	91.85± 4.24	**91.45± 4.00**
SVM	all feat.	72.49± 10.15	96.40± 3.97	92.58± 7.40	86.66± 5.12	**87.86± 4.44**
	all feat. + PCA	81.33± 9.71	94.65± 4.22	89.96± 7.26	90.36± 4.57	**89.89± 4.20**
	color and texture feat.	81.28± 9.11	94.78± 4.26	90.25± 7.24	90.38± 4.70	**89.96± 4.18**
	color, texture + PCA	87.00± 7.74	95.30± 3.88	92.31± 6.50	93.12± 3.87	**92.53± 3.60**
NN	all feat.	77.67± 4.71	95.04± 4.14	83.59± 5.97	91.50± 3.95	**88.76± 4.66**
	all feat. + PCA	85.83± 9.52	93.33± 5.24	81.75± 7.63	95.40± 5.64	**90.65± 5.76**
	color and texture feat.	91.67± 7.66	90.26± 4.44	86.90± 3.98	95.25± 4.6	**91.90± 3.19**
	color, texture + PCA	95.00± 6.45	94.02± 1.79	90.80± 2.56	97.28± 3.38	**95.33± 2.04**

C. Discussion

It can be seen from the Table I that the highest classification accuracy is achieved using a feedforward neural network when only color and texture features are used with PCA - from 34 dimensions to 12. The best accuracy is 95.33%. A significant disadvantage of this method is the long execution time (about 240 s). This method, on the other hand, has the most opportunities for further improvement out of all 3 used algorithms. When using color and texture features with PCA, the results of classification using kNN and SVM algorithms are also satisfactory - 91.45% and 92.63%, respectively. It can be concluded that this selection of features used with PCA shows the best results when using images from the ALL_IDB2 database. Compared to the reference papers, accuracy of 95.33% was higher than in [8], where it is achieved 89.72%, and slightly lower than in [9] and [10], where it is 96.01% and 96.67%, respectively.

IV. CONCLUSION

This paper presents steps for ALL detection from blood images: segmentation, feature extraction, dimensionality reduction and classification. Different classification algorithms were tried out to determine which one should be developed further. Future work could focus on improving automatic segmentation, developing one of the classification methods and achieving better accuracy. Less sensitivity to initial data partition into train and test sets could be achieved using k-fold crossvalidation when classification using neural networks is performed. Finally, testing on larger image datasets is necessary to decide which features are the most distinctive in general case and so that progress in future research work could be made.

ACKNOWLEDGMENT

I would like to thank to Assistant Professor Milica Janković for her helpful advice.

REFERENCES

[1] J. M. Bennett, D. Catovsky, M. T. Daniel, G. Flandrin, D. A. Galton, H. R. Gralnick, C. Sultan, "Proposals for the classification of the acute leukaemias. French-American-British (FAB) co-operative group", *Br. J. Haematol.*, Vol. 4, No. 33, pp. 451-458, August, 1976.

[2] T. Terwilliger, M. Abdul-Hay, "Acute lymphoblastic leukemia: a comprehensive review and 2017 update", *Blood Cancer J.*, Vol. 7, Jun, 2017.

[3] R. D. Labati, V. Piuri, and F. Scotti, "All-IDB: the acute lymphoblastic leukemia image database for image processing" , Proc. of the 18th IEEE International Conference on Image Processing, Brussels, Belgium, pp. 2045–2048, September 11-14, 2011.

[4] F. Scotti, "Automatic morphological analysis for acute leukemia identification in peripheral blood microscope images", Proc. of the IEEE International Conference on Computational Intelligence for Measurement Systems and Applications, pp. 96–101, Messian, Italy, July 20-22, 2005.

[5] M. Madhukar, S. Agaian, A. T. Chronopoulos, "New decision support tool for acute lymphoblastic leukemia classification", Proc. Of SPIE – The International Society for Optical Engineering, Burlingame, California, USA, Vol. 8295, February, 2012

[6] S. Mishra, B. Majhi, P. K. Sa, L. Sharma, "Gray level co-occurrence matrix and random forest based acute lymphoblastic leukemia detection", *Biomed. Signal Process. Control.*, Vol. 33, pp. 272–280, March, 2017.

[7] L. Putzu, G. Caocci, C. Di Ruberto, "Leucocyte classification for leukaemia detection using image processing techniques", in *Artif. Intell. Med*., Vol. 62, pp 179-191, September, 2014.

[8] V. Singhal, P. Singh, "Local Binary Pattern for automatic detection of Acute Lymphoblastic Leukemia*",* Twentieth National Conference on Communications, Kanpur, India, pp. 1-5, February, 2014.

[9] A. Abdeldaim, A. Talaat, M. Elhoseny, A. E. Hassanien, "Computer-Aided Acute Lymphoblastic Leukemia Diagnosis System Based on Image Analysis", *Studies Comp. Intell.*, pp. 131-147, January, 2018.

[10] S. Neoh, W. Srisukkham, L. Zhang, S. Todryk, B. Greystoke, C. P. Lim, M. A. Hossain, N. Aslam,"An Intelligent Decision Support System for Leukaemia Diagnosis using Microscopic Blood Images**",** *Scientific Reports*, Vol. 5, October, 2015.

[11] R. C. Gonzalez, R. E. Woods, *Digital Image Processing*, 3rd ed., Prentice Hall, Upper Saddle River, NJ, 2008.

[12] Ž. Đurović, Pattern Recognition OS4PO, University of Belgrade - School of Electrical Engineering, 2019. http://automatika.etf.bg.ac.rs/sr/prepoznavanje-oblika-os4po/217-serbian/sadr%C5%BEaj/predmeti/izborni-kursevi-za-os/obrada-signala/prepoznavanje-oblika-os4po/427-os4po-materijali

[13] Y. Li, R. Zhu, L. Mi, Y. Cao, D. Yao, "Segmentation of White Blood Cells from Acute Lymphoblastic Leukemia Images Using Dual-Threshold Method", *Comput. Math. Method. M.*, Vol. 2016, pp. 1-12, January, 2016.

Brain Tumor Segmentation in MRI Scans Using Convolutional Neural Networks

Maja Pantić

***Abstract*—In this paper an algorithm for segmentation of brain tumor lesions in magnetic resonance images (MRI) using convolutional neural networks (CNN) is proposed. Precise determination of brain tumor regions is important for diagnosis, treatment choice and patient follow-up. The realized CNN model has the U-Net architecture, which is able to simultaneously extract structure characteristics and their precise locations in the input image. The U-Net is applied on the scans of high-grade glioma patients. The resulting segmentation is evaluated using Dice coefficient and the median Dice values achieved on the test images are 0.83, 0.58 and 0.74 on the whole tumor, active tumor and core tumor region respectively.**

***Index Terms*—brain tumor segmentation; biomedical image processing; convolutional neural networks; U-Net architecture.**

I. Introduction

BRAIN tumor represents the uncontrolled growth of abnormal cells within the brain tissues [1]. Brain tumors can be malignant, when they are referred to as cancer, or benign. Both types of tumor can harm the proper functioning of the affected brain region and need adequate treatment [1].

There are more than 130 types of brain tumors [2]. Based on the organ in which they first appear, brain tumors are classified either as primary or secondary (metastatic) tumors. Primary brain tumors appear in the brain and can spread to other regions in the brain or spinal cord, while metastatic tumors first appear in other body organs and spread to the brain tissues. The most common primary brain tumor type in adults is astrocytoma or glioblastoma multiforme (GBM). GBM is a type of glioma brain tumor which is formed of glial cells, supporting cells of the central nervous system [3].

According to the World Health Organization, the classification of the brain and spinal cord tumors is done on the molecular and histological level [4]. Brain tumors are categorized in four different grades based on the abnormality of tumor cells observed under a microscope and the pace of their growth and spreading. Grade I tumors, also referred to as low-grade tumors, grow and spread slower than higher grade tumors, rarely affect the surrounding tissues and can be cured if completely removed by surgery. Tumors classified as grade IV, also referred to as high-grade tumors, are the most aggressive brain tumor types, as they grow and spread at a very rapid pace and usually cannot be cured [1, 4].

Medical imaging modalities used in medical practice for brain tumor diagnosis are: computerized tomography (CT), magnetic resonance imaging (MRI), single photon emission computed tomography (SPECT) and positron emission tomography (PET). Identifying the exact position, shape and size of tumor lesions in the obtained images or 3D volumes is crucial for correct diagnosis and choice of adequate treatment methods [1]. Therefore, development of image processing techniques which automatically analyze tumor scans with the aim to segment the tumor regions and identify tumor substructures are of great importance, as they could improve and accelerate the process of diagnosis, treatment choice and patients' follow-up care [5]. Automatic segmentation of brain tumor lesions is a challenging task, as the tumor lesions can be of different shape and size and can appear in any region of the brain, as well as vary in pixel intensities in the scanned images, due to the usage of different modalities and scanning devices. Thus, automatic brain tumor segmentation techniques cannot assume any information about the position, size and pixel intensity of tumor lesions in scanned images [5].

Based on the type of information used for the segmentation of tumor regions, segmentation methods can be categorized as either generative probabilistic or discriminative [5]. Generative probabilistic methods combine knowledge of anatomical brain models with the spatial distribution of different tissue types in the brain and can usually generalize well on the previously unseen scans. Discriminative methods do not require information related to the brain structure and they segment the tumor lesions by learning the characteristics from the images and their relations to the segmentation labels manually annotated by the experts. Such methods require large datasets for the training purposes. Segmentation techniques which combine the characteristics of both generative probabilistic and discriminative methods are called generative-discriminative methods [5].

Starting from 2012, the Brain Tumor Image Segmentation Challenge (BRATS) is organized annually with the conjunction of the international Medical Image Computing and Computer Assisted Interventions (MICCAI) conference [6], with the aim of proposing different brain tumor segmentation methods and comparing the results on the commonly used publicly available dataset and using the common protocol for the results evaluation [5, 7]. Since 2014, discriminative methods based on convolutional neural networks (CNNs) have become the most commonly proposed segmentation methods in the BRATS challenges, with a number of novel network architectures as well as their variations suggested every year. CNN models trained on extracted 2 dimensional (2D) or 3 dimensional (3D) image

Maja Pantić is a student of the Master's study program at School of Electrical Engineering, University of Belgrade, 73 Bulevar kralja Aleksandra, 11020 Belgrade, Serbia (e-mail: pm193067m@student.etf.bg.ac.rs).

patches aim to predict the class of the central pixel in the patch while learning local relations between the pixels inside the extracted patch regions [8-12]. In [13] a cascaded two-pathway CNN architecture was proposed, where each path extracts features respectively from the larger-size and the smaller-size 2D patches extracted around the central pixel, so that the network can make predictions based both on the local and more global features. Fully convolutional neural networks (FCNN) do not contain dense neural layers and can produce dense segmentation of the whole images or image patches given at the network input. Number of methods proposed variations of different FCNN architectures, such as DeepMedic [14-16], VGG [15], SegNet [17, 18], U-Net [19-23] and V-Net [24, 25]. DeepMedic is a FCNN architecture with 2 parallel paths which process the input 3D patches extracted from the image at different pixel resolutions, while SegNet, VGG, U-Net and V-Net can be modified to process either whole image slices or 3D patches. Several methods propose cascaded network architectures, where the output of one network architecture is used as the input into the next network, thus achieving segmentation results through several phases [25-28]. In [29] several network architectures were trained independently and then used to form the network ensemble for final segmentation results by averaging the outputs of individual models.

In this paper the automatic discriminative method for glioma brain tumor segmentation in multimodal MR images based on the U-Net architecture of CNN is described. In Section II, the proposed CNN architecture, dataset used and the details on the algorithm implementation are described. Section III represents the segmentation results. Finally, Section IV gives brief conclusion of the proposed method, as well as possible ways of future improvements of the results.

II. The Method

A. The Database

Database used for the training and testing of the proposed segmentation algorithm is the publicly available database of MRI scans of glioma patients [30] used in the BRATS challenges 2015 and 2016 [5, 31]. The training and validation dataset contains 220 scans of high-grade glioma patients and 54 scans of low-grade glioma patients, while the testing dataset consists of 110 mixed scans of both high-grade and low-grade glioma patients. For each patient, there are 155 2D images in axial plane available, acquired with each of following MRI contrasts: T1-weighted, T1-weighted contrast-enhanced (T1c), T2-weighted and T2-weighted FLAIR. The training and validation dataset also contains masks with annotated labels of the tumor structures for all patients. All scans in the database were anonymized, scull stripped, co-registered to corresponding T1c scans and were set to the 1 mm^3 spatial resolution using linear interpolation.

The scans were manually annotated by the expert radiologists, based on the radiological criteria, so that the annotated structures belong to visually separable structures and do not strictly represent different biological structures within the brain. The tumor structures in the images are divided into four categories: edema, non-enhancing core, enhancing core and necrotic core. The annotation masks are the same size as the MRI scans and contain the following pixel-wise labels: 0 – background, 1 – necrotic core, 2 – edema, 3 – non-enhancing core, 4 – enhancing core. The enhancing core can be extracted on the high-grade glioma scans solely. The extracted tumor structures are further grouped into the following tumor regions:

- whole tumor region, which contains all four tumor structures;
- tumor core, which contains necrotic core, non-enhancing core and enhancing core;
- active tumor region, which contains enhancing core.

B. U-Net architecture

The U-Net architecture is the CNN architecture which, for the image given at its input, returns as the output the map of probabilities for each image pixel to be belonging to each of the considered segmentation classes. It was first proposed in [32], where it was used for the segmentation of the biomedical images: scans of neural structures obtained with an electron microscope and cell images obtained with a light microscope. Originally proposed U-Net architecture, as well as its modifications, found application in many other problems of biomedical image segmentation [19-23, 27, 28, 33-35]. Compared to many other CNN architectures used for segmentation purposes, the main advantage of the U-Net architecture is that it can take the whole image as its input, instead of taking various patches from the image. Thus, the network training process becomes faster and the problem of simultaneous feature extraction and their precise localization is avoided [32].

U-Net is a fully convolutional neural network. It consists of the two symmetric paths of convolutional layers, the contracting path and the expansive path, which can together be schematically represented to form the shape of the letter “U”. The aim of the contracting path is to capture context in the image and it has the typical form of the CNN. Its main block consists of two convolutional layers, with activation function applied to the output of each of them and max pooling operation applied after the 2nd convolutional layer. Every succeeding layer in the contracting path uses the doubled number of convolutional filters compared to the preceding layer. The aim of the expansive path is to precisely locate the captured details in the image. Each layer of the expansive path has the input formed by the concatenation of the output of the symmetric layer from the contracting path and the up-sampled output from the previous layer of the expansive path. On such formed input tensor, similarly as in the contracting path, two convolutional layers, each followed by activation functions, are applied and the result represents one of the inputs to the next layer of the expansive path. In the last layer of the expansive path an additional convolution operation is applied after the double convolutional layers and its output represents the map consisting of the probabilities for

each pixel in the input image to be belonging to different segmentation classes. The number of convolutional filters applied in the last convolution operation equals the number of different segmentation classes in the input image [32].

The U-Net architecture implemented in this paper, schematically represented in Fig. 1, resembles the original U-Net architecture, with several changes in the network architecture. It contains four symmetric layers in both the contracting and the expansive path, while the output of the 5th layer in the contracting path is up-sampled and concatenated to the output of the 4th layer in contracting path to form the input to the deepest layer of the expansive path. Different from the original U-Net architecture, the convolutional layers include zero-padding, so that the output of the network has the same dimensions as the input image and no cropping of the outputs from the layers of the contracting path is needed. The number of convolutional filters applied in the first layer of the contractive path is 32 and the dropout [36] is added in all layers of both the contracting and expansive path, as suggested in [33]. The up-sampling of the outputs in the expansive path is done using transposed convolution.

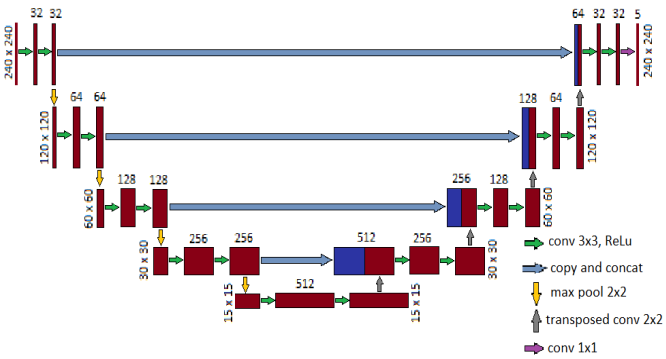

Fig. 1. Implemented U-Net architecture

C. Implementation details

The code was written using Python 3.7.4 programing language (Python Software Foundation, SAD). The network model was formed and trained using TensorFlow 1.13.1 with Keras API, with the GPU version installed for the faster and more efficient computing. The program was tested on the PC with Windows 10 Education 64-bit (Microsoft Corporation, Redmond, Washington, USA) operating system, Intel® Core™ i7-5820K (Intel Corporation, Santa Clara, California, USA) processor with 3.30 GHz frequency, 64 GB RAM and NVIDIA GeForce GTX 1060 (NVIDIA Corporation, Santa Clara, California, USA) GPU with 6 GB memory.

As the training dataset of the high-grade glioma scans contains annotations of four tumor structures, while low-grade glioma scans contain annotations of three tumor structures, as they lack enhancing core, it was chosen to train the CNN to segment only high-grade glioma scans, with the aim to segment all four tumor structures. The dataset was divided so that the scans of 170 randomly chosen patients were used for network training and validation, while the scans of the remaining 50 patients were used for testing of the trained network. The network was trained using 140 patients for training and remaining 30 patients for validation. Thus, the training and validation data subset is divided so that 83% of the data are used for training, while 17% are used for the validation of the network parameters. The test set contains 23% of the whole dataset.

As the dataset preprocessing was already done by the BRATS challenge organizers, the only preprocessing step required was the data normalization along each MRI contrast, so that the pixel values belong to the interval [-1, 1], with the zero mean and unit standard deviation, which is a suitable range for the CNN input values. The input of the network is the 4-channel tensor formed of the MRI contrasts. The masks with segmentation labels were transformed into 5-channel matrices, one for each segmentation class, using one-hot encoding principle [37]. The output of the network is the 5-channel map of the same dimensions as the input, containing the probabilities for each pixel in the input to belong to one of the 5 classes: background, necrosis, edema, non-enhancing core or enhancing core. Each pixel is assigned to the class for which the belonging probability is greater than 50%.

The loss function and metrics used for the performance evaluation during the network training are categorical cross-entropy and categorical accuracy [38], which were also chosen for the training of the original U-Net architecture [32]. The activation function after the final convolutional layer in the expansive path of the U-Net is the softmax activation function, which calculates the probability distribution for each pixel in the input image to belong to each of the segmentation classes. The formulas for softmax and categorical cross-entropy loss are given in (1) and (2):

$$softmax(z_i) = \frac{\exp(z_i)}{\sum_j \exp(z_j)} \tag{1}$$

$$J = -\sum_i p_i \log softmax(z)_i \tag{2}$$

where p_i are the weight maps which give more weight to some pixel values during the training process, and z_i represents the unnormalized probability for the pixel x to belong to the segmentation class i [38], as shown in (3):

$$z_i = \log P(y = i \mid x). \tag{3}$$

The segmentation results were evaluated using Dice coefficient, which represents the overlapping proportion of the segmented area and the annotated label:

$$DICE = \frac{2 \cdot |S_g^1 \cap S_t^1|}{|S_g^1| + |S_t^1|}. \tag{4}$$

Here $|S_g^1|$ and $|S_t^1|$ are the areas of pixels belonging to

the considered class in the annotation mask and the segmented result each, while $|S_g^1 \cap S_t^1|$ is the area of pixels belonging to the considered class in both the annotation mask and the segmentation result [5].

The network was trained using Adam optimizer [39] for the maximum of 50 epochs. Regularization techniques used are: validating the network performance on the validation set, learning rate reduction by the coefficient of 0.1 after 3 epochs and early stopping after 10 epochs of non-improving validation loss applied. After the network is trained, the parameters of the saved best model are loaded and the segmentation results are predicted on the training, validation and test sets. Dice coefficient is then calculated for segmentation results for each of the four tumor structures, as well as for the tumor regions consisting of them: tumor core, enhancing tumor and whole tumor.

III. Results and Discussion

The neural network training lasted 70 min. The best evaluation result on the validation dataset occurred in the 4th epoch and the training was stopped 10 epochs later due to early stopping. The best model achieved loss value of approx. 0.03 on the validation set and 0.02 on the training set. The average prediction time per image using the trained model was 8 ms.

TABLE I
Number of images containing tumor structures

	necrosis	edema	non-enhancing	enhancing
train	4201	10149	7525	6705
valid	1022	2252	1644	1440
test	1379	3666	2634	2284

The number of scans containing each of the tumor structures in the annotation masks for each of the datasets is given in Table 1. Overall, the training set contains 10179 images with at least one tumor structure labeled, the validation set contains 2262 images, while the test set contains 3673 images with at least one tumor structure. Table 1 clearly shows imbalanced data, as the majority of scans in all three sets contain the edema structure, while more than a half of the scans in all sets do not contain a single pixel labeled as necrosis and around a third of the scans do not contain pixels labeled as non-enhancing or enhancing core.

The boxplot diagrams of the Dice coefficient calculated for the tumor structures and tumor regions in all three sets are given in Fig. 2. Median values and mean values are presented as red horizontal lines and green triangles respectively. The boxplot diagrams show better segmentation results for the edema and enhancing core structures than the non-enhancing core and necrosis on all three sets. Dice coefficients achieved for edema and the enhancing core have mean values greater than or equal to 60% and median values greater than or equal to 75% for all three sets, so the segmentation results obtained for these structures can be considered acceptably good. On the other hand, mean values of Dice coefficient obtained for necrotic core are lower than 40% and for the non-enhanced core are around 20% on all three sets, showing poor segmentation results for these structures. The results are expected, as the edema and enhancing core have larger surfaces in the image slices than the necrosis and non-enhancing core, which makes the pixels belonging to the first two structures more common in the image data and makes it more likely for the network to classify them correctly. The mean Dice values for the tumor regions in all the sets are between 0.5 and 0.8, with the highest values achieved for the whole tumor and the lowest values for the tumor core. The mean value achieved on all three datasets for the whole tumor region is greater than 70% and median is greater than 83%. Active tumor region has the mean values greater than or equal to 60% and median greater than or equal to 75%, while the tumor core has the mean value and median each between 50% and 60%, achieved on the test set, and 60% and 80%, achieved on the training set. Achieved mean values greater than 50% and median values greater than or equal to 60% for all tumor regions suggest the successful segmentation of the tumor regions. The achieved segmentation results are comparable to the results of the algorithms available at the BRATS 2015 database website [30]. The greatest limitation of comparing the results of the proposed algorithm with the results in [30] is that in this work two subsets of the high-grade glioma set were used for training and testing of the algorithm, while in the BRATS 2015 challenge the training set consisted of high-grade and low-grade glioma sets, while the separate set without the annotations was used for testing.

An example of the segmentation results for the four tumor structures is given in Fig. 3, while Fig. 4 shows the segmentation results of the tumor regions formed from the structures in Fig. 3. In both figures the segmentation results are overlapping the corresponding annotation masks. Pixels belonging to the annotation masks which were not recognized as the tumor structure by the U-Net are shown in green, pixels predicted as the tumor structure which do not belong to the annotation mask are shown in dark blue, while pixels assigned as tumor structure in both the segmentation result and the annotation mask are presented as bright blue. The achieved values of Dice coefficient are listed under each image in both figures. The best segmentation result was achieved for the edema structure, with the Dice coefficient value of 93%, while the necrotic core was not recognized by the U-Net at all, with the Dice value 0%. It can be noticed that edema has the largest surface of all the structures, while the necrosis has the smallest surface, containing only several pixels in the annotation mask. Furthermore, the incorrectly classified pixels usually belong to the border between the structure area and the background, while pixels inside the area of the annotated structures are usually classified well. Despite the unsuccessful segmentation of the necrotic core and the average segmentation result of the non-enhancing core, with Dice value of 48%, the segmentation of the tumor regions formed from the segmented structures shows good result,

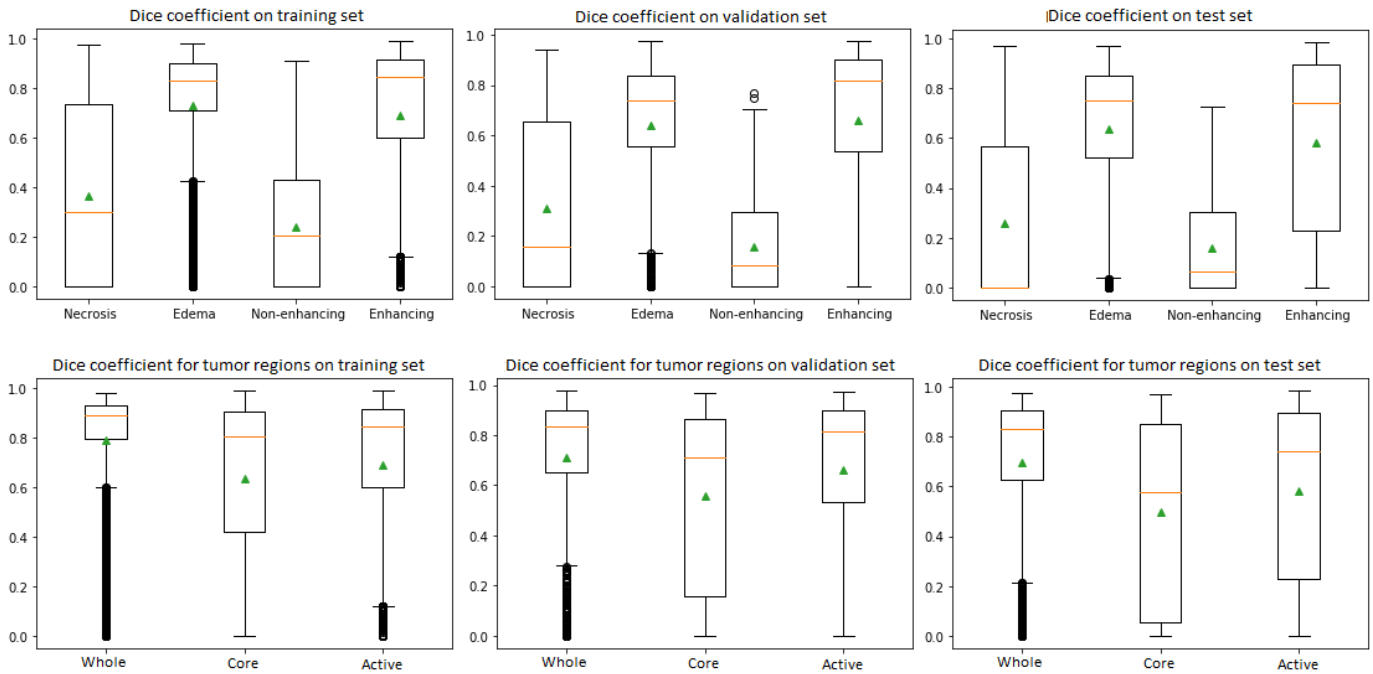

Fig. 2. Boxplot diagram for the Dice coefficient achieved on the tumor structures (1st row) and tumor regions (2nd row).

as shown in Fig. 4, with Dice values of 95% for the whole tumor, 90% for the tumor core and 85% for the active tumor. It is notable that the incorrectly classified pixels usually belong to the borderlines between the different structures.

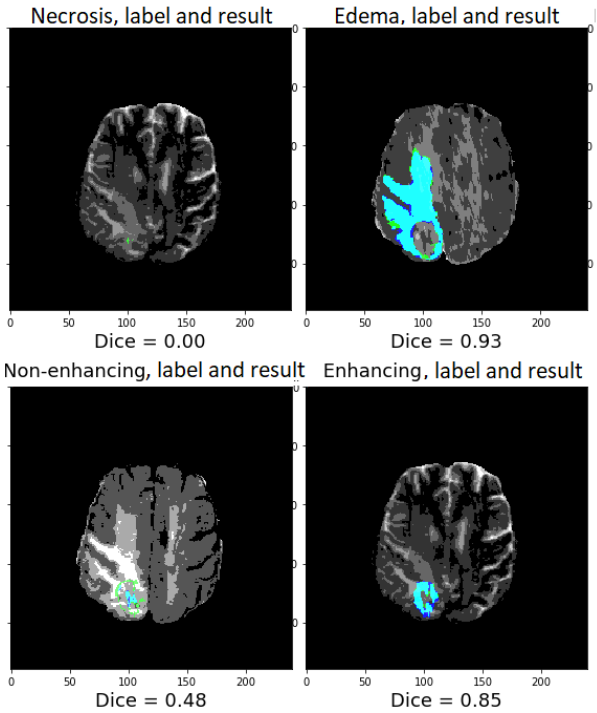

Fig. 3. Example of the segmentation results for tumor structures. Bright blue pixels belong both to the segmented lesion and the annotation mask. Green pixels are ground truth pixels not recognized by the model as tumor structures, while dark blue pixels resemble background pixels incorrectly recognized as tumor structures.

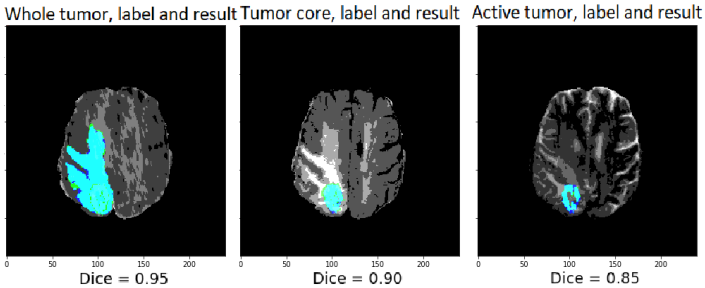

Fig. 4. Example of segmentation results for tumor regions formed from the structures in Fig. 3. The results are presented in the same color order as described in Fig. 3.

IV. Conclusion

In this paper a model of the U-Net CNN architecture was proposed and successfully applied for the segmentation of different tumor structures in the 2D MRI contracts, as well as tumor regions formed from them. The segmentation results are evaluated using Dice coefficient and can be compared to the results proposed at the BRATS 2015 benchmark. It is also shown that the promising segmentation results can be achieved for all tumor regions, with mean Dice values greater than 0.5, despite the poor segmentation results of some of the tumor structures.

Possible improvements could be achieved by modifying the U-Net architecture and tuning some of its parameters as hyper-parameters, such as the number of layers in the contracting and expansive path, number of convolutional layers applied at the input layer of the contractive path, or loss function and metrics used for the evaluation of the network training. Employing data augmentation could create more input images available during the training process and

thus prevent the network from early overfitting. Furthermore, as the consecutive axial slices of the MRI contrasts are mutually dependent, transforming the network architecture so that it extracts information from 3D volumes, instead of 2D images, could also improve results, as proposed in [19, 22].

ACKNOWLEDGMENT

The results presented in this paper were obtained as part of the author's Bachelor's thesis project, defended in September 2019 at School of Electrical Engineering, University of Belgrade. Hereby, the author would like to thank Milica Janković, Assisstant Professor at School of Electrical Engineering, University of Belgrade, the Bachelor's thesis supervisor, for suggestions and comments about this paper.

REFERENCES

[1] PDQ® Adult Treatment Editorial Board. PDQ Adult Central Nervous System Tumors Treatment. Bethesda, MD: National Cancer Institute. Available at: https://www.cancer.gov/types/brain/patient/adult-brain-treatment-pdq. Accessed: Aug, 2020. [PMID: 26389458]

[2] Cancer Research UK, https://www.cancerresearchuk.org/about-cancer/brain-tumours/types, accessed: Aug, 2020.

[3] Cancer Research UK, https://www.cancerresearchuk.org/about-cancer/brain-tumours/types/glioma-adults accessed: Aug, 2020..

[4] D. N. Louis, A. Perry, G. Reifenberger, A. von Deimling, D. Figarella-Branger, W. K. Cavenee, H. Ohgaki, O. D. Wiestler, P. Kleihues, D. W. Ellison, "The 2016 World Health Organization classification of tumors of the central nervous system: a summary," *Acta neuropathol*, vol. *131*, no. *6*, pp. *803-820*, Jun, 2016.

[5] B. H. Menze, A. Jakab, S. Bauer, J. Kalpathy-Cramer, K. Farahani, J. Kirby, Y. Burren, N. Porz, J. Slotboom, R. Wiest, L. Lanczi, E. Gerstner, M. A. Weber, T. Arbel, B. B. Avants, N. Ayache, P. Buendia, D. L. Collins, N. Cordier, J. J. Corso, A. Criminisi, T. Das, H. Delingette, Ç. Demiralp, C. R. Durst, M. Dojat, S. Doyle, J. Festa, F. Forbes, E. Geremia, B. Glocker, P. Golland, X. Guo, A. Hamamci, K. M. Iftekharuddin, R. Jena, N. M. John, E. Konukoglu, D. Lashkari, J. A. Mariz, R. Meier, S. Pereira, D. Precup, S. J. Price, T. R. Raviv, S. M. Reza, M. Ryan, D. Sarikaya, L. Schwartz, H. C. Shin, J. Shotton, C. A. Silva, N. Sousa, N. K. Subbanna, G. Szekely, T. J. Taylor, O. M. Thomas, N. J. Tustison, G. Unal, F. Vasseur, M. Wintermark, D. H. Ye, L. Zhao, B. Zhao, D. Zikic, M. Prastawa, M. Reyes, K. Van Leemput, "The multimodal brain tumor image segmentation benchmark (BRATS)," *IEEE Trans Med Imaging*, vol. *34*, no. *10*, pp. *1993–2024*, Oct, 2015.

[6] https://miccai2020.org/en/, accessed: Aug, 2020.

[7] http://braintumorsegmentation.org/, accessed: Aug, 2020.

[8] A. Davy, M. Havaei, D. Warde-Farley, A. Biard, L. Tran, P. M. Jodoin, A. Courville, H. Larochelle, C. Pal, Y. Bengio, "Brain tumor segmentation with deep neural networks," in Proc. BRATS-MICCAI, pp. *001-004*, Sept, 2014.

[9] G. Urban, M. Bendszus, F. Hamprecht, J. Kleesiek, "Multi-modal brain tumor segmentation using deep convolutional neural networks," in Proc. BRATS-MICCAI, pp. *031-035*, Sept, 2014.

[10] D. Zikic, Y. Ioannou, M. Brown, A. Criminisi, "Segmentation of brain tumor tissues with convolutional neural networks," in Proc. BRATS-MICCAI, pp. *036-039*, Sept, 2014.

[11] B. Pandian, J. Boyle, D. A. Orringer, "Multimodal tumor segmentation with 3D volumetric convolutional neural networks," in Proc. BRATS-MICCAI, pp. *049-052*, Oct, 2016.

[12] S. Chen, C. Ding, C. Zhou, "Brain tumor segmentation with label distribution learning and multi-level feature representation," in Proc. BRATS-MICCAI, pp. *050-053*, Sept, 2017.

[13] M. Havaei, A. Davy, D. Warde-Farley, A. Biard, A. C. Courville, Y. Bengio, C. Pal, P. Jodoin, H. Larochelle, "Brain tumor segmentation with Deep Neural Networks," *Medical Image Analysis*, vol. *35*, pp. *018–031*, Jan, 2017.

[14] K. Kamnitsas, E. Ferrante, S. Parisot, C. Ledig, A. Nori, A. Criminisi, D. Rueckert, B. Glocker, "DeepMedic on brain tumor segmentation," in Proc. BRATS-MICCAI, pp. *018-022*, Oct, 2016.

[15] A. Casamitjana, S. Puch, A. Aduriz, E. Sayrol, V. Vilaplana, "3D convolutional networks for brain tumor segmentation," in Proc. BRATS-MICCAI, pp. *065-068*, Oct, 2016.

[16] A. Karnawat, P. Prasanna, A. Madabushi, P. Tiwari, "Radiomics-based convolutional neural network (RadCNN) for brain tumor segmentation on multi-parametric MRI," in Proc. BRATS-MICCAI, pp. *147-153*, Oct, 2017.

[17] T.K. Lun, W. Hsu, "Brain tumor segmentation using deep convolutional neural network," in Proc. BRATS-MICCAI, pp. *026-029*, Oct, 2016.

[18] S. Dong, "A separate 3D-SegNet architecture for brain tumor segmentation," in Proc. BRATS-MICCAI, pp. *054-060*, Oct, 2017.

[19] X. Feng, C. Meyer, "Patch-based 3D U-Net for brain tumor segmentation," in Proc. BRATS-MICCAI, pp. *067-072*, Oct, 2017.

[20] F. Isensee, P. Kickingereder, W. Wick, M. Bendszus, K. H. Maier-Hein, "Brain tumor segmentation and radiomics survival prediction: contribution to the BRATS 2017 challenge," in Proc. BRATS-MICCAI, pp. *100-107*, Oct, 2017.

[21] G. Kim, "Brain tumor segmentation using deep U-Net," in Proc. BRATS-MICCAI, pp. *154-160*, Oct, 2017.

[22] C. Wang, O. Smedby, "Automatic brain tumor segmentation using 2.5D U-nets," in Proc. BRATS-MICCAI, pp. *292-296*, Oct, 2017.

[23] L. Daia, T. Lib, H. Shuc, L. Zhongd, H. Shena, H Zhub, "Automatic brain tumor segmentation with domain transfer," in Proc. BRATS-MICCAI, pp. *111-118*, Sept, 2018.

[24] M. Cata, A. Casamitjana, I. Sanchez, M. Combalia, V. Vilaplana, "Masked V-Net: an approach to brain tumor segmentation," in Proc. BRATS-MICCAI, pp. *042-049*, Oct, 2017.

[25] R. Hua, Y. Zhang, Q. Huo, Y. Gao, Y. Sun, F. Shi, "Multimodal brain tumor segmentation using cascaded V-Net," in Proc. BRATS-MICCAI, pp. *205-212*, Sept, 2018.

[26] G. Wang, W. Li, S. Ourselin, T. Vercauteren, "Automatic brain tumor segmentation using cascaded anisotropic convolutional neural networks," in Proc. BRATS-MICCAI, pp. *297-303*, Oct, 2017.

[27] D. Lachinov, E. Vasiliev, V. Turlapov, "Glioma segmentation with cascaded Unet: preliminary results," in Proc. BRATS-MICCAI, pp. *272-279*, Sept, 2018.

[28] X. Li, "Fused U-Net for brain tumor segmentation based on multimodal MR images," in Proc. BRATS-MICCAI, pp. *290-297*, Sept, 2018.

[29] K. Kamnitsas, W. Bai, E. Ferrante, S. McDonagh, M. Sinclair, N. Pawlowski, M. Rajchl, M. Lee, B. Kainz, D. Rueckert, B. Glocker, "Ensembles of multiple models and architectures for robust brain tumour segmentation," in Proc. BRATS-MICCAI, pp. *135-146*, Oct, 2017.

[30] https://www.smir.ch/BRATS/Start2015, accessed: Aug, 2020.

[31] M. Kistler, S. Bonaretti, M. Pfahrer, R. Niklaus, P. Buchler, "The Virtual Skeleton Database: An Open Access Repository for Biomedical Research and Collaboration," *J Med Internet Res*, vol. *15*, no. *11*, *e245*, Nov, 2013.

[32] O. Ronneberger, P. Fischer, T. Brox, "U-Net: Convolutional Networks for Biomedical Image Segmentation," in *MICCAI*, *Lecture Notes in Computer Science*, Springer, Cham, vol. *9351*, pp. 234*–241*, Oct, 2015.

[33] A. A. Novikov, D. Lenis, D. Major, J. Hladuvka, M. Wimmer, K. Buhler, "Fully convolutional architectures for multiclass segmentation in chest radiographs," *IEEE Trans on Med Imaging*, vol. *37*, no. *8*, pp. *1865-1876*, Feb, 2018.

[34] B. Kayalibay, G. Jensen, P. van der Smagt, "CNN-based Segmentation of Medical Imaging Data," *ArXiv*, vol. *abs/1701.03056*, n. pag. *24*, Jul, 2017.

[35] H. Dong, G. Yang, F. Liu, Y. Mo, Y. Guo, "Automatic brain tumor detection and segmentation using U-Net based fully convolutional networks", in Proc. Medical Image Understanding and Analysis (MIUA), Edinburgh, UK, Jul,2017.

[36] N. Srivastava, G. Hinton, A. Krizhevsky, I. Sutskever, R. Salakhutdinov, "Dropout: A Simple Way to Prevent Neural Networks from Overfitting", *Journal of Machine Learning Research*, vol. *15*, pp. *1929-1958*, Jun, 2014.

[37] F. Chollet, "Deep Learning for Computer Vision", in *Deep Learning with Python*, New York, USA: Manning Publications Co, 2017, ch. *5*, pp. *119-159*

[38] I. Goodfellow, Y. Bengio A. Courville, "Deep Learning", Cambridge, MA, USA: MIT Press, 2016, URL: http://www.deeplearningbook.org/, accessed: Aug, 2020.

[39] D. Kingma, J. Ba, "Adam: A Method for Stochastic Optimization", in Proc. ICLR, n. pag. *15*, Dec, 2014.

Real-time navigation system for Central Venous Catheters using ultrasound technology

Dejana Vuković, Dr. Jens Wildhagen, M.Eng. Korbinian Köhler

***Abstract*—In this paper the development and testing of a system prototype for a novel real-time navigation using 100 kHz ultrasound technology intended for the precise positioning of a CVC (Central Venous Catheter) inside the central venous system is presented. For the prototype realization a DSP (Digital Signal Processor) based hardware, including data converters, an ultrasonic transducer and a hydrophone, has been used. The processing algorithms implemented in C programming language included amplitude modulation/demodulation, matched filtering, and polyphase interpolation of chirp signals. For testing purposes, a measurement setup with a model of the upper part of the human torso based on water, agar-agar, pork ribs and pork lung was established. This paper shows the results of testing the developed prototype in terms of robustness, accuracy, and the possibility of ultrasound transmission through tissue, lungs, and ribs. The presented results indicate that even though the developed system shows a high level of accuracy (> 98 %) with a distance estimation update rate of 3.2 s and a usability for distances up to 20 cm in case of transmission through tissue and ribs, the overall applicability of the introduced ultrasound based navigation system is limited by the presence of the lungs. Additionally, the results confirm the existence of a statistically significant difference between ultrasound transmission through tissue and ribs.**

***Index Terms*—ultrasound, central venous catheter, navigation, real-time.**

I. Introduction

CENTRAL venous catheterization is a well-known technique of accessing the central venous system by cannulating large veins to enable the administration of medications or fluids in cases when standard administration methods are not possible or insufficient [1]. A CVC (*Central Venous Catheter*) can be applied during surgery and/or postoperatively for parenteral nutrition, dialysis, or pain control therapy. To accomplish the successful delivery of medication, the CVC tip needs to be positioned inside the vena cava just above the heart [2].

Current solutions for the CVC navigation and positioning include usage of X-ray or ECG (*electrocardiogram*) technology. In both cases, the CVC is blindly navigated using anatomical indicators. The confirmation of correct position of the CVC can then be verified once at the end of procedure using X-ray or in real-time using ECG [3][4].

In this paper a novel navigation system using ultrasound technology is proposed. The main idea is to transmit ultrasonic signals from the patient's chest and receive them at the tip of the CVC under placement. The time between signal transmission and signal detection shall be used to determine the corresponding distance and calculate the position of the catheter tip in relation to the patient's anatomy [5]. It was expected that for ultrasound frequencies between 10 kHz and 750 kHz the developed system will enable transmission of ultrasound signals through lungs (air) and bones [6][7]. In comparison to X-ray and ECG techniques, the introduced system should ensure a reliable real-time CVC navigation unaffected by changes in physiological signals, which is not dependent on the applicant's skills and is not exposing the patient to unnecessary X-ray radiation.

This paper provides deeper insight into the possibility of ultrasound transmission through the human chest. It introduces an idea for a new and original CVC navigation system and investigates its applicability in the real-life environment.

II. The Method

The implementation of the developed system included realization of a suitable hardware, a model of the upper part of the human torso and appropriate signal processing techniques.

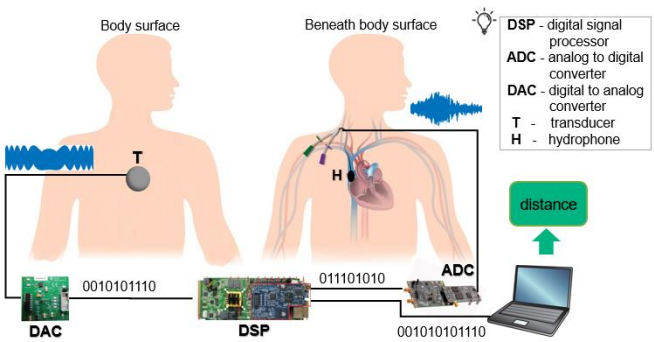

Fig. 1. Schematics of the implemented system.

A. Hardware

The technical part of the system comprising of evaluation boards for DSP (*Digital Signal Processor*) - TMDSEVM6657LS (fixed and floating point, dual core, 1 GHz CPU speed per core), DAC (*Digital to Analog Converter*) – DAC80504EVM (16-bit) and ADC (*Analog to Digital Converter*) – ADS8920BEVM-PDK (16-bit), all manufactured by Texas Instruments (Dallas, Texas, USA),

Dejana Vuković is with the School of Electrical Engineering, University of Belgrade, 73 Bulevar Kralja Aleksandra, 11020 Belgrade, Serbia (e-mail: dejana.vukovicc@gmail.com)

Jens Wildhagen is with B. Braun Melsungen AG, Carl-Braun-Straße 1, 34212 Melsungen, Germany (e-mail: jens.wildhagen@bbraun.com)

Korbinian Köhler is with B. Braun Melsungen AG, Carl-Braun-Straße 1, 34212 Melsungen, Germany (e-mail: korbinian.koehler@bbraun.com)

was responsible for the real-time signal generation and processing. The communication between DSP and data converters was established using a 41.67 MHz SPI (*Serial Peripheral Interface*) channel of the DSP. The sampling rate of the implemented system was 306.7 kHz. An ultrasound transducer of frequency 100 kHz, bandwidth 16 kHz, diameter 40±0.5 mm, manufactured by Multicomp Electronic Components (Leeds, England) was used. The hydrophone used in this project was a miniature probe BII-7186 manufactured by Benthowave Instrument Inc. (Collingwood, Canada). The BII-7186 probe is equipped with a built-in digitally programmable preamplifier and a high pass filter with a cut-off frequency of 30 kHz. The amplification factor used in the project was 40 dB. Schematics of the implemented system can be seen on Fig. 1.

B. *Model of upper part of human torso*

In order to obtain a model with comparable results in terms of ultrasound transmission through the human chest, raw pork ribs and pork lung were used considering the anatomical similarity as well as the speed of sound. Due to the similarity of the speed of sound in tissue, vein, and water (1540 m/s for tissue and vein, 1493 m/s for water), water was used to model tissue. A plastic rectangular water tank (43 cm/40.3 cm x 27 cm x 34 cm/31 cm) with a silicone membrane (26 cm x 19 cm, thickness 3 mm, speed of sound 990 m/s) was designed as a basic setup, whereas different samples of agar-agar moulds (thickness 2 cm, speed of sound 1547 m/s) with samples of rib or lung were used to establish different transmission mediums (Fig. 2. left). The agar-agar moulds were prepared by dissolving agar-agar powder in cold water (5 g agar-agar per 100 ml water), bringing it to boil, cooling it down for 2 h (at a room temperature of approximately 22 °C), pouring the still liquid solution over the samples of lung (8 cm x 7 cm, thickness 2 cm) or rib (8.8 cm x 1 cm x 0.6 cm) within a rectangular glass container (9 cm x 15 cm x 2 cm) and leaving it to cool down in a refrigerator for another 2 h. The silicone membrane was used on the front part of the water tank to simulate the transmission of ultrasound signals through the skin on the human chest (Fig. 2. right). The influence of the ultrasound attenuation during the transmission from the transducer to the silicone membrane was minimized using conductive gel. The final measurement setup can be seen on Fig. 3.

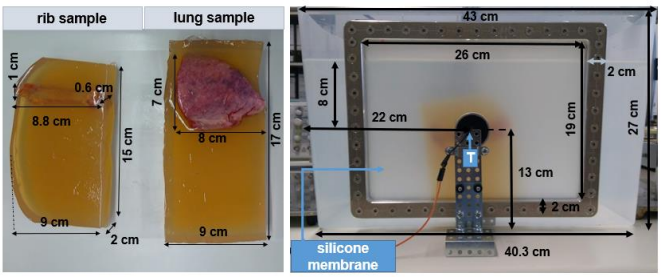

Fig. 2. Left: rib and lung measurement samples with dimensions, right: front view of water tank with silicone membrane, transducer, and rib measurement sample (inside the water tank) including corresponding dimensions.

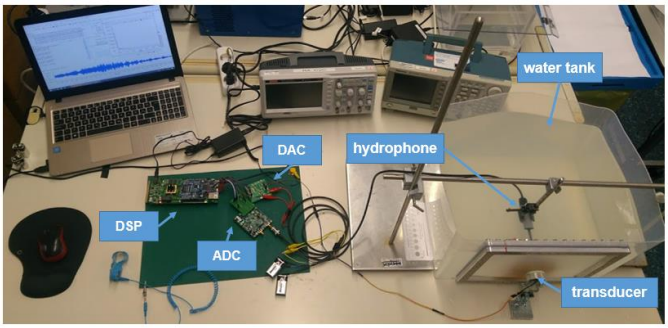

Fig. 3. The final measurement setup.

C. *Signal processing*

The processing algorithms were developed in C programming language within the CCS v9.1 (*Code Composer Studio*) development environment (Texas Instruments, Dallas, Texas, USA). A block diagram of the implemented signal processing can be seen on Fig. 4.

It has been shown that for frequencies inside the interval from 10 kHz to 750 kHz, the attenuation of the ultrasound signal in lungs decreases as the frequency increases [8], whereas for the transmission of ultrasound through ribs the opposite is valid [7]. The frequency of ultrasound signals used in this project was 100 kHz, chosen as a tradeoff between the conditions mentioned above.

The linear baseband chirp signal with unit amplitude, duration T and frequency sweep (bandwidth) B is defined as follows [9]:

$$m[n] = e^{j2\pi\left(f_0 nT_s + \frac{K}{2}(nT_s)^2\right)}, n = \{1 \dots N\} \tag{1}$$

where N is the number of samples of the chirp signal $m(t)$ sampled in the time moments $t = nT_s$, T_s is the sampling period, $K = \frac{B}{T}$, and $f_0 = -\frac{B}{2}$ is the frequency in the time moment $t = 0$. In this project a bandwidth of 16 kHz and a duration of 20 ms have been used.

DSBSC-AM (*Double Sideband Suppressed Carrier - Amplitude Modulation*) of the chirp signal can be formulated as follows [10]:

$$\begin{aligned} s[n] &= Re\{A_c m[n] e^{j2\pi F_c nT_s}\} \\ &= A_c \cos\left(2\pi\left((f_0 + F_c)nT_s + \frac{K}{2}(nT_s)^2\right)\right) \end{aligned} \tag{2}$$

where F_c is the frequency of the carrier wave with the amplitude A_c (here: F_c = 100 kHz, A_c = 1.25 V). Due to characteristics of the used DAC, the transmitted signal was a unipolar value of the modulated signal, as given per:

$$t[n] = s[n] + 1.25 \tag{3}$$

The removal of the DC (*Direct Current*) component of the received signal (present due to characteristics of the used ADC) is performed as follows:

$$r[n] = r_n[n] - r_{DC} \tag{4}$$

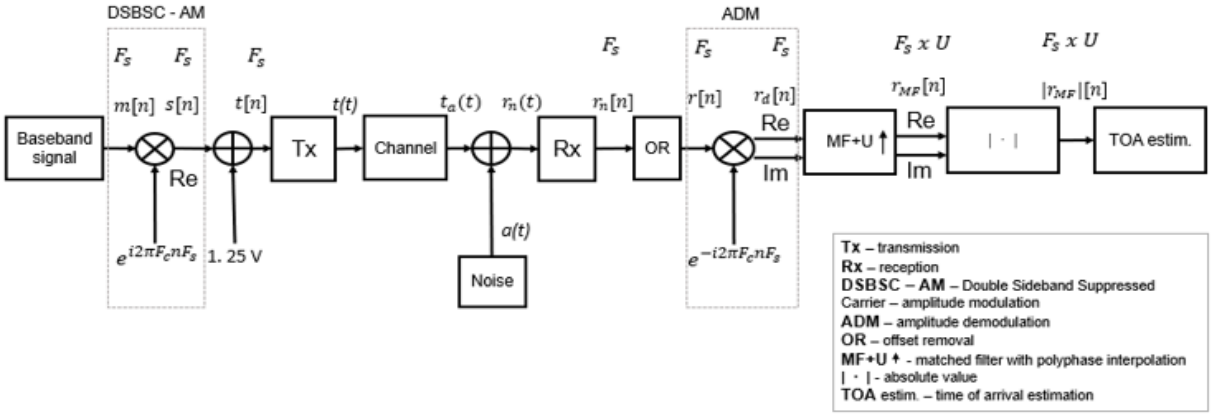

Fig. 4. Block diagram of implemented processing techniques.

$$r_{DC} = \frac{1}{N}\sum_{n=1}^{N} r_n[n] \quad (5)$$

$$r_n[n] = r_n(nT_s) \quad (6)$$

$$r_n(t) = t_a(t) + a(t) \quad (7)$$

$$t_a(t) = B_c \cos\left(2\pi\left((f_0 + F_c)t + \frac{K}{2}t^2\right)\right) \quad (8)$$

where $r_n[n]$ are samples of the signal $r_n(t)$, obtained as the sum of the received attenuated signal $t_a(t)$ with amplitude B_c and the noise $a(t)$ in time moments $t = nT_s$, r_{DC} is the estimated DC component, $r[n]$ are samples of the received signal obtained after the removal of the DC component r_{DC}.

The process of amplitude demodulation of the passband chirp signal can be formulated as follows [10]:

$$r_d[n] = r[n]e^{-j2\pi F_c nT_s}$$
$$= \frac{B_c}{2}e^{j2\pi\left(f_0 nT_s + \frac{K(nT_s)^2}{2}\right)} + \frac{B_c}{2}e^{-j2\pi\left((f_0+2F_c)nT_s + \frac{K(nT_s)^2}{2}\right)}$$
$$+(a[n] - r_{DC})(\cos(2\pi F_c nT_s) - j\sin(2\pi F_c nT_s)) \quad (9)$$

where $r_d[n]$ are the samples of the received demodulated signal.

Matched filtering generates its output by correlating a known template signal with the input signal. It is analogue to convolving the input signal with a complex-conjugated and time inverse version of a known template signal [11]. The output of the matched filter is defined as:

$$r_{MF}[n] = r_d[n] * h[n] = \sum_{i=1}^{N} r_d[i]h[n-i] \quad (10)$$

where $h[n] = m^*[-n]$ is the impulse response of the matched filter corresponding to the complex-conjugated time inverse version of the baseband chirp signal with a duration of N samples.

The output of the matched filter in an ideal noiseless case for a chirp signal as defined per (10) is:

$$r_{MF}[n] = \frac{1}{\pi K n T_s}\sqrt{\frac{jB}{T}}\sin(\pi B n T_s)\, e^{j2\pi\left(f_0 nT_s - \frac{K(nT_s)^2}{2}\right)}$$
$$= \sqrt{TB}\frac{\sin(\pi B n T_s)}{\pi B n T_s}\sqrt{j}\, e^{j2\pi\left(f_0 nT_s - \frac{K(nT_s)^2}{2}\right)} \quad (11)$$

where $\sqrt{\frac{jB}{T}}$ represents scaling factor resulting from frequency response of a compression filter in a form of a dispersive delay line that enables an ideal compression of chirp signal.

The magnitude of the matched filter output is therefore:

$$|r_{MF}[n]| \approx \sqrt{TB}\frac{\sin(\pi B n T_s)}{\pi B n T_s} \quad (12)$$

and represents a form of a standard $sinc$ function.

In order to increase the resolution of the matched filter output, a polyphase interpolation was used. The polyphase interpolation implements a parallel bank of polyphase FIR (*Finite Impulse Response*) filters, whose impulse responses within matched filtering are upsampled values of the template signal. If the factor of interpolation is *U*, then for each sample of input signal the interpolation filter will provide *U* new values between successive samples of the interpolated signal [12]. The interpolation factor used in the project was 6.

The time of arrival of a transmitted signal was calculated as follows:

$$\tau_{TOA} = \tau_E - \tau_o \quad (13)$$

$$\tau_o = \tau_{Ec} - \tau_c \quad (14)$$

$$\tau_c = \frac{d_c}{c_c} \quad (15)$$

where τ_E and τ_{Ec} are the time moments corresponding to the measured peak of magnitude of matched filter output during experimental measurement and calibration and τ_c the correct time delay expected for a distance d_c during calibration in a transmission medium with the speed of sound c_c. The peak of the magnitude of the matched filter was estimated using a simple algorithm for signal maximum computation. Additionally, τ_o denotes the time offset in time of arrival estimation introduced by the system (DAC-ADC conversion, transducer maximum amplitude rise time). The estimation of the distance d was defined as:

$$d = \tau_{TOA}\, c \quad (16)$$

where c is the speed of sound in the transmission medium [5].

D. *Testing of system and statistical analysis*

The robustness of the system was estimated by observing the SNR (*Signal-to-Noise Ratio*) in correspondence to the change in the transmission medium and the distance between transmission and reception. The SNR was defined as:

$$SNR_{dB} = 20\log_{10}\frac{A_1}{A_2} \tag{17}$$

where A_1 and A_2 stand for the magnitude of the strongest and the second strongest peak in the output of the matched filter.

The relative error of distance measurement e_r was estimated using the following relation:

$$e_r = |d_m - D|/D \tag{19}$$

where d_m is the measured distance and D is the exact distance between transducer and hydrophone. The exact distance was measured using a ruler (resolution 1 mm) positioned at the bottom of the water tank by measuring the distance between the marked center of the transducer on the inner part of the silicone membrane and the tip of the hydrophone, which were aligned prior to the measurement.

System testing with different mediums on different distances has been realized using testing conditions shown in Table I. For each of the testing conditions 30 repetitions have been performed.

TABLE I. TESTING CONDITIONS

Medium	*F_c[kHz]*	*B[kHz]*	*T[ms]*	*D[cm]*
Tissue				5
Rib	100	16	20	10
Lung				20

After obtaining samples for all of the previously described testing conditions, statistic descriptors (mean, standard deviation, median, variance, range, interquartile range, skewness, kurtosis) have been computed using the SSPS v. 27 (*Statistical Package for the Social Sciences)* software package (IBM, Armonk, New York, USA).

The existence of a statistically significant difference between samples of distance estimation in different mediums was examined using the Wilcoxon signed rank test. It tests the hypothesis that the difference of samples of two vectors of data comes from a distribution with a zero median. The result of the test is 1 if it successfully rejects the hypothesis at 5 % significance level, and 0 otherwise. For the implementation in the project the built-in MATLAB (MathWorks, Natick, Massachusetts, USA) function *signrank* was used.

The speed performance of the system was verified by 30 repetitive measurements of the number of clock cycles needed for an execution of the implemented processing algorithm.

III. MAIN RESULTS

Results of the signal processing described in Section II in case of a generated baseband chirp signal with a bandwidth of 16 kHz, a duration of 20 ms, a modulation with carrier on a frequency of 100 kHz and a transmission through the testing medium tissue on a distance of 5 cm, can be seen on Fig. 5-9.

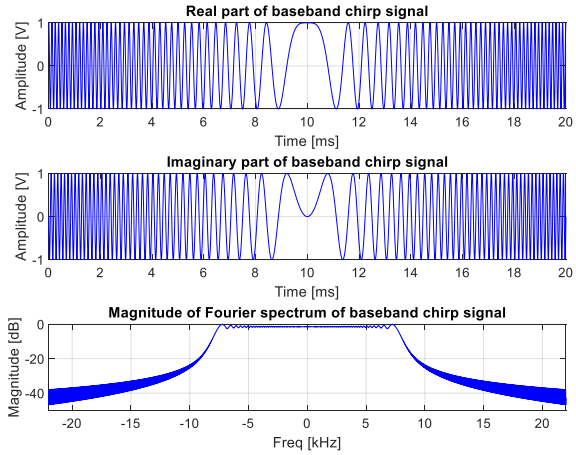

Fig. 5. Baseband chirp signal $m[n]$ with bandwidth 16 kHz and duration 20 ms (top to bottom): real part, imaginary part, magnitude of Fourier spectrum.

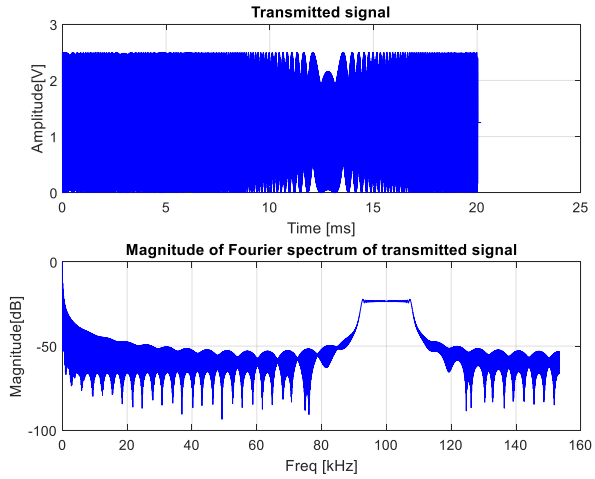

Fig. 6. Transmitted signal $t[n]$ (baseband chirp signal after modulation with carrier on frequency 100 kHz and DC component addition, top to bottom): real part, magnitude of Fourier spectrum.

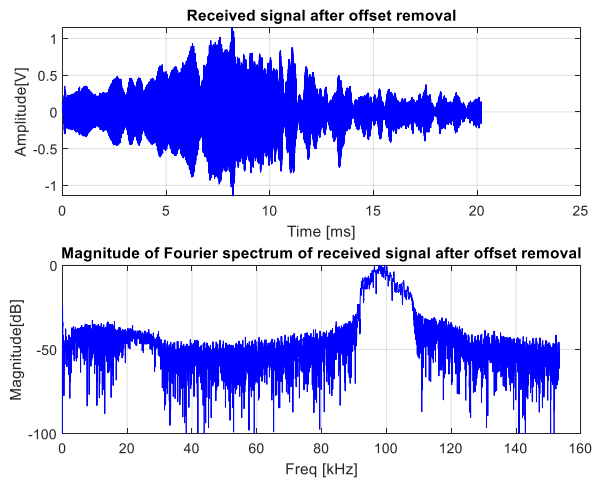

Fig. 7. Received signal $r[n]$ after DC offset removal in case of transmission through testing medium tissue on distance 5 cm (top to bottom): time domain, magnitude of Fourier spectrum.

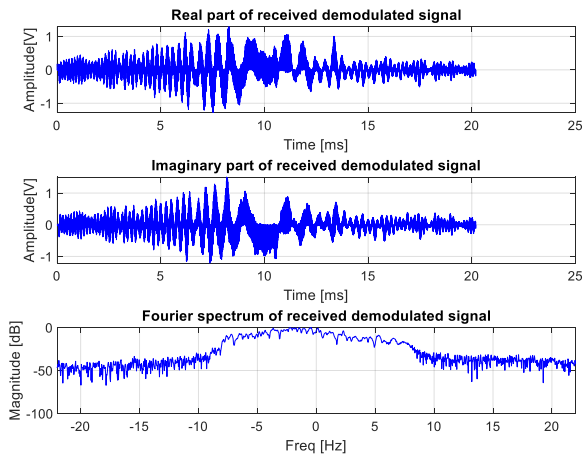

Fig. 8. Received signal without DC component after demodulation with carrier on frequency 100 kHz - $r_d[n]$, in case of transmission through testing medium tissue on distance 5 cm (top to bottom): real part, imaginary part, magnitude of Fourier spectrum.

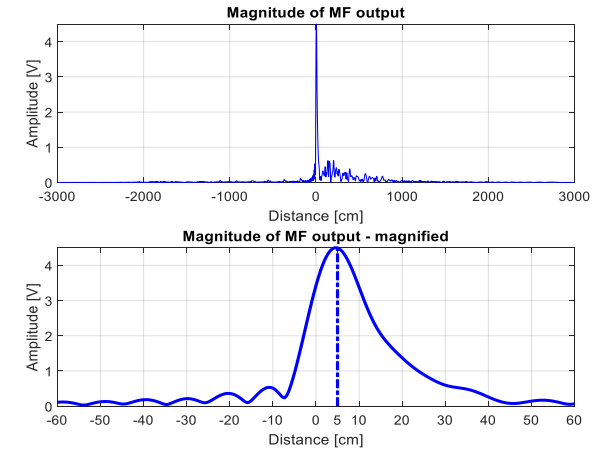

Fig. 9. Magnitude of matched filter output of received demodulated signal without DC offset and baseband chirp signal - $|r_{MF}[n]|$ (top to bottom): all samples, magnified section [-60 cm, 60 cm].

Fig. 7. shows that the DC offset component on 0 kHz was successfully removed. Additionally, Fig. 7. (bottom) indicates that there is a substantial amount of noise present on all components of the spectrum.

Fig. 9. (top) shows that the matched filter output in case of a transmission through the testing medium tissue on 5 cm contains several smaller peaks originating from the reflection of the sides of water tank besides the most prominent peak. Fig. 9. (bottom) indicates that the most prominent peak corresponds to the 5 cm distance (the exact distance between the points of transmission and reception).

SNR characteristics (mean values with confidence intervals) obtained during the transmission of chirp signals with a bandwidth of 16 kHz, a duration of 20 ms, modulated with carrier on a frequency of 100 kHz in testing mediums tissue and rib on distances of 5 cm, 10 cm, and 20 cm can be seen on Fig. 10. It shows that as the distance between the points of transmission and reception increases, the estimated SNR decreases. Additionally, the introduction of a rib results in an additional loss of SNR of approximately 4 dB.

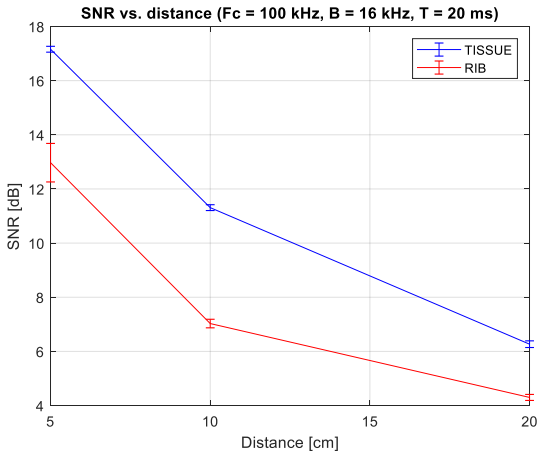

Fig. 10. SNR characteristics in case of transmission of ultrasound signals of frequency 100 kHz, with bandwidth 16 kHz, duration 20 ms in testing medium tissue and medium rib for distances 5 cm, 10 cm, and 20 cm.

The overlapped output of the matched filter and the fraction of the first millisecond of the received signal after offset removal in case of a transmission through testing medium lung on 5 cm can be seen on Fig. 11. The graphs indicate that the most prominent peak does not correspond to the exact distance of 5 cm (approx. 115 cm). As it is not known whether the ultrasound travels through the connective tissue of the lung or through a lot of air-tissue interfaces, it is difficult to estimate whether one of the smaller peaks prior to the most prominent one corresponds to the indirect path through the lungs. Considering that the first peak is present at approximately 17 cm and that the distance from the transducer to the water surface above the water tank is 8 cm (Fig. 2. (right)), this peak could be the result of a surface reflection.

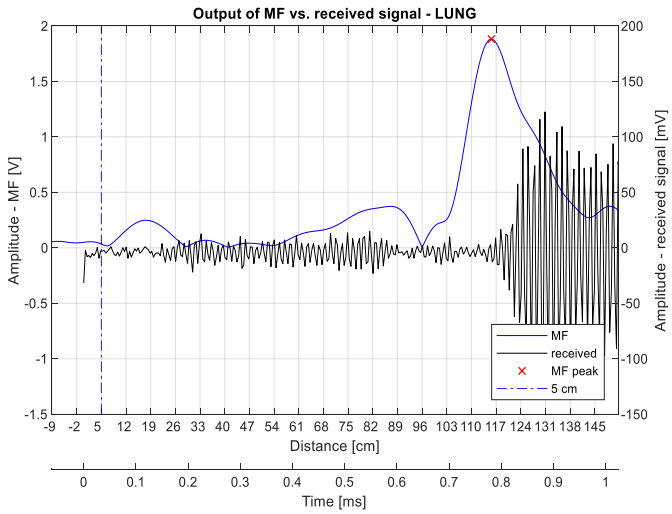

Fig. 11. Overlapped magnitude of matched filter output of received demodulated signal without DC component and baseband chirp signal (blue line) and received signal after DC offset removal (black line) obtained during transmission of ultrasound signals in testing medium lung on distance 5 cm.

The values of the statistic descriptors for the relative error of distance estimation during transmission within the testing medium tissue on distances of 5 cm, 10 cm, and 20 cm can be seen in Table II, whereas comparative values of statistic descriptors for the distance estimation during transmission

within the testing mediums tissue and rib on an exact distance of 5 cm can be seen in Table III.

TABLE II. RELATIVE ERROR OF DISTANCE ESTIMATION DURING TRANSMISSION IN TESTING MEDIUM TISSUE ON DISTANCES 5 CM, 10 CM, AND 20 CM

Descriptor	e_r		
	D = 5 cm	D = 10 cm	D = 20 cm
Mean [%]	0.36	0.62	1.66
Median	$3.67 \cdot 10^{-3}$	$8.86 \cdot 10^{-3}$	$1.67 \cdot 10^{-2}$
Variance	$0.68 \cdot 10^{-3}$	0.14	$0.28 \cdot 10^{-1}$
Std. deviation [%]	$0.26 \cdot 10^{-3}$	0.38	0.17
Range	$2.00 \cdot 10^{-3}$	$8.04 \cdot 10^{-3}$	$1.21 \cdot 10^{-2}$
Interquartile Range	0.00	$8.04 \cdot 10^{-3}$	0.00
Skewness	-2.49	-0.74	-3.39
Kurtosis	5.73	1.55	19.95

TABLE III. COMPARISON OF DISTANCE ESTIMATION DURING TRANSMISSION IN TESTING MEDIUMS TISSUE AND RIB ON DISTANCE 5 CM

Descriptor	d_m	
	Tissue	*Rib*
Mean	5.02	3.35
Median	5.02	3.24
Variance	$1.69 \cdot 10^{-6}$	$2.25 \cdot 10^{-4}$
Std. deviation	$0.13\ x\ 10^{-2}$	0.15
Range	0.01	0.04
Interquartile Range	0.00	0.32
Skewness	-2.49	0.87
Kurtosis	5.73	1.22

The values in Table II show that with the increase in distance the mean value of the relative error also increases. The standard deviation of the relative error < 1 % indicates that there are no significant changes in the repetitive measurements of the received signal. Table III shows lower mean values of the distance estimation for the testing medium rib than medium tissue. This result is corresponding to the theoretical consideration that the speed of sound in bones is bigger than in tissue/water.

Based on the 30 repetitions of clock measurements, it has been calculated that the update rate of the distance estimation was 3.2 GHz (3.2 s).

The Wilcoxon signed rank test on measurements in the testing mediums tissue and rib for a distance of 5 cm shows value 1. Therefore, there is a statistically significant difference between transmissions in these two mediums.

IV. DISCUSSION AND CONCLUSION

Based on the previously shown results the presented system ensures a low error of distance estimation (< 2 %) for distances up to 20 cm with a relatively reasonable update rate. However, even though the system is usable in the testing mediums tissue and rib, the results of a transmission through the testing medium lung do not give enough information to confirm the premise that a transthoracic transmission on a frequency of 100 kHz is possible as contrary to the expected results, given in [7]. Therefore, the presented system did not prove to be a viable replacement for existing real-time CVC navigation systems.

Besides the limitation resulting from the ultrasound attenuation in lungs, the performance of the prototype was limited by the characteristics and the interconnection of the hardware. The usage of long wires affected the speed of the SPI and the sampling rate of the system. The low amplitude of the transmitted signals has resulted in low sound pressure levels, whereas the narrow bandwidth of the transducer has affected the amplitude of the matched filter output. By increasing the sound pressure levels of the transmitted signals and the usage of wideband transducers within a uniform electronic system, a further investigation of the possibility of transthoracic transmission can be obtained in future attempts.

ACKNOWLEDGMENT

The authors owe gratitude to CoE Pain Control and CVC within the Hospital Care division of B. Braun Melsungen AG (Melsungen, Germany) for providing equipment for research and prototype development. Special acknowledgment is dedicated to Assistant Prof. Milica Janković, PhD, for help and suggestions during the work on this project.

REFERENCES

[1] R. Taylor, A. Palagiri, “Central venous catheterization“, *Crit. Care Med.*, 35(5), pp. 1390-1396, May 2007.

[2] A. K. Krishnan, P. Menon, S. V. Kumar, "Electrocardiogram-guided Technique: An Alternative Method for Confirming Central Venous Catheter Tip Placement", *JETS*, 11(4), pp. 276-281, Oct. 2018.

[3] H. Kamalipour, S. Ahmadi, P. Kamalipour, "Ultrasound for Localization of Central Venous Catheter: A Good Alternative to Chest X-Ray", *Anesth Pain Med.*, 6(5), pp. e.38834, Oct. 2016.

[4] Y. Jeon, H. G. Ryu, J.H. Kim, J.H Bahk, "Transesophageal echocardiographic evaluation of ECG-guided central venous catheter placement", *Can J Anaesth*, 53, pp. 978-983, Oct. 2006.

[5] S. Holm, “Ultrasound positioning based on time-of-flight and signal strength”, *2012 International Conference on Indoor Positioning and Indoor Navigation*, Sydney, Australia, 13-15. Nov. 2012.

[6] W. Lin, Y.X. Quin, C. Rubin, “Ultrasonic Wave Propagation in Trabecular Bone Predicted by the Stratisfied Model”, *Ann Biomed Eng*, 29, pp. 781-790, Sept. 2001.

[7] D. Rueter, H. P. Hauber, D. Droeman, P. Zabel, S. Uhling, “Low-frequency Ultrasound Permeates the Human Thorax and Lung: a Novel Approach to Non-Invasive Monitoring”, *Ultraschall in der Medizin*, 31(1), pp. 53-62, Feb 2010.

[8] P. C. Pedersen, H. S. Ozcan, “Ultrasound properties of lung tissue and their measurements”, *Ultrasound Med Biol*, 12(6), pp. 483-499, June 1986.

[9] Wikipedia, *Chirp*, [Online]. Available: https://en.wikipedia.org/wiki/Chirp (10.08.2020.)

[10] S. A. Tretter, *Communication System Design Using DSP* Algorithms, 3rd ed, New York, USA: Springer, 2008.

[11] T. T. Mar, S. S. Y. Mon, “Pulse compression method for radar signal processing”, *IJSEA*, 3(2), pp. 31-35, 2014.

[12] M. Popovic, *Digitalni procesori signala [Digital signal processors]*, 3rd ed.Belgrade, Serbia: Academic mind, 2003.